Clarkson University

Proper Orthogonal Decomposition Based Reduced Order Modeling for Fluid Flow

A dissertation by

by

Fariduddin Behzad

Department of Mechanical and Aeronautical Engineering

Submitted in partial fulfillment of requirements
for the degree of

Doctor of Philosophy, Coulter School of Engineering

December 2014

_________________, _________________

Date, Dean

ProQuest LLC.
789 East Eisenhower Parkway
P.O. Box 1346
Ann Arbor, MI 48106 - 1346

The undersigned have examined the dissertation entitled **"Proper Orthogonal Decomposition Based Reduced Order Modeling for Fluid Flow"** presented by **Fariduddin Behzad**, a candidate for the degree of Doctor of Philosophy, and hereby certify that it is worthy of acceptance.

____________________,

Date,

Dr. Goodarz Ahmadi (Advisor)

Dr. Brian T. Helenbrook (Co-advisor)

EXAMINING COMMITTEE

Dr. Erik M. Bolt

Dr. John B. McLaughlin

Dr. Piergiovanni Marzocca

Acknowledgements

Looking back in time, there are many people who contributed directly or indirectly in this achievement and they all deserve my deepest gratitude. My special thanks to Dr. Brian Helenbrook and Dr. Goodarz Ahmadi, my advisors, who guided me in my academic pursuit. It is an honour for me to work with them. I would also like to thank my other advisory committee members, Drs. Erik M. Bollt, John B. McLaughlin, Piergiovanni Marzocca, and Ratneshwar (Ratan) Jha for their encouragement and assistance. I would also like to thank Brian T. Huntley, Technical Director of IT Operations, in providing the Cluster as the main hardware which let me perform the simulations of this study.

Clarkson University

Abstract

Department of Mechanical and Aeronautical Engineering

Doctor of Philosophy

by Fariduddin Behzad

Proper orthogonal decomposition-based reduced order modeling is a technique that can be used to develop low dimensional models of fluid flow. In this technique, the Navier-Stokes equations are projected onto a finite number of POD basis functions resulting in a system of ODEs that model the system. The overarching goal of this work is to determine the best methods of applying this technique to generate reliable models of fluid flow. The first chapter investigates some basic characteristics of the proper orthogonal decomposition using the Burgers equation as a surrogate model problem. In applying the POD to this problem, we found that the eigenvalue spectrum is affected by machine precision and this leads to non-phsical negative eigenvalues in the POD. To avoid this, we introduced a new method called deflation that gives positive eigenvalues, but has the disadvantage that the orthogonality of the POD modes is more affected by numerical precision errors. To reduce the size of eigenproblem of POD process, the well-known snapshot method was tested. It was found that the number of snapshots required to obtain an accurate eigenvalue spectrum was determined by the smallest time scale of the phenomenon. After resolving this time scale, the errors in the eigenvalues and modes drop rapidly then converge with second-order accuracy. After obtaing POD modes, the ROM error was assessed using two errors, the error of projection of the problem onto the POD modes (the out-plane error) and the error of the ROM in the space spanned by POD modes (the in-plane error). The numerical results showed not only is the in-plane error bounded by the out-plane error (in agreement with theory) but it actually converges faster than the out-of-plane error. The second chapter is dedicated to building a robust POD-ROM for long term simulation of Navier-Stokes equation. The ability of the POD method to decompose the simulation and the capability of POD-ROM to simulate a low and high Reynolds flow over a NACA0015 airfoil was studied. We observed that POD can be applied for low Reynolds flows successfully if a proper stabilization method is used. For the high Reynolds case, the convergence of the eigenvalues spectrum with respect to duration of time window from we observed that the number of modes needed to simulate a certain time window increases almost linearly with the length of the time window. So, generating a POD-ROM for high Reynolds flow that reproduced the correct long-term limit cycle behavior needs many more modes than has been usually used in the literature. In the last chapter, we address the problem that the standard method of generating POD modes may be inaccurate when used off-design (at parameter values not used to generate the POD). We tested some of the popular methods developed to remedy that problem. The accuracy of these methods was in direct relation with the amount of data provided for those methods. So, in order to generate appropriate POD modes, very large POD problems must be solved. To avoid this, a new multi-level method, called recursive POD, for enriching the POD modes is introduced that mathematically provides optimal POD modes while reducing the computational size of problem to a manageable degrees. A low Reynolds flow over NACA 0015, actuated with constant suction/blowing of a fluidic jet located on top surface of airfoil is used as benchmark to test the technique. The flow is shifted from one periodic state to another periodic state due to fluidic jet effect. It was found that the modes extracted with the recursive POD method are as accurate as the modes of the best known method, global POD, while the computational effort is lower.

Contents

Acknowledgements **ii**

Abstract **iii**

List of Figures **viii**

List of Tables **xii**

Abbreviations **xiii**

1 Introduction **1**

1.0.1 Objectives 2

2 POD-ROM **5**

2.1 Introduction 5

2.2 Problem Formulation 8

2.3 Numerical Implementation 9

2.4 Proper Orthogonal Decomposition 12

2.4.1 Formulation 12

2.4.2 Deflation 16

2.4.3 Accuracy 19

2.5 ROM 33

2.5.1 Results 34

2.6 Conclusions 41

3 Proper Orthogonal Decomposition Based Reduced Order Models for Low and High Reynolds Flows **43**

3.1 Introduction 43

3.2 Detailed Solutions 47

3.2.1 Problem Description 47

3.2.2 Governing Equations 48

3.2.3 Numerical Method 49

3.3 Proper Orthogonal Decomposition for Fluid Flow 50

3.4 Reduced Order Modeling 52

- 3.4.1 Galerkin ROM 52
- 3.4.2 Streamwise-Upwind-Petrov-Galerkin (SUPG) ROM 53
- 3.4.3 Spectral Vanishing Viscosity ROM 54
- 3.5 Low Reynolds Case 55
  - 3.5.1 Results for Galerkin ROM 60
  - 3.5.2 Results for SUPG ROM 62
  - 3.5.3 Results for SVV ROM 65
- 3.6 High Reynolds Number Case 66
  - 3.6.1 Mode generation 68
    - 3.6.1.1 Effect of Time Window 68
    - 3.6.1.2 Effect of Snapshot Interval 76
    - 3.6.1.3 Effect of Domain Size & Angle of Attack 76
  - 3.6.2 ROMs 78
    - 3.6.2.1 Effect of Time Window 79
    - 3.6.2.2 Effect of Number of Modes 83
    - 3.6.2.3 Effect of Stabilization 85
    - 3.6.2.4 Effect of domain size 87
- 3.7 Conclusions 89

4 Proper Orthogonal Decomposition Based Reduced Order Modeling for Transient Flow 92

- 4.1 Introduction 92
- 4.2 Detailed Solution 97
  - 4.2.1 Problem Description 97
  - 4.2.2 Governing Equations 98
  - 4.2.3 Numerical Method 99
  - 4.2.4 Actuator Description 100
- 4.3 Reduced-Order Modeling Based on a POD Galerkin Approach . . . 100
  - 4.3.1 Proper Orthogonal Decomposition 100
  - 4.3.2 Low-dimensional Model 102
- 4.4 Parameter Changes in the Proper Orthogonal Decomposition 102
  - 4.4.1 Global Proper Orthogonal Decomposition (GPOD) 103
  - 4.4.2 Double Proper Orthogonal Decomposition (DPOD) 103
  - 4.4.3 Recursive Proper Orthogonal Decomposition (RPOD) 106
- 4.5 Results 109
  - 4.5.1 RPOD Versus GPOD 109
  - 4.5.2 MPOD 113
- 4.6 Conclusion 114

5 Summary, Conclusions, and Recommendations for Future Work 116

- 5.0.1 Conclusion 117
  - 5.0.1.1 Proper orthogonal decomposition based reduced order modeling for burger equation 117
  - 5.0.1.2 On the robust proper orthogonal decomposition based reduced order modeling 118

5.0.1.3 Proper orthogonal decomposition based reduced order modeling for transient fluid flows 119
5.0.2 Recommendations for future work 120

Bibliography **122**

List of Figures

2.1 Typical solution of Burgers' equation at $t = 0.0, 0.15, 0.30$ and 0.45s second for initial condition (a)$1 + \sin(2\pi x)$ and (b)$1 + \exp(\sin(4\pi x))$. 11

2.2 Norm 2 of Burgers' equation solution by Fourier simulation (a) and Finite Element(b) for initial condition $1 + \sin(2\pi x)$ (solid line) and $1 + \exp(\sin(4\pi x))$ (dash line). 12

2.3 Energy distribution of POD modes, Direct method without deflation (solid line), Snapshots method (dashed line), direct method with deflation (□) and snapshot method with deflation (○). Initial condition is $1 + \exp(\sin(4\pi x))$. a) N=100 b) N=400. 20

2.4 Orthogonality of POD modes for initial condition $1+\exp(\sin(4\pi x))$, (a) Direct method without deflation, (b) Direct method with deflation, (c) Snapshot method using 100 snapshots, without deflation, (d) Snapshot method using 100 snapshots, with deflation. 25

2.5 Out of plane error of the initial condition, $\|e_o(0)\|$. Direct method without deflation (—), snapshot method without deflation (- -), direct method with deflation (□), snapshot method with deflation (○). 26

2.6 Out of plane error of initial condition $\|e_o(0)\|$. Direct method with deflated coefficients (—), snapshot method with deflated coefficients (- -), direct method with deflation (□), snapshot method with deflation (○). 27

2.7 Eigenvalues, λ, and out of plane error of the initial condition, $e_o(0)$, for $1 + \exp(\sin(4\pi x))$. Direct method without deflation (solid line), snapshot method without deflation constructed using 50 (boxes), 100 (circles), 200 (triangles), 400 (diamonds), and 800 (crosses) snapshots. 28

2.8 Error in eigenvalues 3, 7, and 11 versus the number of snapshots. Left figure compares two grid resolutions, $N_e = 100$ (dotted line) and $N_e = 400$ (dashed line) at $\nu = 5 \times 10^{-3}$. Right figure compares two viscosities, $\nu = 5 \times 10^{-3}$ (dotted line) and $\nu = 1 \times 10^{-4}$ (solid line) at $N_e = 400$. In both figures, the thick dash-dotted line shows second order convergence. 30

2.9 Integrated out of plane errors (lines) and the summation of the truncated eigenvalues (symbols) for the: direct method (solid line, boxes) and snapshot method with 100 snapshots (dashed line, circles). 32

2.10 Comparison between detailed FEM (solid line) and 10 dimensional POD-ROM (dash line) simulation of Burgers equation for initial condition $1 + \exp(\sin(4\pi x))$. 35
2.11 Maximum L_2 error of Fourier method (dotted line), POD-ROM simulation straight Galerkin (solid line) and POD-ROM simulation using SUPG stabilization (dashed line). 37
2.12 Total error, $e_t(t)$, and out-of-plane error, $e_o(t)$, for Galerkin (solid line, boxes) and SUPG stabilized (dashed line,circles) POD-ROMs for low grid based Reynolds number. 38
2.13 Total error, $e_t(t)$, and out-of-plane error, $e_o(t)$, for Galerkin (solid line, boxes) and SUPG stabilized (dashed line,circles) POD-ROMs for high grid based Reynolds number. 39
2.14 Total error (curves) and out-of-plane error (symbols) of SUPG stabilized POD-ROM simulations: direct method (solid line, circles) and snapshot method with 100 snapshots (dotted line, triangles). . 40

3.1 *hp*-Finite element mesh for low Reynolds case study, Re=1000 (chord length of the NACA0015 airfoil=1; Radius of domain=10.) 48
3.2 Instantaneous u-velocity contours, $Re = 1000$. 58
3.3 Instantaneous u and v velocity at probe location, $Re = 1000$. 58
3.4 POD mode eigenvalues with $N_s = 120$ (−■−) and $N_s = 60$ (○). $1/N^2$ convergence (solid line). 59
3.5 Representation of some POD modes. u velocity POD modes (left) and v velocity POD modes (right). Dashed lines show the negative values. 60
3.6 Envelopes of C_D of detailed simulation (solid lines) and C_D of 4 Galerkin POD-ROM cases from table 3.2 (gray). 61
3.7 Envelopes of C_D of detailed simulation (solid lines) and C_D of 4 SUPG based POD-ROM cases from table 3.2 (gray). 62
3.8 Contour of $\sqrt{(u_{Detailed} - u_{ROM})^2 + (v_{Detailed} - v_{ROM})^2}$ after 230 shedding cycles. 63
3.9 Temporal evolution of the predicted POD-ROM coefficients in comparison with projected over detailed simulation. Detailed simulation(—), 15 modes simulation (−■−), 21 modes simulation (−▲−) and 15 modes simulation without stabilization (···). 64
3.10 C_D of detailed simulation (gray line) and envelopes of C_D of SVV simulations for the different values of K and ϵ given in table 3.3. . . 66
3.11 *hp*-Finite element mesh (chord length of the NACA0015 airfoil=1; Radius of domain=10.) 68
3.12 Contour of instantaneous u and v-velocity field from detailed simulation. 69
3.13 POD mode eigenvalues with different time length (number of snapshots) for case study 1. 70
3.14 POD mode eigenvalues with different time length (number of snapshots) for case study 3. 72

3.15 Case study 1, number of POD modes needed to capture 90% (dashed) and 99% (solid) of the energy as a function of the length of the time window T. 73
3.16 Representation of first POD mode (mode 0) of case study 1 for different non-dimensional time windows, (a) and (b) for $T = 3.125$, (c) and (d) for $T = 11.25$, and (e) and (f) for $T = 30$. u velocity POD modes (left) and v velocity POD modes (right). 74
3.17 Representation of second POD mode (first fluctuating mode) of case study 1 for different non-dimensional time windows, (a) and (b) for $T = 11.25$, and (c) and (d) for $T = 30$. u velocity POD modes (left) and v velocity POD modes (right). 75
3.18 Representation of sixth POD mode (fifth fluctuating mode) of case study 1 for different non-dimensional time windows, (a) and (b) for $T = 11.25$, and (c) and (d) for $T = 30$. u velocity POD modes (left) and v velocity POD modes (right). 75
3.19 POD mode eigenvalues with different N_p for time window 26.25, case study 1. 77
3.20 Contour of instantaneous u-velocity field from detailed simulation, angle of attck 9°. 78
3.21 Case study 1, C_D of detailed simulation (black line), SUPG POD-ROM simulation with $N_r = 49$ for $T = 0.625$ (dashed line), and SUPG POD-ROM simulation with $N_r = 49$ for $T = 3.125$. (dotted line). 80
3.22 Case study 1, C_D of detailed simulation (black line), SUPG POD-ROM simulation with $N_r = 49$ for time window 3, $T = 6.25$ (dashed line), and SUPG POD-ROM simulation with $N_r = 49$ for time window 4, $T = 11.25$ (dotted line). 82
3.23 Contour of u velocity, (a) u_{Detailed} (b) u_{ROM} 83
3.24 Case study 1, C_D of detailed simulation (black line) SUPG POD-ROM simulation with $N_r = 49$ (dashed line) and $N_r = 29$ (dot-dashed line) for time window 2, $T = 3.125$. 84
3.25 Case study 1, C_D of detailed simulation (black line) SUPG POD-ROM simulation for time windows 4 ($T = 11.25$) with $N_r = 89$ (dotted line) and $N_r = 175$ (dashed line). 85
3.26 C_D of detailed simulation (black line), SUPG POD-ROM with $N_r = 49$ (dashed line) and Galerkin POD-ROM with $N_r = 49$ (dotted line) from time window 2, $T = 3.125$. 87
3.27 C_D of detailed simulation (black line), SUPG POD-ROM, $N_r = 49$, time window 2 (dotted line) and time window 4 (dashed line) . . . 89

4.1 *hp*-Finite element mesh, resolved in wake region and high resolved around jet region. ($Re = 1000$, chord length of the NACA0015 airfoil=1; Radious of domain=10.) 98
4.2 Pictorial representation of the GPOD procedure. 104
4.3 Pictorial representation of the DPOD procedure. 105
4.4 Pictorial representation of the MPOD procedure. 105

4.5 Eigenvalues of POD using all snapshots (solid line), eigenvalues of four detailed simulations (dashed line). 110
4.6 Eigenvalues of POD using all snapshots (solid line), eigenvalues of RPODs with cut-off M = 50, 75, 100, and 110 (dashed line). . . . 111
4.7 Eigenvalues of POD using all snapshots (solid line), eigenvalues of GPOD using N_s = 220 and 440 (dotted line) and, RPOD using cut-off number of $N_{cut-off}$ = 55 and 110 (dashed line). 112
4.8 Comparison of the drag coefficient, detailed simulation with A=u_∞ (solid lines), POD-ROM using GPOD modes with A=$-u_\infty$ (dashed lines), and POD-ROM using RPOD modes with A=$-u_\infty$ (dotted lines). 113
4.9 Comparison of the drag coefficient, detailed simulation with A=u_∞ (solid lines), detailed simulation with A=$-1/2u_\infty$ (dash-dotted lines), POD-ROM using MPOD basis with A=$-1/2u_\infty$ (dotted lines), POD-ROM using MPOD basis with A=u_∞ (dashed lines). 114

List of Tables

3.1 POD-ROM characteristics 56
3.2 Normalized energy summation for low Reynolds number case 57
3.3 Brief description of the different SVV-ROMs for comparison of SUPG and SVV 65
3.4 POD-ROM characteristics 67
3.5 Number of fluctuating POD mode needed to capture 99% of energy 78
3.6 Mean and standard deviation of simulation of section 3.6.2.1 80

Abbreviations

DNS	**D**irect **N**umerical **S**imulation
DPOD	**D**ouble **P**roper **O**rthogonal **D**ecomposition
EOF	**E**mperical **N**rthogonal **F**unction
GPOD	**G**lobal **P**roper **O**rthogonal **D**ecomposition
LES	**L**arge **E**ddy **S**imulation
MPOD	**M**ultilevel **P**roper **O**rthogonal **D**ecomposition
ODE	**O**rdinary **D**ifferential **E**quation
POD	**P**roper **O**rthogonal **D**ecomposition
ROM	**R**educed **O**rder **M**odeling
RPOD	**R**ecursive **P**roper **O**rthogonal **D**ecomposition
SUPG	**S**treamwise **U**pwind **P**etrov **G**alerkin
SVV	**S**pectral **V**anishing **V**iscosity

Chapter 1

Introduction

Fluid flow dynamics is rather complicated and has a rich class of solution due to the nonlinear nature of its governing equation. The nonlinearity in the flow velocity originates from the convective transport and the pressure term which is also nonlocal. The nonlinearity has a fundamental significance in aerodynamic and hydrodynamic applications where real time and spatially resolved simulations of the governing equations are needed. Accurate representation of the flow field typically requires large grids covering the computational domain, which leads to many degrees of freedom (or modes). Typical finite element/finite volume method may require many thousands/millions of elements/control volumes and consequently, requires massive computational resources. On the other hand, a number of practical engineering problems including flow control, optimization and uncertainty quantification of fluid systems, require repeated simulations of the unsteady fluid flows. The huge computational cost and the necessity of fast and numerous simulations brings up the natural question that whether or not it is necessary and/or practical to accurately produce the entire features of the flow details for complex systems? One possibility to make many of these flow analyses practical is to use the reduced-order models to significantly reduce the required simulation effort. Among various types of reduced-order models, the one that is of interest to complex fluid systems using very few degrees of freedom is the proper orthogonal decomposition (POD) approach. The POD is also known as the Karhunen-Loeve expansion in the field of statistics and principal component analysis or empirical orthogonal functions (EOF) in meteorology. The approach decomposes the flow parameters based on their energy content meaning that the computed POD modes are energetically optimized in mean square sense. Therefore, POD makes it possible to reconstruct a nonlinear process by a linear combination of limited number of main modes. Order reduction of the equations is accomplishes by projecting the governing equation onto a finite but optimal number of the POD basis functions and solving the resulting ODEs. For nonlinear, time-dependent fluid flow problems governed by the Navier-Stokes equations, the reduced-order models are typically constructed from two steps. First, a series of the detailed simulations are performed and the desired variable is mapped to a finite number of basis functions or modes. The span of these modes forms a subspace. Second step is Galerkin projection of the Navier-Stokes equations onto a span of small number of dominant POD modes. Thereby the distributed-parameter problem is reduced into a set of finite-dimensional nonlinear dynamical system in time.

1.0.1 Objectives

A comprehensive assessment of the numerical accuracy of POD representation has been rarely addressed. The general objective of this thesis is to assess the accuracy of the proper orthogonal decomposition of flow around an airfoil for active flow control applications. The specific Objectives are:

- Assessing the effect of truncation and stabilization on the accuracy of POD based reduced order model.
- Developing a robust POD-ROM for long term simulation of Navier-Stokes equation. This includes assessing the ability of the POD-ROM to simulate an unactuated low Reynolds and high Reynolds flow over an airfoil.
- Developing a new multi-level POD method capable of managing large eigenvalue problems, generating the enriched POD modes in terms of information, that are capable of describing transient flows.

The thesis is organized as follows:

1. An introduction to the reduced order models and proper orthogonal decomposition is provided in the introduction section.
2. Chapter two of this study is devoted to inspection of the numerical error of POD and the associated ROM, including round off error and error of truncation of POD modes. A 1D Burgers equation, which involves both convection and diffusion, is first studied. A series of numerical investigation consisting of the sensitivity of the eigenvalues and POD modes to truncation and round-off errors is performed. Then, the effects of POD mode quality, ROM stabilization, and ROM dimension on the accuracy of ROMs for low- and high-Reynolds number simulations are examined. The interplay between the data that the straight Galerkin and SUPG POD modes are derived from and the methods used to derive the ROM is also investigates in Chapter 2.
3. In Chapter 3, testing the long time stability and robustness of POD-ROM for an incompressible viscous flow at low and high Reynolds number are presented. For the case of low Reynolds flows, comparisons of the performance of the Galerkin POD-ROM, streamwise-upwind-Petrov-Galerkin (SUPG) POD-ROM and, spectral-vanishing-viscosity (SVV) POD-ROM are done. After obtaining accurate results using the SUPG POD-ROM for periodic flows at low Reynolds numbers, the flows at high Reynolds numbers are analyzed and tested. This provides information on the capability of POD for complex non-periodic viscous flow. Detailed analysis for a 2-D flow around the airfoil at a high Reynolds number is performed. It is found that for non-periodic fluid flow, long time detailed simulation is needed to derive the POD modes. Also, including the high dimension of POD-ROM is crucial to obtaining accurate result.
4. Chapter 4 is focused on the ability of POD-ROM for predicting the transient flow conditions around the airfoils. When POD is evaluated from the data for a certain time interval for example unactuated or actuated airfoils, the

resulting spatial POD modes and the corresponding ROM fatefully represent the flow field only over this temporal interval. That is the subspace spanned by POD modes only portrays the unactuated flow regime, if the modes are generated for this period. But during active flow control, the flow changes from the condition of unactuated airfoil to a different flow under the actuation conditions. The POD that is generated for the unforced airfoil is not appropriate for generating the transient flow condition and or the actuated flow. Therefore, there is a need for generating set of POD modes that the resulting ROM produces accurate results over a wide range of flow conditions. Accordingly, in Chapter 4 the procedure for developing a set of enriched POD modes that is capable of covering a wide range of transient flow conditions is described. As noted before, the standard methods for generating POD-ROM does not lead to accurate results. A new novel approach using the energy weighted PODs to generate the optimal enriched POD is introduced. The new approach allows solving a manageable eigenvalue problem that leads to enriched POD modes. Comparisons between the performances of the new method with the standard POD-ROM methods are presented.

Chapter 2

POD-ROM

2.1 Introduction

Numerical simulation of the Navier-Stokes Equations (NSE) typically requires enormous computational resources. Even with current significant increase in computational power, it is still basically impossible to solve many practical flow problems accurately and even more difficult to do this in real time. The main difficulty is the large number of degrees of freedom needed to resolve all of the flow features. In order to obtain real-time solutions, which are often needed for flow control problems, one solution is to use the reduced order models (ROM). The idea of reduced order modeling is to perform detailed, time consuming simulations ahead of time, then use this information to generate a predictive and fast model which can be used for real-time prediction of the response of a system to some time varying input. An extensive review of ROM techniques was reported in [1].

Among the various ROM techniques, the proper orthogonal decomposition (POD)-based reduced order modeling has attracted considerable attention for application to fluid flow anlaysis. The goal of POD-ROM is to reduce the number of degrees of freedom necessary for numerically solving a system of partial differential equations by introducing spatial basis functions specifically adapted to the system. When using finite volume, finite difference, finite element, or spectral methods to solve the Navier-Stokes equations, the basis functions typically have little connection with the problem being solved and thus it requires many functions to represent the solution. The POD [2] (also known as the Karhunen-Loeve (KL) expansion [3, 4]) generates the basis functions from either numerical simulations of the system or from experimental data. These POD basis functions, called POD modes, are then used with a Galerkin projection to construct a set of ODEs that predict the flow behavior. Because the POD modes are generated specifically for an individual flow, one can often generate an accurate model of that flow using only a small number of modes.

Although POD-ROM should be able to simulate complex systems efficiently, recent work has shown that these models often suffer from a lack of accuracy specially for long-time simulations [5–10]. This is true even when using what seems like a sufficient number of modes, enough to capture most of the energy of a system. Possible reasons for this are suggested in [8–10]. One potential reason for loss of accuracy is that the truncation involved in the POD-Galerkin approach omits the modes through which energy dissipation occurs. This then leads to a lack of robustness in the models. o remedy this difficulty, several modifications to the Galerkin projection method have been suggested. In particular, the use of “eddy viscosity” to account for energy dissipation has attracted attention. Aubry et al. [5] used a mixing-length-based eddy viscosity for their analysis. Podvin [11] improved the same model and concluded low-dimensional models are able to capture some key features of near-wall turbulent flows. Sirisup and Karniadakis [6] used the idea of Spectral Vanishing Viscosity (SVV) to add dissipation to their model. Another approach is to calibrate the evolution of the POD-ROM coefficients using the correct coefficients derived from detailed simulations [7, 8, 12]. An example is the least-squares calibration method [7]. In this method correction terms are added to the dynamical model to force the ROM simulation toward the data of the detailed simulation. Although this approach can repredict a DNS, it is unclear whether it will be accurate for varying flow conditions and inputs. Another approach is large-eddy-simulation-based POD-ROM, which takes take into account the effect of mode truncation by incorporating an LES-type subgrid-scale model [13]. Wang et al. [10] tried this approach, replacing the grid scale in the Smagorinsky subgrid-scale model with a scale related to the truncated modes.

The purpose of the chapter is two-fold; The first goal of the work is to determine the importance of numerical errors on the POD and ROM process; the POD problem is often significantly affected by numerical round-off errors, and it is important to assess how these round-off errors affect the robustness of the ROM. In almost all previous work, the effect of round-off errors in the POD process are ignored. Furthermore, for numerical expediency, reduced data sets are often used to generate the POD modes instead of using all available data. Here we explicitly assess the magnitude of these errors and their impact on the derived ROM.

The Second goal of the study is to investigate the importance of stabilization or dissipation in creating robust POD-ROM models. To do this, we will examine Burgers' equation which involves both convection and diffusion and investigate the interplay between the data that the modes are derived from and the methods used to derive the ROM. Kunisch and Volkwein [14] gave a combined temporal and POD error estimate for ROMs of Burgers' equation, but they did not consider the effect of stabilization. Borggaard, Iliescu and Wang [15] performed a similar analysis on a ROM derived with artificial viscosity as a stabilization method. . However, their error analysis of the POD reduction was intertwined with the temporal errors so it is not easy to understand the ROM errors. Luo, Zhou and Yang [16] performed a combined analysis of spatial errors and ROM errors for an unstabilized formulation of the Burger's equation. Finally, Nguyen, Rozza and Patera [17] presented a posteriori error bounds for reduced order model of the unsteady viscous Burgers' equation, but their 1-D case did not really involve convective solutions which makes it difficult to determine the importance of stabilization on the results. The goal of this work is to determine the effect of stabilization on the ROM process without also considering other effects like spatial or temporal resolution. To this end, we assume that the FEM solutions are the "truth" and examine how stabilized and unstabilized ROMs converge to these solutions as the number of degrees of freedom in the models are increased.

The chapter is organized as follows: Section 2.2 describes the physical problem studied and the following section details the methods used to obtain the exact detailed solutions. The next section describes the reduced order modeling process. First, the Proper Orthogonal Decomposition (POD) and the "deflation" POD are introduced, and the effects of various errors in the POD process are assessed. In section 2.5 talks briefly about the methods of generating reduced order models using a given set of modes and the stabilization of POD based reduced order model are discussed. The last section examines the necessity of introducing stabilization to improve the accuracy of the POD-ROM model for high grid based Reynolds number. Also, it provides some notes on the effect of quality of POD modes on the reduced order results.

2.2 Problem Formulation

Burger's equation is a useful 1D model due to its incorporating both the nonlinear convective term as well as diffusive effect. In this section, the reduced-order modeling approach based on POD is applied to a one-dimensional Burgers' equation,

$$\mathcal{L}\left(u\right) = \left(\frac{\partial u}{\partial t} + u\frac{\partial u}{\partial x} - \nu\frac{\partial^2 u}{\partial x^2}\right) = 0 \quad in \quad \Omega,$$

where u is the solution variable and ν is the diffusivity. The spatial domain (Ω) is taken as $x \in [0, 1]$ with periodic boundary conditions. The temporal domain is $t \in [0, 3]$. For initial conditions, we use either a sinusoidal function with a period equal to the domain length $1 + \sin(2\pi x)$ or a periodic function containing a wider Fourier spectrum,

$$u(x, 0) = 1 + \exp(\sin(4\pi x)). \tag{2.1}$$

are used. These initial conditions give rise to localized features that propagate through the domain, thus they are a difficult test of reduced order modeling techniques.

2.3 Numerical Implementation

To generate solutions to the above problem, we use two different numerical techniques, finite element and Fourier methods. Both methods project the partial differential equation onto a finite dimensional subspace thus resulting a system of ODEs. However, the finite element method and Fourier method have significantly different basis function (C^0 versus C^∞ continuous functions) and convergence rates. We primarily focus on data from the finite element method. The Fourier method is used to provide a baseline of comparison for the ROMs.

A streamwise-upwind-Petrov-Galerkin variational (SUPG) approach is used for the finite element formulation [18],

$$\left(\phi + u\tau\frac{\partial \phi}{\partial x}\,,\ \frac{\partial u}{\partial t} + u\frac{\partial u}{\partial x}\right) + \left(\frac{\partial \phi}{\partial x},\ \nu\frac{\partial u}{\partial x}\right) = 0, \tag{2.2}$$

$(.,.)$ is the standard Euclidean inner product, ϕ is a test function, u is the solution variable, and τ is a stabilization parameter, given by

$$\tau = \frac{1}{\left|\frac{2u}{\Delta x}\right| + \frac{4.0\nu}{\Delta x^2}}, \tag{2.3}$$

where Δx is the mesh spacing. The domain is discretized into N_e equal length elements where N_e varies depending on the case. The solution u and the test functions are chosen from the space $\mathcal{S}$, which is a standard piecewise linear, continuous finite element space. To integrate Eq. (2.2), a 2-point Gaussian quadrature rule is used on each element. The initial conditions for FE simulations are evaluated using an L_2 projection that requires a mass matrix inversion. The integrals in the L_2 projection are also calculated using the 2-point Gaussian rule.

The Fourier method uses a Fourier expansion of the solution,

$$u(x,t) = \sum_{n=-N_f/2}^{N_f/2-1} \hat{u}_n(t)\exp(ik_n x).$$

where $k_n = 2\pi n$ and N_f is the number of terms kept in the trigonometric series (written in complex exponential form). This expansion is substituted into a Galerkin weighted integral form of the governing equation to derive a system of ordinary differential equations for the time-dependent coefficients. All integrals in the Galerkin formulation are evaluated exactly; numerical integration is not used. Two different methods for calculating the initial conditions are used. For the initial condition $u = 1 + \sin(2\pi x)$, an exact initial condition can be specified. For the case $u = 1 + \exp(\sin(4\pi x))$, initial Fourier coefficients can be calculated using standard fast Fourier transform subroutines. The most exact Fourier simulation contains 512 modes. By comparing results between the two initial condition cases, we can determine whether initial condition error has any impact on the results.

We note that there is little difference between a SUPG and Galerkin formulation when using a Fourier expansion. An upwind weighted test function, $\phi + u\tau\partial\phi/\partial x$, becomes $\exp(ik_nx) + u\tau ik_n \exp(ik_nx) = (1 + u\tau ik_n)\exp(ik_nx)$ when ϕ is chosen from the Fourier space. In the pure convection case, $u\tau = \Delta x \text{ sign}(u)/2$, thus the SUPG test function and the Galerkin test functions only differ by a multiplicative constant as long as u doesn't change sign. Because this multiplicative constant does not change the discrete equations, the results of the two formulations are identical. For diffusive cases, there is a slight difference because $u\tau$ is not strictly constant. If the problem were linear with a constant convection speed, a, the Galerkin and SUPG formulations would give identical results independent of viscosity. Thus SUPG stabilization is not necessary when a Fourier method is used.

For both the finite element and Fourier methods, the standard 4^{th} order Runge-Kutta scheme is used to advance the solutions in time with $\Delta t = 1.25 \times 10^{-5}$. This value is much (at least 10 times) smaller than that required by stability, $\Delta t = (|2u/dx| + 4.0\nu/dx^2)^{-1}$, for the most-resolved finite element simulation used in the results. The time step is held fixed for all simulations so we can eliminate temporal discretization error when comparing solutions derived using different spatial basis functions (either reduced-order, FEM, or Fourier bases).

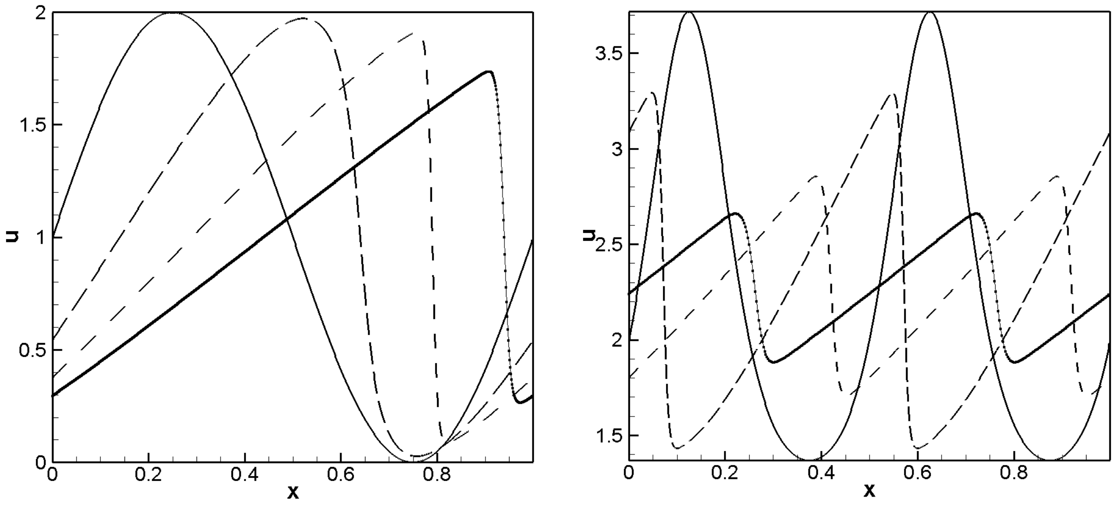

(a) (b)

Figure 2.1: Typical solution of Burgers' equation at $t = 0.0, 0.15, 0.30$ and 0.45s second for initial condition (a)$1 + \sin(2\pi x)$ and (b)$1 + \exp(\sin(4\pi x))$.

To give an example of the behavior of the solution, Fig. 2.1a and Fig. 2.1b show solution profiles at $t = 0, 0.15, 0.30$ and 0.45 for the two different initial conditions. These are Fourier solutions with 512 modes and obtained with ν equal to 0.005. For both initial conditions, by $t = 0.3$ the solutions develop a steep propagating front. With 512 modes, the spatial resolution is on the order of 1.95×10^{-3} so that this front is well-resolved; the difference in position between the maximum and minimum around the front is approximately 6.0×10^{-2}, which is 30 times greater than the spatial resolution.

Convergence of the FE and Fourier method are depicted in Fig. 2.2. As expected the Fourier method converges exponentially with the number of modes used. Extrapolating the error curve to 512 modes, one can estimate that the error in the 512 mode solution is roughly 5 orders of magnitude smaller than even the Fourier solution with 256 modes. The SUPG FE solutions converge with the rate of $\Delta x^{1.5}$, which is what is expected for a convection dominated problem [18]. Temporal error is not important because all simulations are done with the same time step and time advancement scheme.

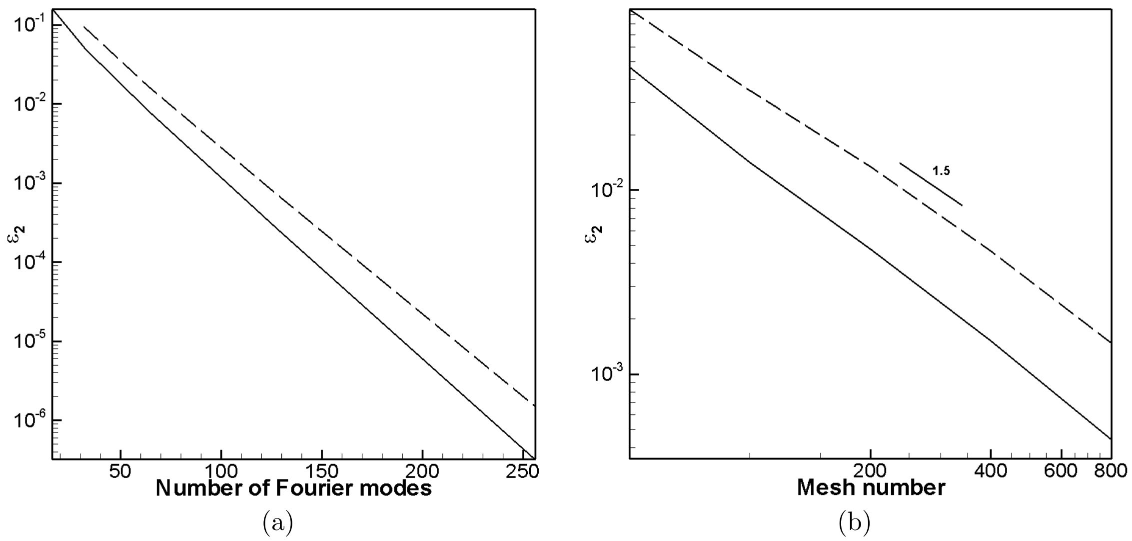

Figure 2.2: Norm 2 of Burgers' equation solution by Fourier simulation (a) and Finite Element(b) for initial condition 1+sin($2\pi x$) (solid line) and 1+exp(sin($4\pi x$)) (dash line).

2.4 Proper Orthogonal Decomposition

2.4.1 Formulation

The bases for the reduced order models are derived from the detailed data using the proper orthogonal decomposition (POD). The POD was introduced by Lumley [2] as a means to extract the large scale structures of turbulent flows. It uses data obtained from experiments or numerical simulations to generate an orthogonal set of spatial basis functions. These functions, herein called POD modes, optimally represent the flow; the mean square inner product of the solution with a POD mode is maximized. With an adequate number of POD modes, we can approximate any solution as a linear combination of time-dependent weighting coefficients, $a_n(t)$, and the POD modes, $\Phi_n(x)$.

$$\begin{aligned} u(x,t) &= \sum_{n=1}^{M} a_n(t)\Phi_n(x) \\ &= \sum_{n=1}^{M} \left(u(x,t), \Phi_n(x)\right) \Phi_n(x). \end{aligned} \tag{2.4}$$

The POD modes are eigenfunctions of the following Fredholm integral equation

$$\int_{\Omega} R(x,x')\Phi_n(x')dx' = \lambda_n \Phi_n(x), \tag{2.5}$$

where

$$R(x,x') = \langle u(x,t)\ u^*(x',t)\rangle, \tag{2.6}$$

is the time-averaged correlation tensor. The angled brackets indicate a time average and u^* is the complex conjugate. An outcome of these definitions is that the mean squared variation captured by the n^{th} POD mode $\Phi_n(x)$ is

$$\frac{1}{T}\int_0^T a_n(t)^2 dt = \lambda_n.$$

and the $a_n(t)$ are uncorrelated (orthogonal) variables in time.

Since both the finite element and Fourier solutions can be written as a linear combination of coefficients and basis functions ($u(x,t) = \sum_j \hat{u}_j(t)\phi_j(x)$ where $\phi_j(x)$ is either the Finite element basis functions or the Fourier modes), it is convenient to derive a general eigenvalue problem formulation which is suitable for both cases. In this case, the integral Eq. (2.5) becomes a discrete eigenvalue problem. Note that for the finite element formulation, the $\hat{u}(t)$ are real coefficients and j varies from 1 to the number of basis functions, N_e, while for the Fourier modes the $\hat{u}(t)$ are complex and j varies from $-N_f/2$ to $N_f/2-1$. For either case, substituting in Eq. (2.5), the eigenvalue problem becomes

$$\int \langle \sum_j \hat{u}_j(t)\phi_j(x)\ \sum_i \hat{u}_i^*(t)\phi_i^*(x')\rangle \Phi_n(x')dx' = \lambda_n \Phi_n(x),$$

Furthermore, the POD modes can be constructed as linear combinations of the solution basis functions, $\Phi_n(x) = \sum_j v_{jn}\phi_j(x) = \phi^T V_n$. Factoring $\phi(x)$ from both sides, the results in tensorial notation becomes:

$$\phi^T(x)\left(\langle \int \hat{u}(t)\hat{u}^{*T}(t)\phi^*(x')\phi^T(x')V_n dx'\rangle = \lambda_n V_n\right).$$

This becomes

$$\langle \hat{u}(t)\hat{u}(t)^{*T}\rangle MV = \lambda V,$$

where the mass matrix M is defined as

$$M = \int \phi^*(x')\phi^T(x')dx'.$$

For the Fourier basis, the mass matrix is diagonal, while for the FEM basis in 1D, the mass matrix is tridiagonal. To make the eigenvalue problem symmetric, we multiply both sides by M,

$$M\langle \hat{u}(t)\hat{u}(t)^*\rangle MV = \lambda MV, \tag{2.7}$$

This system can then be solved with standard eigenvalues solvers such as Lapack's DGEEV or SVGED.

This method of mode generation is known as the direct method. Independent of whether the data comes from FEM or a Fourier simulation, we need to construct the time-averaged correlation tensor (covariance matrix) of the FEM or Fourier solution coefficients and find the eigenvalues and eigenvectors of this matrix. For the Fourier method, the dimension of $\langle \hat{u}^T\hat{u}\rangle$ in Eq. (2.7) is equal to number of Fourier modes, N_f, while it is equal to number of elements, N_e, for the finite element approach. Thus, the eigenvalue problem becomes difficult when a fine grid is used because the matrix is full and the dimension of the matrix is equal to the dimension of grid.

To overcome this problem, Sirovich [19] developed the snapshot method. The main idea of this method is to write the POD modes as a linear combination of snapshots of the instantaneous flow field. That is,

$$\Phi_n(x) = \sum_{m=1}^{N_s} u(x, t_m)\Psi_{m,n},$$

where the sum is performed over the number of snapshots, N_s, used in the discrete time average for Eq. (2.6). By substituting this equation into Eq. (2.4), the following analogous eigenvalue problem is obtained:

$$C\ \Psi_n = \lambda_n \Psi_n, \tag{2.8}$$

whose discrete matrix entries are given as

$$C_{lk} = \frac{1}{N_s} \int_{\Omega} u(x, t_l) u(x, t_k)^* dx. \tag{2.9}$$

Plugging the numerical expansion of u into Eq. (2.9) and then substituting the result into Eq. (2.8) gives

$$\frac{1}{N_s} \left(\hat{u}^T(t_l) \int \phi^T(x)\phi(x)^* dx \hat{u}(t_k)^* \right) \Psi_n = \lambda_n \Psi_n,$$

in vectorial notation,

$$\frac{1}{N_s} \left(\hat{u}^T(t_l) M \hat{u}(t_k)^* \right) \Psi_n = \lambda_n \Psi_n,$$

This method involves solving an eigenvalue problem that has a dimension N_s. Thus, the snapshot method is computationally more efficient whenever the number of snapshots, N_s, is smaller than the number of elements, N_e.

For either of the above approaches, standard LAPACK routines can be used for finding the eigenvalues and eigenvectors which then can be used to reconstruct the POD modes.

2.4.2 Deflation

There are several numerical difficulties associated with both the snapshot and direct methods of finding the POD modes, which are often overlooked. As each eigenvalue of the POD decomposition represents the energy captured by that specific mode, the eigenvalue spectrum typically spans many orders of magnitude. Such eigenvalue problems often give rise to large numerical errors in the calculation of the eigenvalues and eigenvectors. In this section, we propose an alternative approach to calculate the POD modes that helps eliminate some of the numerical errors and compare the errors of the various methods from both a theoretical and numerical perspective.

The new method for calculating the POD modes relies on the fact that the POD modes are a hierarchal series of orthogonal functions. Rather than relying on the eigenvalue solver to create eigenvectors that produce modes that satisfy this property, we generate the modes sequentially so that we can explicitly control the orthogonality of the derived POD modes.

The basic idea is as follows

step 1. Compute the dominant eigenvalue and eigenvector using either of the two methods described above (direct or snapshot). Use this eigenvector to generate the corresponding POD mode.

step 2. For each solution snapshot, generate new snapshots by subtracting the projection of the snapshot onto the mode as follows

$$u_{new}(x,t) = u(x,t) - (u(x,t), \Phi_1(x))\Phi_1(x).$$

step 3. Return to step 1 using the new solution snapshots to find the next mode.

Because the new snapshots are explicitly made orthogonal to the POD mode, any mode found using the new snapshots should be orthogonal to the previous POD modes to machine precision (proof given below). This is also true of standard approaches. In the results, we examine the outcomes using both approaches.

To see that the above procedure gives the same POD modes, let us examine the POD problem that is created when using the new snapshots. Plugging in $u(x,t) - a_1(t)\Phi_1(x)$ for u in Eq. (2.5) where $a_1(t) = (u(x,t), \Phi_1(x))$ gives

$$\int_\Omega \langle (u(x,t) - a_1\Phi_1(x))(u^*(x',t) - a_1^*\Phi_1(x')^*)^T\rangle \Phi_n(x')dx' = \lambda_n\Phi_n(x),$$

Expanding the left hand side, it follows that

$$\begin{aligned}
&\int_\Omega R(x,x')\Phi_n(x')dx' \\
&- \int_\Omega \langle a_1(t)\Phi_1(x)(u^*(x',t))^T\rangle \Phi_n(x')dx' \\
&- \int_\Omega \langle u(x,t)(a_1^*(t)\Phi_1^*(x'))^T\rangle \Phi_n(x')dx' \\
&+ \int_\Omega \langle a_1(t)\Phi_1(x)(a_1^*(t)\Phi_1^*(x'))^T\rangle \Phi_n(x')dx' = \lambda_n\Phi_n(x).
\end{aligned}$$

Now substituting $u(x,t) = \sum a_i(t)\Phi_i(x)$ this becomes

$$\begin{aligned}
&\int_\Omega R(x,x')\Phi_n(x')dx' \\
&- \Phi_1(x)\int_\Omega \langle a_1(t)\sum a_i^*(t)\Phi_i^*(x')\rangle \Phi_n(x')dx' \\
&- \langle \sum a_i(t)\Phi_i(x)a_1^*(t)\rangle \int_\Omega \Phi_1(x')\Phi_n(x')dx' \\
&+ \Phi_1(x)\langle a_1(t)a_1^*(t)\rangle \int_\Omega \Phi_1^*(x')\Phi_n(x')dx' = \lambda_n\Phi_n(x).
\end{aligned}$$

Noting that a property of the POD is $< a_i a_j >= \lambda_i \delta_{i,j}$ where $\delta_{i,j}$ is the Kronecker delta, for POD mode 1, Φ_1, this can be further simplified to

$$\begin{aligned}
&\int_\Omega R(x,x')\Phi_1(x')dx' \\
&- \Phi_1(x)\lambda_1 \\
&- \Phi_1(x)\lambda_1 \\
&+ \Phi_1(x)\lambda_1 \\
&= \int_\Omega R(x,x')\Phi_1(x')dx' - \Phi_1(x)\lambda_1 = (0)\Phi_1(x)
\end{aligned}$$

So the new snapshots have zero mean energy in the first POD mode. For the remaining modes, $\Phi_n(x)$ $n \neq 1$, the same procedure would be

$$\begin{aligned}
&\int_\Omega R(x,x')\Phi_n(x')dx' \\
&- \Phi_1(x) \int_\Omega \langle a_1(t) \sum a_i^*(t)\Phi_i^*(x')\rangle \Phi_n(x')dx' \\
&- \langle \sum a_i(t)\Phi_i(x)a_1^*(t)\rangle \int_\Omega \Phi_1(x')\Phi_n(x')dx' \\
&+ \Phi_1(x)\langle a_1(t)a_1^*(t)\rangle \int_\Omega \Phi_1^*(x')\Phi_n(x')dx' = \lambda_n\Phi_n(x).
\end{aligned}$$

This becomes

$$\begin{aligned}
&\int_\Omega R(x,x')\Phi_n(x')dx' \\
&- \Phi_1(x)(0) \\
&- 0 \\
&+ 0 \\
&= \int_\Omega R(x,x')\Phi_n(x')dx' = \lambda_n\Phi_n(x)
\end{aligned}$$

which shows that the form and eigenvalues of the remaining modes are unchanged. Thus, this procedure, which we call “deflation” can be used sequentially to determine the entire sequence of POD modes. The Lapack routine, DGEESVD, can be used to find the dominant eigenvalue and eigenvector pair rather than the entire spectrum, which allows step 1 in the procedure to be performed efficiently.

2.4.3 Accuracy

In this section the POD modes of Burgers' equation are built from FEM data using both the direct and snapshot method. The goal is to assess the effect of round-off errors on both the predicted eigenvalue spectrum and the mode shapes as well as to compare the different methods for calculating the eigenvalue spectrums and modes. When using the snapshot method, not all of the snapshots were used to create matrices (Eq. (2.6) and Eq. (2.9)) because the number of time steps in the simulations was much larger than the number of grid points. This inherently will make the snapshot results different than the direct method results. If the snapshots used are linearly independent and the number used, N_s, is larger than the number of grid points in the mesh, N_e, then any eigenvalues beyond N_e are guaranteed to be zero. This is because one can reproduce any solution on the mesh with N_e modes. Results are presented for N_e=100 and 400. For these cases, N_s was taken as 100 and 400 respectively where the snapshots were uniformly sampled from the full set of snapshots. The effect of the number of snapshots used will be examined more thoroughly in a subsequent section.

The eigenvalue spectrum of the snapshot method and the direct method are depicted in Fig. 2.3 for simulations of the initial condition $1 + \exp(\sin(4\pi x))$. Fig. 2.3a and Fig. 2.3b show results obtained from the simulations performed with N_e = 100 and N_e=400 respectively. The initial condition $1 + \exp(\sin(4\pi x))$ is interesting because two complete periods are contained within the domain. Because of this, all eigenvalues after the $(N_e/2)^{th}$ eigenvalue should be identically zero. By examining this problem, one can easily identify effects of round-off error on the eigenvalue spectrum. For Fig. 2.3a, all eigenvalues after 50 should be zero. For the direct method without deflation, one can see a drop in the eigenvalue from 10^{-10} to just below 10^{-14}. For the direct method with deflation the drop is larger, going below 10^{-17}. For the direct method without deflation, the eigenvalues beyond this point do not decay much further and the eigenvalue of mode 75 actually

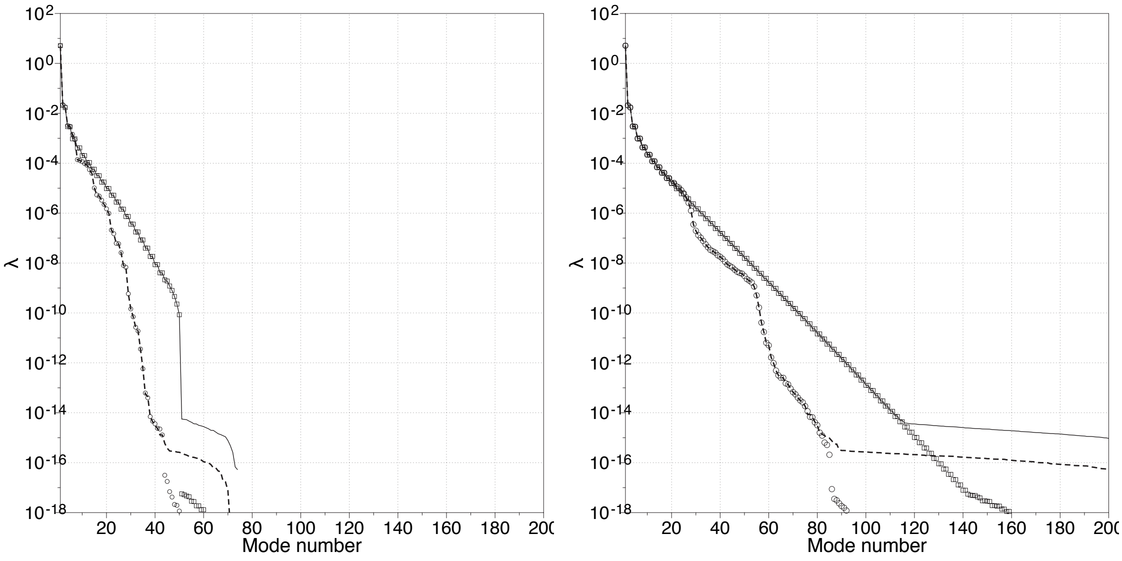

(a) (b)

Figure 2.3: Energy distribution of POD modes, Direct method without deflation (solid line), Snapshots method (dashed line), direct method with deflation (□) and snapshot method with deflation (○). Initial condition is $1 + \exp(\sin(4\pi x))$. a) N=100 b) N=400.

becomes negative and thus is not plotted. For the direct method with deflation, the eigenvalues continue to exponentially decay and reach a value of 10^{-24} for mode number 100. This was fairly typical of the behavior of these two methods. The methods agreed for the larger eigenvalues, but when the eigenvalues became small, the deflation method continued to give positive and diminishing eigenvalues while the direct method often gave non-physical negative eigenvalues.

This also occurred for $N_e = 400$ with the direct method. In this case, all eigenvalues beyond number 200 should be zero. However, because the eigenvalue spectrum already decayed 16 orders of magnitude at this point, the direct method was unable to predict this drop. For the direct method without deflation, the eigenvalue decay slowed significantly at mode number 118 and then stayed flat until mode number 251. At this point the eigenvalues went negative. For the direct method with deflation, the eigenvalues continued to decay.

Comparing the direct method eigenvalues in both figures, one can see that the eigenvalues agree reasonably well up to around the 50^{th} eigenvalue where the eigenvalues for the simulation with $N_e = 100$ suddenly dropped. The fact that the eigenvalue spectrum is reasonably independent of the numerical discretization indicates that the eigenvalues are a property of the solution and not an outcome of the numerical method. By comparing eigenvalue spectrums obtained with different meshes, one can discern which modes are physical (0-50 for $N_e = 100$) and which modes are strictly numerical artifacts $(50 - 100)$.

Comparing the snapshot method eigenvalues to those obtained by the direct method shows that the choice of $N_s = N_e$ is not sufficient to guarantee good agreement between the two methods. For $N_s = 100$ (Fig. 2.3a), the spectrums only agree to the 6^{th} mode or so. For $N_s = 400$ (Fig. 2.3b), the spectrums agree up to the 30^{th} mode. In most CFD calculations, the total number of snapshots is usually less than the number of grid points and one typically then uses the snapshot method. In the next section, we examine how many snapshots are necessary to give precise eigenvalues and eigenvectors. The difference between the snapshot method without deflation and the snapshot method with deflation is similar to what was seen for the direct method. Deflation always gives positive decaying eigenvalues where the snapshot method without deflation tends to plateau at machine precision and then give negative eigenvalues.

To bound the effect of round-off errors on the POD, error estimates for the numerical eigenvalue solvers can be used. For symmetric real matrices, two useful inequalities are defined in references [20] and [21]. Let two eigenproblems be defined as $AS_A = S_A\alpha$, $BS_B = S_B\beta$ and let the sequence of eigenvalues α_j and β_j be ordered by their (real) value. Define γ as the maximum difference of the eigenvalues,

$$\gamma \equiv \max_j |\alpha_j - \beta_j|,$$

then

$$\gamma \leq \|A - B\|.$$

This says that the magnitude of the change in an eigenvalue is not more than the magnitude of the difference between the two matrices. Suppose that A is the finite precision representation of Eq. (2.7) and B is the infinite precision representation. Define H as the finite precision error, $H = A - B$. Then the error in eigenvalues,

γ is bounded by

$$\gamma \leq \|A - B\| = \|H\| \tag{2.10}$$

if the relative precision is ϵ, we expect

$$\|H\| \leq n\epsilon\|A\| \tag{2.11}$$

where n is the rank of the matrix. For a real symmetric matrix A, the L_2 norm of A is is equal to its maximum absolute eigenvalue. Therefore, Eq. (2.11) shows that the maximum difference between the real and calculated eigenvalues is bounded by maximum absolute eigenvalue times machine precision times the rank of the matrix. For the results in Fig. 2.3a and Fig. 2.3b, the maximum eigenvalue is 5.135 and the calculations were done in double precision so ϵ is $O(10^{-16})$. This gives an error estimate for the eigenvalues of $5e-14$ when $N_s = 100$ and $2e-13$ when $N_s = 400$. This a reasonable estimate of the limits beyond which the actual values of the eigenvalues become predominately determined by round-off errors as shown by the fact the deflation and direct methods give very different answers for eigenvalues with a magnitude less than the error estimates.

The error estimates also predict the errors in direction of the eigenvectors [20, 21]. If $gap(i) = \min_{j\neq i} |\alpha_i - \beta_j|$ over all j's, meaning that α_i is separated by a $gap(i)$ from B's eigenvalues other than β_i, then

$$\sin(\angle(S_{Ai}, S_{Bi})) \leq \|A - B\|/gap(i) \tag{2.12}$$

Again using $\|A - B\| = \|H\| \leq n\epsilon\|A\|$, it follows that

$$\sin(\angle(S_{Ai}, S_{Bi})) \leq n\epsilon\|A\|/gap(i)$$

The gap for any of the eigenvalues is determined by the neighboring eigenvalues. For eigenvalue 1, for example the gap is $5.135 - 0.020$ so the error in direction of these eigenvectors is less than 1.004×10^{-14}. For the eigenvectors of the small eigenvalues, the gap is approaching $\epsilon\|A\|$ so these eigenvectors can point in entirely the wrong direction. This is not surprising in that there is basically no energy in these modes, so the definition of the eigenvectors becomes difficult. We note that the eigenvector solvers guarantee that all of the eigenvectors are orthonormal to machine precision in spite of the fact that the directions may be totally wrong.

The orthogonality of the eigenvectors of the discrete eigenvalue problem does not necessarily guarantee that the POD modes themselves are orthogonal. To demonstrate this fact, Fig. 2.4 shows the logarithm of the orthogonality ($log_{10}(|\int_\Omega \Phi_i \cdot \Phi_j dx|)$) of the modes generated by the four different methods for $N_s = 100$ and the initial condition $1 + \exp(\sin(4\pi x))$. (The eigenvalue spectrum for this case is shown in Fig. 2.3a). The ideal POD modes should have a 0 on the main diagonal and be around machine round-off (-16) everywhere else. The direct method without deflation (Fig. 2.4a) gave the best result with all modes being orthogonal up to machine precision. For the direct method with deflation (Fig. 2.4b) the eigenmodes up to mode 50 are orthogonal to 14 orders of precision, but orthogonality decreases significantly beyond 50 because there were two wavelengths within the domain. For the initial condition $1 + \sin(2\pi x)$, the orthogonality looked basically like the bottom left quadrant of the Fig. 2.4b. For the deflation method, the orthogonality decays because of the sequential nature in which the eigenmodes are found. Round off error accumulates during the process which gives the initial and final modes the worst orthogonality (the top and bottom left corners of the figure).

For the snapshot method without deflation (Fig. 2.4c), the orthogonality of the modes is poor for any mode beyond 30. This is the point where the eigenvalues start to decay towards machine precision as shown in Fig. 2.3a. For the higher resolution case (not shown), the behavior was similar with the decay starting at mode number 55 in agreement with Fig. 2.3b. When using the deflation method, the orthogonality was significantly improved and followed the same behavior as that of the direct method with deflation. The reason that the snapshot method without deflation is more sensitive to round-off errors than the direct method without deflation is that for the snapshot method, orthogonality of the discrete eigenvectors only guarantees orthogonality of the POD modes if the eigenvalue problem is solved precisely. For example, orthogonality is given by

$$\int_\Omega \Phi_i(x)\Phi_j(x)dx = \int_\Omega \Psi_{k,i}u(x,t_k)\Psi_{l,j}u(x,t_l)dx = \Psi_{k,i}\int u(x,t_k)u(x,t_l)dx\Psi_{l,j}$$

The last part of this expression is the left hand side of the snapshot eigenvalue problem, Eq. (2.8). If the eigenvalue problem is solved up to machine precision, then this can be replaced by the right hand side, and the orthogonality of the eigenvectors gives

$$= \Psi_{k,i}\lambda_j\Psi_{k,j} = \delta_{i,j}\lambda_j.$$

Thus, the snapshot method relies on the eigenvalue problem being solved precisely to obtain orthogonality of the POD modes. For the direct method, applying the discrete eigen solvers to Eq. (2.7) guarantees the orthogonality of the eigenvectors with respect to the mass matrix, ($V_i^T M V_j = \delta_{i,j}$) to machine precision. This is exactly the property needed to show orthogonality of the POD modes.

As a last check on the quality of the modes, we investigate their ability to reproduce the detailed solutions. In this work, we follow the methodology of Rathinam and Petzold [22] to evaluate error. The error between the detailed simulation and the projection onto the POD subspace is called the out of plane error, $e_o(t)$. This error is a consequence of the truncation of the POD modes. The instantaneous out of plane error, $\|e_o(t)\|$, is defined as the L_2 norm of the error caused by the POD subspace approximation, Eq. (2.4). This error is defined as

$$\begin{aligned} \|e_o(t)\|^2 &= \|u(x,t) - \sum\nolimits_{j=1}^{M}(u(x,t),\Phi_j(x))\Phi_j(x)\|^2 \\ &= \int_\Omega \Big(u(x,t) - \sum\nolimits_{j=1}^{M}(u(x,t),\Phi_j(x))\Phi_j(x)\Big)^2 dx. \end{aligned} \tag{2.13}$$

Fig. 2.5 shows the out of plane error for the initial condition, $\|e_o(0)\|$, for $N_e = 100$ (The orthogonality of the POD modes for this case is shown in Fig. 2.4.) There is a significant disagreement between the snapshot and the direct method because only 100 snapshots were used for the snapshot method. The issue of the effect of number of snapshots will be revisited in the next section. The methods with

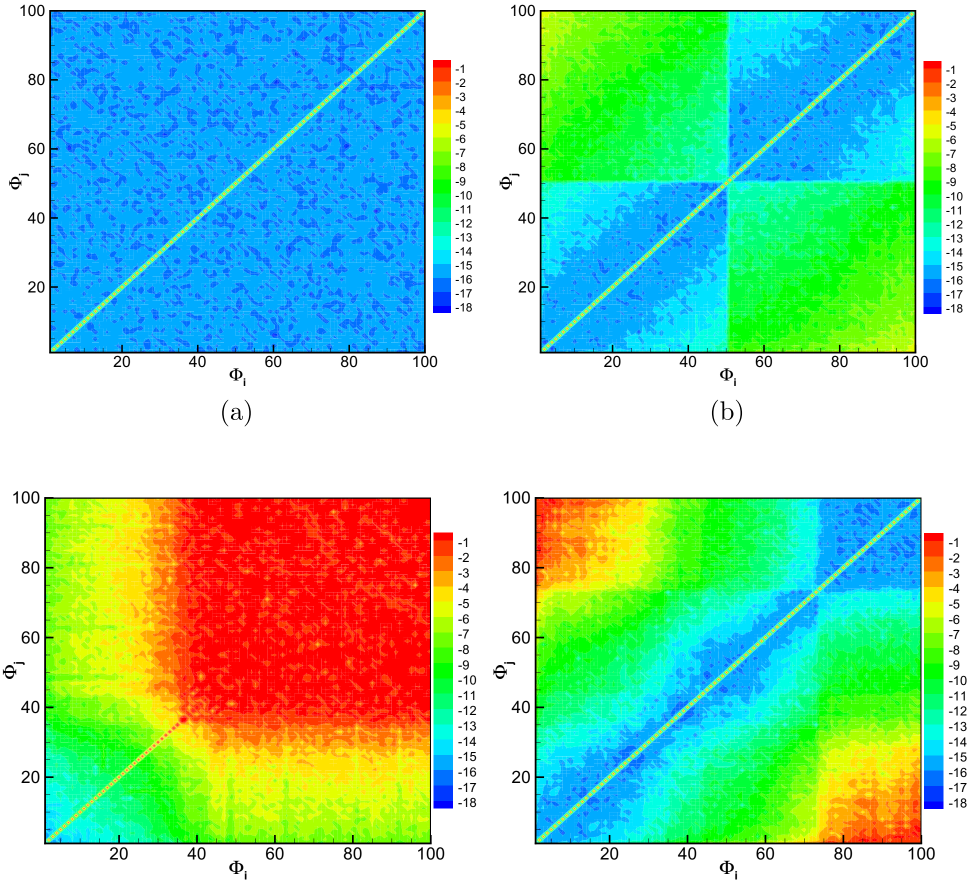

(a) (b)

(c) (d)

Figure 2.4: Orthogonality of POD modes for initial condition $1+\exp(\sin(4\pi x))$, (a) Direct method without deflation, (b) Direct method with deflation, (c) Snapshot method using 100 snapshots, without deflation, (d) Snapshot method using 100 snapshots, with deflation.

and without deflation agree well up to about 40 modes at which point the error using the deflation method increases as modes are added. This increase is due to the nonorthogonality of the modes. As one can see in Fig. 2.3a, when using the deflation method, the highest index modes are not orthogonal to the low index modes. As the solution contains a large amount of energy in the low index modes, this energy gets incorrectly captured by the high index modes as well causing the increasing error. This is especially true of the snapshot method, and one can see the resulting increase in error in Fig. 2.5.

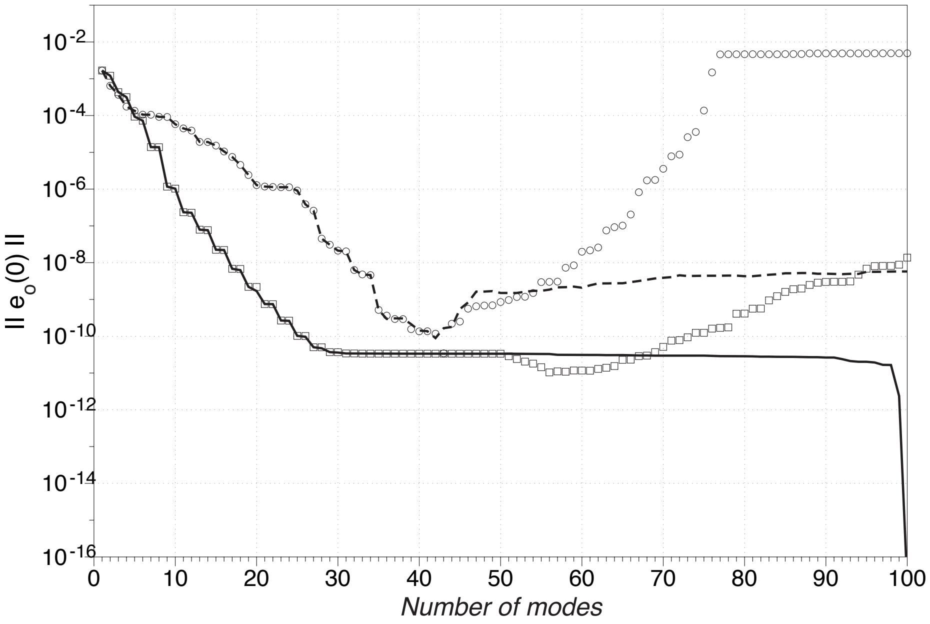

Figure 2.5: Out of plane error of the initial condition, $\|e_o(0)\|$. Direct method without deflation (—), snapshot method without deflation (– –), direct method with deflation (□), snapshot method with deflation (○).

To be sure that these errors are caused by the nonorthogonality of the modes, we can reconstruction the initial condition using deflated POD coefficients, meaning

$$a_i = \int \left(\Phi_i(x), (u(x) - \sum_{j=1}^{i-1} a_j \Phi_j) \right) dx. \tag{2.14}$$

This eliminates the possibility that energy in the low index modes gets captured by the high index modes. The results are depicted in Fig. 2.6. The results using deflated coefficients deviate from the previous results at about 40 modes, but in this case the reconstruction using the deflated coefficients gives improved results relative to even the direct method. This demonstrates that the reason for the increasing error shown in Fig. 2.5 is POD mode nonorthogonality.

We now investigate the effect of the number of snapshots used to generate the POD modes. In most applications of the POD, the snapshot method is used because one can choose the number of snapshots used and thus control the size of the eigenvalue problem that needs to be solved. Numerical studies by Noack et al. [23] showed that the first N pairs of POD modes can be computed from

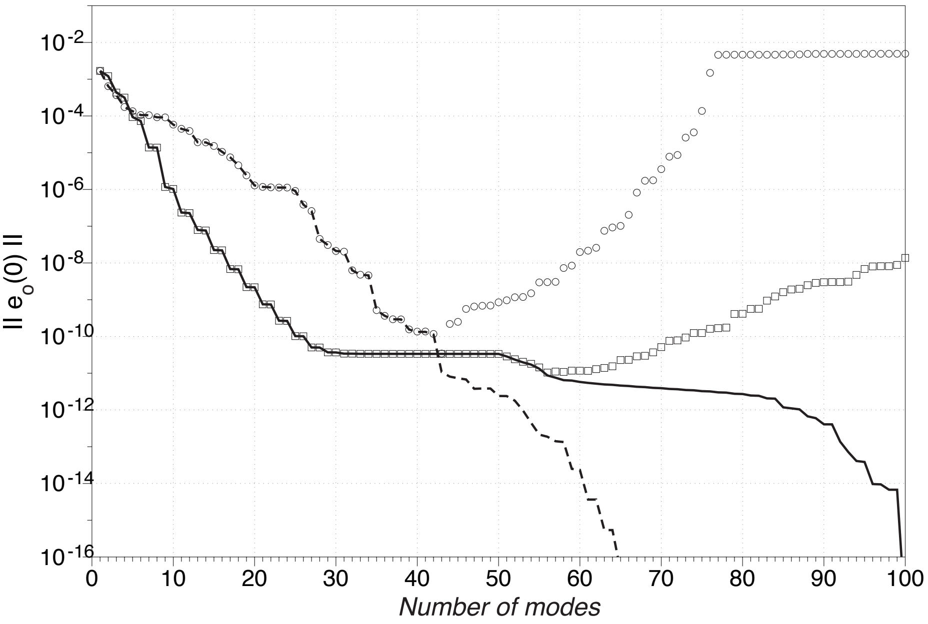

Figure 2.6: Out of plane error of initial condition $\|e_o(0)\|$. Direct method with deflated coefficients (—), snapshot method with deflated coefficients (– –), direct method with deflation (□), snapshot method with deflation (○).

only $2N$ snapshots for a shear layer flow. An increase to $4N$ or more snapshots did not have any significant effect on the resulting models. In this section, we try to quantify and predict the effect of the number of snapshots on the accuracy of the POD process. To this end, Fig. 2.7 shows the eigenvalue spectrums obtained when using different numbers of snapshots. The eigenvalues of the direct method are also shown in this figure for comparison. As expected, with an increase in the number of snapshots, the eigenvalues of the snapshot method converge to those of the direct method. For $N_s = 50, 100, 200, 400, 800$, the eigenvalues have a visible deviation from the direct method, respectively, for eigenvalues 5, 6, 15, 27, and 51 respectively. Thus, for this problem 8 times the number of grid points is enough to ensure good agreement throughout the energy containing part of the spectrum. Fig. 2.7b shows the out of plane error for the initial conditions for modes derived with differing numbers of snapshots. Here we see deviation from the direct method at 2, 5, 7, and 11, and 51 modes. Clearly, the number of snapshots needed depends on how accurately one wants to reproduce the solution.

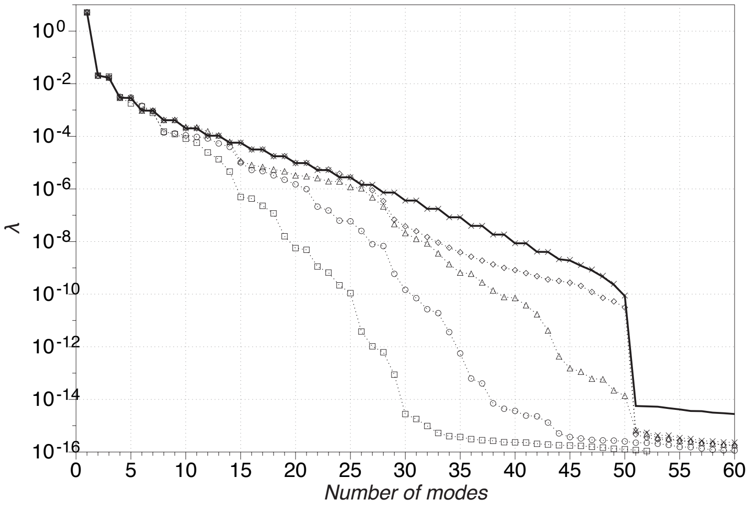

(a)

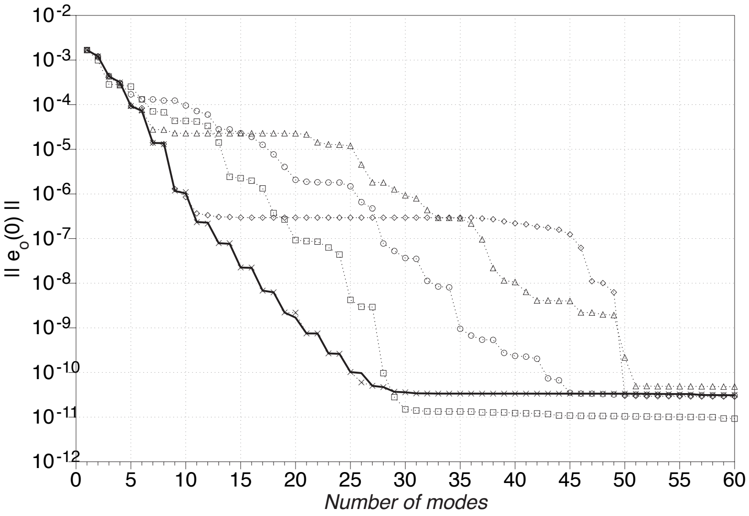

(b)

Figure 2.7: Eigenvalues, λ, and out of plane error of the initial condition, $e_o(0)$, for $1+\exp(\sin(4\pi x))$. Direct method without deflation (solid line), snapshot method without deflation constructed using 50 (boxes), 100 (circles), 200 (triangles), 400 (diamonds), and 800 (crosses) snapshots.

To more quantitatively analyze the effect of the number of snapshots on the accuracy of the modes, we begin by noting that if the time average needed for the direct method is evaluated with N_s snapshots, then the direct method and the snapshot method exactly agree (excluding finite precision errors). Thus, we can analyze the effect of N_s on the direct method which is easier mathematically. Let two direct method eigenproblems be $AS_A = S_A\alpha$, $BS_B = S_B\beta$. If A was constructed using a time average over all snapshots and B used fewer snapshots, then $A+H = B$. The error in eigenvalues can be bounded using the same formula as before, Eq. (2.10)

$$max|\alpha_j - \beta_j| \leq \|A - B\| = \|H\| \tag{2.15}$$

To determine H, we note that

$$\langle u(x,t)u(x',t)\rangle = \frac{1}{T}\sum_n u(x,t)u(x',t)dt \approx \frac{1}{T}\int_0^T u(x,t)u(x',t)dt$$

This corresponds to a midpoint method of integration which has the following error behavior

$$\int_0^T f(t)dt = \sum_{i=0}^{T/dt}\left(f\left(\frac{t_i + t_{i+1}}{2}\right) + \frac{f''(\bar{t}_i)dt^2}{24}\right)dt \ , \ t_{i+1} - t_i = dt \tag{2.16}$$

where $\bar{t}_i$ is some value in the time interval. Therefore, each step of the midpoint method therefore contributes an error of order $O(dt^3)$. Because T/dt intervals are used, the error of entire process is $O(dt^2)$. Substituting the error of Eq. (2.16) in Eq. (2.15) shows that the eigenvalues converge as $O(1/N_s^2)$. To confirm this, Fig. 2.8 shows the difference between eigenvalues 3, 7, and 11 of the direct method and the snapshot method with different number of snapshots. The thick dash-dotted line shows second-order convergence. Eigenvalues 3, 7, and 11 were chosen because they exhibit the range of behaviors observed. Fig. 2.8a shows the effect of grid resolution by comparing $N_e = 100$ and 400 at $\nu = 5 \times 10^{-3}$, and Fig. 2.8b shows the effect of viscosity by comparing $\nu = 5 \times 10^{-3}$ and 1×10^{-4} at $N_e = 400$. For all of these cases, there are some common trends. First, once enough snapshots are taken, all cases follow $O(dt^2)$ convergence. Thus, the above analysis is predictive of the convergence behavior. However, for the cases with $\nu = 5 \times 10^{-3}$, the error in the eigenvalues does not follow the predicted behavior until N_s is around 400 to 800. In addition, when this number of snapshots is reached, the error in the high index eigenvalues decreases rapidly. This is shown by the curves for eigenvalue 11 and is even more pronounced for the higher eigenvalues. These typically reach machine order accuracy when N_s is slightly greater than 800. This can also be seen in Fig. 2.7a by noting that when the number of snapshots increases from

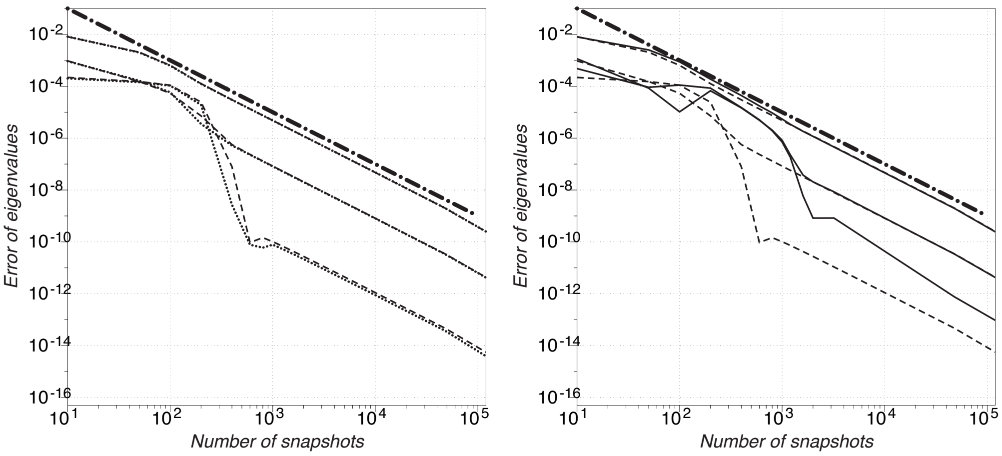

(a) $\nu = 10^{-3}$

(b) $N_e = 400$

Figure 2.8: Error in eigenvalues 3, 7, and 11 versus the number of snapshots. Left figure compares two grid resolutions, $N_e = 100$ (dotted line) and $N_e = 400$ (dashed line) at $\nu = 5 \times 10^{-3}$. Right figure compares two viscosities, $\nu = 5 \times 10^{-3}$ (dotted line) and $\nu = 1 \times 10^{-4}$ (solid line) at $N_e = 400$. In both figures, the thick dash-dotted line shows second order convergence.

400 to 800, one can no longer distinguish the snapshot eigenvalues from the direct eigenvalues. Comparing the cases $N_e = 100$ and $N_e = 400$ with $\nu = 5 \times 10^{-3}$, shows that this behavior is essentially grid independent.

To understand why this occurs, it is constructive to consider the time scales of the problem. As discussed previously, the width of the propagating front in this problem is on the order of ν/u where u is the propagation velocity of the front. Thus, there is an inherent time scale of ν/u^2. This is a conservative estimate of physical time scale. Another estimate can be obtained using the width of the propagating front divided by velocity. A criteria to determine when sufficient snapshots are used is that the snapshots intervals should be on the order of the smallest physical time scale,

$$\frac{\nu/u^2}{T/N_s} \simeq 1 \Rightarrow \frac{(5 \times 10^{-3})/4}{3/N_s} \simeq 1 \Rightarrow N_s = 2400,$$

or

$$\frac{l_{front}/u}{T/N_s} \simeq 1 \Rightarrow \frac{(6 \times 10^{-2})/2}{3/N_s} \simeq 1 \Rightarrow N_s = 100.$$

So, assuming the mesh resolves the width of the propagating front, then the drop off of the eigenvalue error should occur in the range of 100 to 2400 snapshots. The third case confirms this analysis in that when the smallest time scale decreases (by decreasing ν), the number of snapshots needed increases. The number of snapshot does not increase in direct proportion to the change in ν however because in this case the width of the propagating front can not be resolved on the mesh. Grid resolution does begin to play a role when the solution becomes under-resolved. Thus the critical feature for determining the number of snapshots is to resolve the smallest time scale of the phenomenon of interest. After that time scale is resolved, the eigenvalues and modes converge with second-order accuracy.

The last issue to examine is the out of plane error when using the modes generated by different methods. It can be shown that the temporal integral of $e_o(t)$ is equal to the summation of the truncated eigenvalues [22]

$$\sqrt{\sum_{j=M+1}^{N} \lambda_j} = \sqrt{\int_0^T \|e_o(\tau)\|^2 d\tau}. \tag{2.17}$$

This is true as long as the modes are free from round-off errors or from errors due to using a reduced number of snapshots. These errors, however, can clearly invalidate this relation, for example in the case of the direct method where the eigenvalues become negative. To investigate this further, Fig. 2.9 shows the left and right hand side of equation Eq. (2.17) for two different POD computations, the direct method and the snapshot method with $N_s = 100$. Neither case used deflation. For both cases, the left hand side is shown with symbols and the right hand side with lines. If symbols for the summation of the eigenvalues are not shown, it is because the summation was negative. This occurred for the direct method beyond 49 snapshots and for the snapshot method with 100 snapshots beyond 43 snapshots. Using the direct method, the integrated out of plane error and the summation of the truncated eigenvalues agree reasonably well with the actual out of plane errors being slightly higher than that predicted by the sum of the truncated eigenvalues. The out-of-plane error is slightly higher than the sum of the truncated eigenvalues, most likely because of the negative contribution of the eigenvalues greater than 49. For the modes generated with $N_s = 100$, the

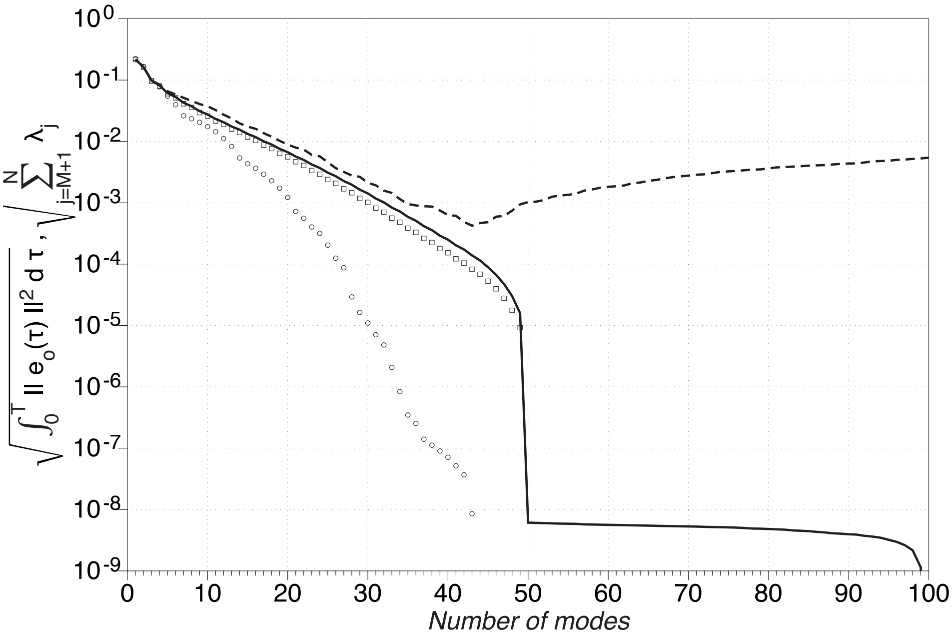

Figure 2.9: Integrated out of plane errors (lines) and the summation of the truncated eigenvalues (symbols) for the: direct method (solid line, boxes) and snapshot method with 100 snapshots (dashed line, circles).

sum of the truncated eigenvalues is much lower because of the errors discussed in the previous section. However, for approximations with less than 40 modes, the out-of-plane error of the modes is not significantly greater than the modes derived from the direct method. The insensitivity of the out-of-plane error to the data used to generate the modes has been discussed in [22]. Essentially, because the modes satisfy a maximum condition, the change in the out-of-plane error with infinitesimal perturbations to the eigenvector directions is zero. Thus, this gives a low sensitivity of the error to finite amplitude changes in the POD modes. If one is not concerned about the eigenvalue spectrum, one can use fewer snapshots and still obtain modes that represent the solution well. For the snapshot method, the error increases after 45 modes for the reasons given in the discussion on mode orthogonality.

To conclude the analysis of the errors affecting the POD mode generation process, the following observations are made:

- The number of samples for the snapshot method should be large enough to resolve the smallest time scales of the problem. Beyond this number of snapshots, the error in the higher modes rapidly decays and converges with second order in the number of snapshots.

- Round-off error significantly affects the higher index modes. If the snapshot method is used, these errors cause non-orthogonality of the modes, which leads to an increase in the projection error with number of modes.
- The error in eigenvalues can be reduced using the deflation method, but this increases the non-orthogonality errors. It may be possible to use a stabilized Gram-Schmidt algorithm or a Householder algorithm [24] to reduce the nonorthogonality, but this has not been investigated here.

2.5 ROM

Given a set of POD modes, a ROM can be generated by using the POD modes as test functions in a weak formulation of the governing equations. A Galerkin weak form is most often used [7, 8] in which the system of equations is givne as

$$\frac{d}{dt}\left(u,\Phi\right)+\left(\left(u\cdot\nabla\right)u,\Phi\right)-\nu\left(\nabla u,\nabla\Phi\right)=0\quad\forall\Phi$$

where u is expanded in a series of POD modes as shown in Eq. (2.4). If only a finite number of terms in the expansion are kept, this becomes a low-dimensional model. Keeping the first M modes, a system of ordinary differential equations of dimension M is derived,

$$\frac{\partial a_n}{\partial t}=f_n(a_1,...,a_M)\quad n\in[1,M].$$

This is the governing equations that determines the evolution of the weighting coefficients, a_n. Additional information may be found in [25].

As discussed in the introduction, a POD-ROM using a Galerkin weak formulation can diverge or drift to the wrong solution [5, 26–30] and a proposed solution to this problem is to add dissipation or stabilization to the ROMs [6, 31]. Because the streamwise-upwind-Petrov-Galerkin (SUPG) was used to stabilize the FEM simulations, we also investigate ROMs generated using a SUPG stabilized weak form as proposed by [9]. The form of the SUPG equation after simplification is

$$\frac{d}{dt}\left(u,\Phi+u\tau\frac{\partial\Phi}{\partial x}\right)+\left(\left(u\cdot\nabla\right)u,\Phi+u\tau\frac{\partial\Phi}{\partial x}\right)-\nu\left(\nabla u,\nabla\Phi\right)=0\quad\forall\Phi$$

The advantage of SUPG over other stabilization methods is that it is a consistent formulation in that if the POD modes can exactly represent the solution to the governing equation, then this solution will also satisfy the weak form. This is not true of artificial dissipation approaches that add additional stabilizing terms to the governing equation.

Another subtlety of the ROM process is that the specific form of the data used to generate the POD modes is important. For example, one could generate POD modes from either Fourier or FEM simulations. If the simulations are well resolved, then these modes should be very similar. However, as noted in the Numerical Implementation section, a SUPG weak form will have no effect for the modes constructed from the Fourier simulations. The implications of this will be seen in the subsequent results section.

2.5.1 Results

In this section, the impact of stabilization and the quality of the POD modes on the error of ROMs is investigated. To begin, the the error criteria are introduced. Many previous authors [6–8, 12, 32] used the error of the first few POD coefficients as an error criterion, whereas much of the significant error happens in the high index mode numbers. For example, Fig. 2.10 compares the FEM solution with a POD-ROM simulation of Burgers equation with 10 POD modes for the initial condition $u(x,0) = 1 + \exp(\sin(4\pi x))$ and $\nu = 0.005$ over $N_e = 100$ grid. It is obvious that the difference between the simulations has high wave number components. Therefore, the error of first few coefficients is not enough to assess the total error. We therefore continue to follow the methodology of Rathinam and

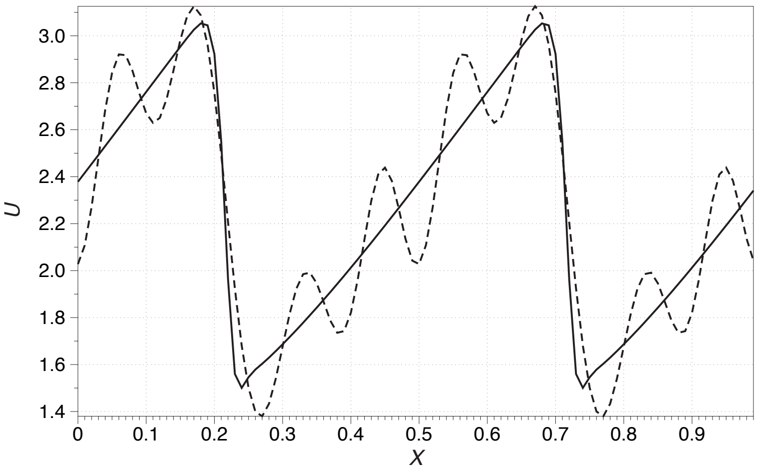

Figure 2.10: Comparison between detailed FEM (solid line) and 10 dimensional POD-ROM (dash line) simulation of Burgers equation for initial condition $1 + \exp(\sin(4\pi x))$.

Petzold [22] to evaluate error. The out of plane error, $e_o(t)$, was introduced as the error between u and its projection onto the POD subspace in section 2.4.3. The total error between the FEM and ROM simulation can be thus split into two orthogonal vectors: $e_t(t) = e_o(t) + e_i(t)$ where $e_i(t)$ is the “in plane error” during a ROM simulation in the POD subspace. Because the FEM results are known, the total error, $e_t(t)$, can be calculated easily and then the in-plane error can be deduced. Assessing the in-plane error is important because it indicates the quality of the ROM solution as compared to the best possible reproduction of the FEM given that space of POD modes. Said another way, the in-plane error is the error caused by the ROM and the out-of-plane error is the error caused by using a finite dimensional POD space.

To understand the effect of stabilization, two different viscosities are studied, $\nu = 0.005$ and $\nu = 0.0001$. With $N_e = 100$, which is the grid resolution used in all the following, these correspond to high and low grid-based Reynolds number simulations. The first case has a $Re_{\Delta x} = 4$ and the second of 200, however both cases are actually high Reynolds number in terms of the domain length (400 and 2000 respectively). The first case corresponds to a simulation where Galerkin FEM and SUPG FEM both perform well. In the second case, the front-thickness is not well-resolved on the mesh and a SUPG simulation gives improved FEM results over a Galerkin formulation, but neither accurately resolves the propagating front. This case was investigated mainly to obtain further insight into the effect of stabilization; there is little reason to make a ROM from under-resolved simulations. For both the FEM and POD-ROM simulations, two cases, one with (SUPG) and without stabilization (Galerkin), have been performed. Unless otherwise noted, the direct method without deflation has been employed to derive the POD modes.

We begin by examining the convergence of the ROM to the FEM simulations. Fig. 2.11 shows the convergence of the temporal maximum of the L_2 error for the low Reynolds case i.e. the maximum in time of $e(t)$. As a point of comparison, the convergence of an N_F mode Fourier simulation to a 512 mode Fourier simulation is shown as well. The convergence rate of the POD is faster than the Fourier method. This is expected as the POD modes are chosen to optimally represent the solution. Up to around 30 modes, there is little difference between the Galerkin and SUPG ROMs. This was somewhat unexpected because even though the low index mode shapes are nearly identical for the two approaches, the weighted integral forms used in the ROM are not. The two weighted integral forms are essentially

$$\int \phi \mathcal{L}(u)\ dx$$

for Galerkin and

$$\int \left(\phi + u\tau \frac{d\phi}{dx} \right) \mathcal{L}(u)\ dx$$

for SUPG. When only a low number of modes is used, $\mathcal{L}(u)$ is not zero so the two different weightings of the residual should give significantly different results. The fact that the results are nearly identical indicates that the SUPG weighting term is not having a significant effect. One could speculate various reasons for this, maybe the SUPG term is small because the grid Reynolds number is only 4 or maybe the modes are Fourier-like such that the SUPG terms is irrelevant.

The total error, $e_t(T)$, and the out-of-plane error, $e_o(T)$, are depicted in Fig. 2.12 for the low Reynolds case. We again see that the two approaches perform similarly. Up to 30 modes, the out-of plane error for both the Galerkin and SUPG modes are

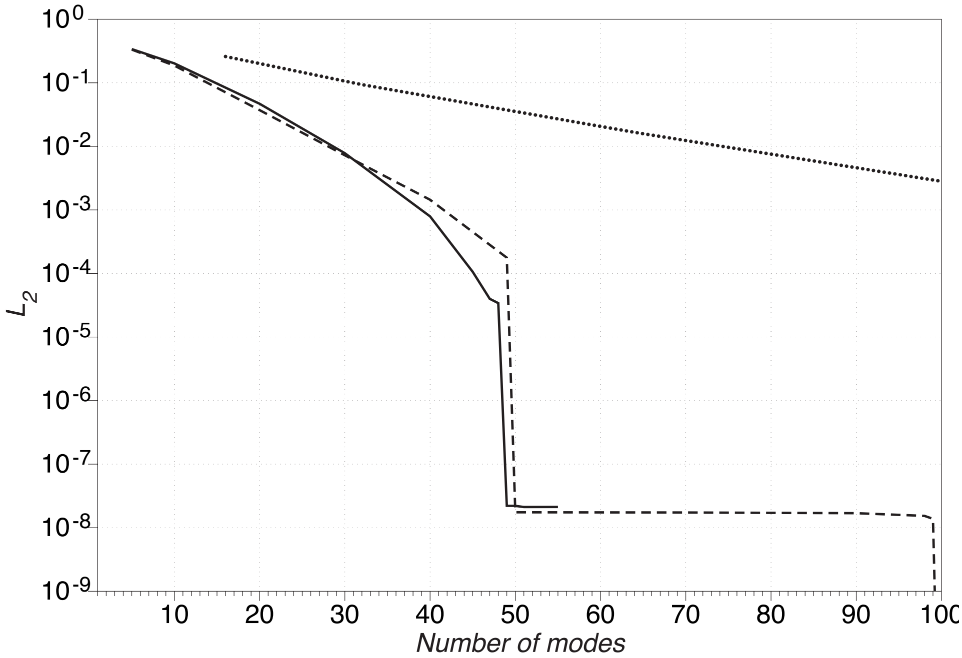

Figure 2.11: Maximum L_2 error of Fourier method (dotted line), POD-ROM simulation straight Galerkin (solid line) and POD-ROM simulation using SUPG stabilization (dashed line).

basically indistinguishable confirming that the low-index mode shapes are nearly the same. For both the SUPG and Galerkin approach, when a small number of modes is used, the total error is higher than the out-of-plane error which indicates that there is a significant in-plane error. As the number of modes increases, the relative magnitude of the in-plane error decreases and the magnitude of the out-of-plane and total errors are almost the same. In [22], it was proven that the in-plane error, $e_i(T)$, is bounded by an integral of the out-of-plane error, $e_o(t)$ as follows

$$\|e_i(T)\| < \gamma_M \sqrt{\int_0^T \|e_o(\tau)\|^2 d\tau} = \gamma_M \sqrt{\sum\nolimits_{j=M+1}^{N} \lambda_j}. \tag{2.18}$$

where γ_M depends on the ROM solution evolution operator. The total error satisfies a similar bound with a different definition of γ_M. As the solution evolution operator changes with the number of modes included in the ROM, γ_M changes with the number of modes included in the model. This fact was not investigated in detail in [22] and the convergence of the in-plane error was mostly assumed to reduce to zero in proportion to the out-of-plane error. Fig. 2.12 shows that in fact the in-plane error goes to zero faster than the out-of plane error; for low

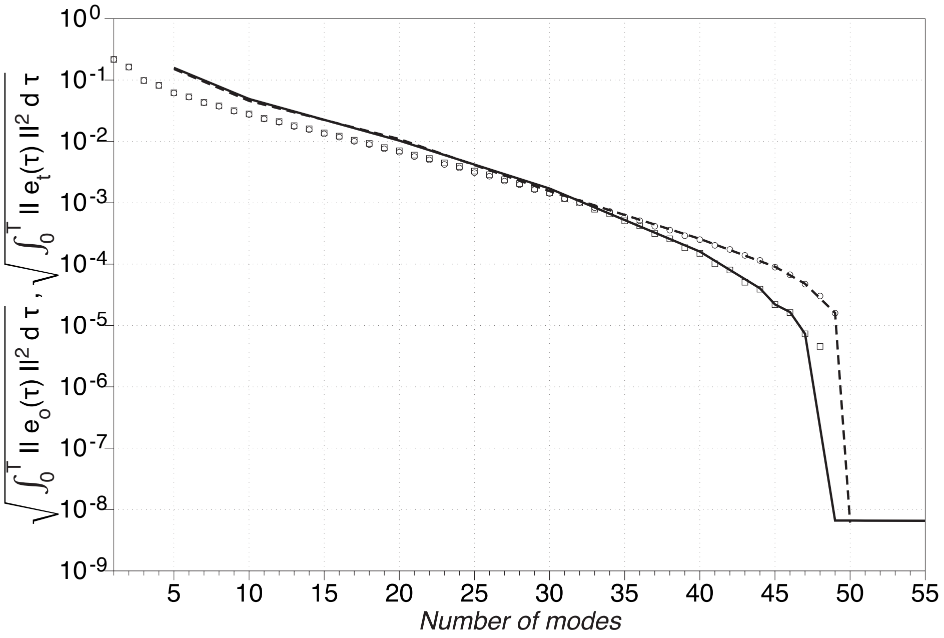

Figure 2.12: Total error, $e_t(t)$, and out-of-plane error, $e_o(t)$, for Galerkin (solid line, boxes) and SUPG stabilized (dashed line,circles) POD-ROMs for low grid based Reynolds number.

dimensional models ($M < 30$) the in-plane error makes an observable contribution to the total error, but for higher dimensional models, the error is almost entirely due to the out-of-plane component. This indicates that γ_M is actually decreasing to zero as the number of modes in the model increases.

For the high Reynolds number case, there is a more significant difference between the Galerkin and the SUPG results. As the steep propagating front in this case is under-resolved, there is significant oscillations in both the Galerkin and SUPG solutions although more so in the Galerkin simulations. This leads to a slower convergence rate in the out-of-plane error as shown by the symbols in Fig. 2.13. The total error for both cases follows the out-of-plane error; however in this case, the in-plane error makes a more significant contribution to the total error. For the SUPG case, we again see the in-plane error contribution decreasing at about 30 to 35 modes (where the total error and the out-of plane errors start to coincide). In the Galerkin case, the in-plane error remains significant up to 50 modes. It should be remembered that this is the comparison between the detailed simulations and the reduced order model so the fact that the error becomes small at 50 modes is

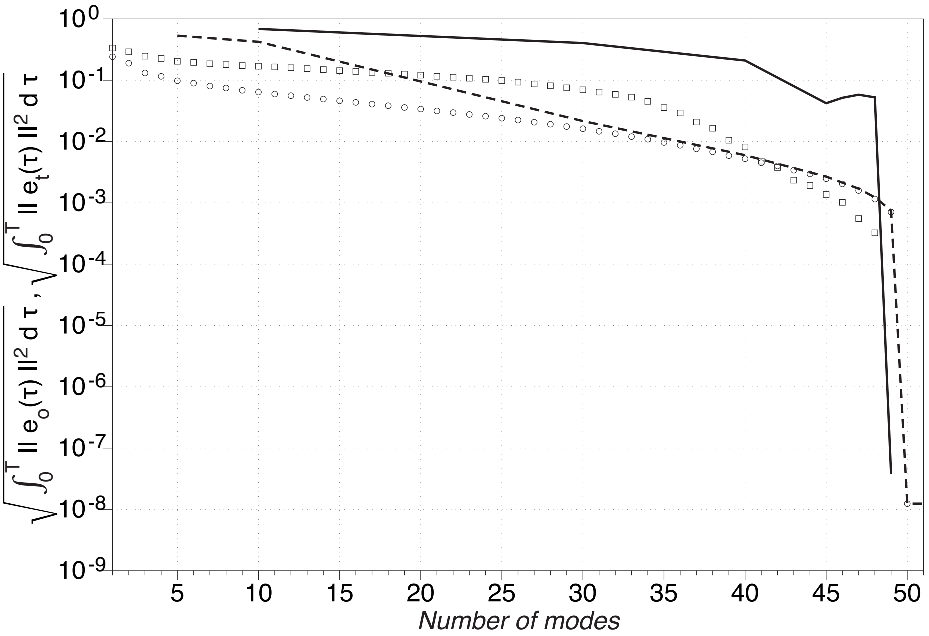

Figure 2.13: Total error, $e_t(t)$, and out-of-plane error, $e_o(t)$, for Galerkin (solid line, boxes) and SUPG stabilized (dashed line,circles) POD-ROMs for high grid based Reynolds number.

only an indication that the ROM reproduces the detailed simulation, not that the simulations are physically accurate.

Lastly, we examine the effect of the quality of the eigenmodes on the total error, $e_t(t)$. Two different sets of eigenmodes are used:

- **Case A:** The POD modes driven from direct method without deflation.
- **Case B:** The POD modes derived from snapshot method using 100 snapshots without deflation.

Case A corresponds to modes with the most orthogonal modes and lowest out-of-plane error as shown in Fig. 2.4 and Fig. 2.9. Case B corresponds to modes with less orthogonality and higher out-of-plane error. All simulations have been done using SUPG stabilization applied to the low Reynolds case. The total error, $e_t(t)$, and out of plane error, $e_o(t)$ are depicted in Fig. 2.14. Comparing the two cases, one sees that the penalty for using a reduced number of snapshots (100 versus 240,000) is not great; the out-of-plane error and total error of Case B are only

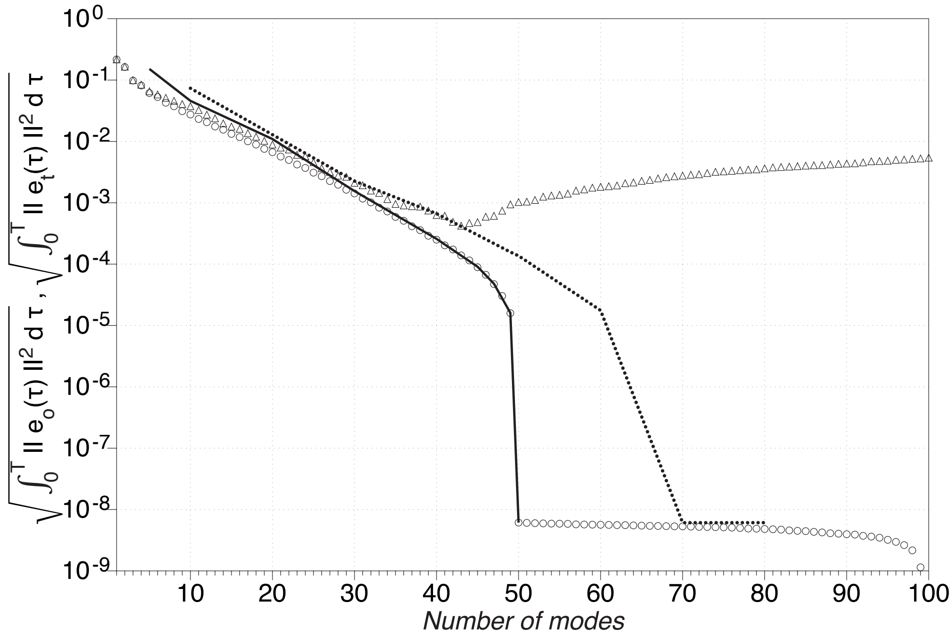

Figure 2.14: Total error (curves) and out-of-plane error (symbols) of SUPG stabilized POD-ROM simulations: direct method (solid line, circles) and snapshot method with 100 snapshots (dotted line, triangles).

slightly greater than the results obtained with Case A. The main determiner of the accuracy of the models is the number of modes included.

The one unexpected behavior in Fig. 2.14 is that for case B, the total error of the ROM, $e_t(t)$, is less than the out-of-plane error, $e_o(t)$ when the number of modes used is greater than 43. As mentioned previously, the out-plane error is the difference between the FEM simulation and its projection onto the POD modes. Because of this, the out-plane error becomes larger as the non-orthogonality of the modes increases. A large nonorthogonality of the POD modes for this case was shown earlier in Fig. 2.4c. The total error is the difference between the FEM simulation and the reduced order simulation. It is only affected by nonorthogonality of the POD modes at the very first time step when the initial condition is construct by projection. After this, the ROM solution dos not require orthogonality. The out-plane-error is only required to be less than the total error when considering modes that have no orthogonality errors.

2.6 Conclusions

This chapter examined the accuracy of the reduced order model based on the proper orthogonal decomposition (POS-ROM). The effect of various errors on the eigenvalue spectra and the quality of the POD modes are first assessed. The second part of Chapter 2 was focused on the accuracy of the reduced order models. The cases of high- and low-grid-based-Reynolds-number studies for Burgers equation were examined. The cases with and without stabilization are treated. The streamwise upwind-Petrov-Galerkin (SUPG) that was used to stabilize the FEM simulations, was also used to stabilize the ROMs. Based on the presented results the following conclusions are drawn:

- It was found that the lapack solution of the eigenvalue problem often gives negative values when the eigenvalues approach the machine precision, while the deflation method always gives positive decaying eigenvalues. Error bounds were given that show that the errors depend on the maximum POD eigenvalue, machine precision, and the rank of the matrix. Percent error bound showed that the eigenvalues less than the magnitude of machine precision times maximum absolute eigenvalue are very different for the deflation and direct methods.

- The orthogonality of the POD modes for different calculation methods was compared. The direct method without deflation is the only method that guarantees the orthogonality up to machine precision. For the snapshot method without deflation the orthogonality of the modes is poor for any mode beyond the point where the eigenvalues approach the machine precision. The orthogonality of the snapshot method can be improved using the deflation method but not to the machine precision.

- For the snapshot method, the number of snapshots required to obtain an accurate eigenvalue spectrum was determined by the smallest time scale of the process. When this time scale is resolved, the errors in the eigenvalues and modes drop rapidly then converge toward the exact modes with second-order accuracy.

- For the high Reynolds number flow case, the numerical results with stabilization were more accurate. Without stabilization the in-plane error of the ROM was high even when the number of POD modes used in the model was increased. However, when the detailed simulations used to derive the ROM were well-resolved (the low-Re case), the accuracy of both models was comparable.

- Rathinam and Petzold [22] showed that the in-plane error was bounded by the out-of-plane error times a modeling constant. Our results showed that the modeling constant goes to zero as the number of modes increases. So not only is the in-plane error bounded by the out-plane error, but the in-plane error goes to zero faster than the out-of plane error as the number of POD modes increases.

- Comparison of ROMs derived using the high and low quality POD modes showed that the ROM was fairly insensitive to the quality of POD modes. The accuracy of the ROMs was much more sensitive to the number of POD modes used in the model. Percent increase in the number of modes (regardless of orthogonality quality) improved the accuracy of ROM. However, increasing the number of POD modes wass more effective if the modes were more orthogonal.

Chapter 3

Proper Orthogonal Decomposition Based Reduced Order Models for Low and High Reynolds Flows

3.1 Introduction

Despite the remarkable improvements in computer speed and memory, accurate real time solution of the Navier-Stokes (NS) equations is still beyond the limits of current computational capabilities. However, in certain applications, such as active flow control, rapid flow prediction is critical. To overcome this problem, one possibility is to use a reduced order model (ROM) of the flow. A review of different ROMs was provided by Antoulas [1]. In this work, proper orthogonal decomposition (POD)-based reduced order modeling is studied as this approach has been used extensively in fluid flow applications as discussed below.

POD was introduced independently by Karhunen [3] and Loeve [4] for studying the stochastic characteristics of complex non-linear dynamical systems. In fluid mechanics, the POD was first introduced by [2, 33] for studying the coherent structures of a turbulent flow field. Due to its ability to capture dominant flow structures, the use of the POD for analyzing turbulent flows has attracted attention [5, 26, 28, 34, 35]. The POD provides an optimal orthogonal basis that makes it possible to reconstruct a stochastic process using a linear combination of a small number of spatial modes. These modes are normally obtained as eigenfunctions of the two-point correlation function of the random process. Projecting the governing equation (in this case the Navier-Stokes equation) onto a finite number of the POD basis functions results in a system of coupled ordinary differential equations (ODEs). The solution of which provides an accurate ROM of the flow field.

Although in principal POD-based ROMs can efficiently represent complex stochastic systems, there are a number of points that need to be thought through. First, POD-ROMs often use only a small number of modes to represent the flow. While a few modes are often sufficient to reconstruct the large-scale energy containing features of the flow, the modes that are associated with the small-scale fluctuations are truncated. Because dissipation occurs at small scales, which are typically associated with the low-energy POD modes, the POD-ROM dynamical system may not provide sufficient dissipation. It is crucial that the effect of small-scale dissipation is taken into account to make the simulations stable and robust. In this regards, different approaches have been suggested.

The first attempt for stabilizing POD-ROMs was with the use of eddy viscosity models introduced by Aubry et al. [5]. In this approach an artificial viscosity is added to the governing equation, which is referred to as the Heisenberg model [36]. Along this line, Ukeiley et al. [37] suggested an eddy viscosity model based on the characteristic scales of the first truncated POD modes. Podvin [11] improved the eddy viscosity closure models by accounting for the intermodal energy transfer. His model did not reproduce the detailed physics of the flow, however, it captured the essential aspects of the mechanism for the generation of turbulence.

Another class of eddy viscosity closure models considers the energy balance of the POD-ROM [38, 39]. It is generally recognized that the eddy-viscosity type models for POD depend on many parameters including the power spectrum shape, cutoff

POD mode, and energy transfer to the cutoff POD mode. In some respect this is similar to modeling the truncated modes in spectral closures [40, 41]. Rempfer and Fasel [28] and Rempfer [27] suggested that the dissipation term should be replaced by modal viscosities that affect each POD mode differently. Based on this idea, Tadmore [42] developed the Spectral Vanishing Viscosity (SVV) approach, which introduces an artificial dissipation that only affects the small-scales. This method is suitable where global energetically-ordered modes are involved (hierarchical discretizations) e.g. spectral Fourier methods. In this spirit, [6] introduced SVV into POD-ROM simulations and were able to obtain accurate large-scale results although inaccuracies in the small-scale modes were observed.

Ullmann and Lang [13] briefly mentioned the possibility of taking an LES subgrid-scale model into account in the reduced order model. The truncation of modes to build a POD-ROM is similar to filtration of small-scales in a large-scale modeling point of view. They employed the Smagorinsky subgrid-scale model as a stabilization technique for the POD-ROM model with the standard constant. The results of the model did not exactly match the original LES. However, the POD-ROM reproduced the energy spectrum of the flow. Wang et al. [10] used the same idea but instead of using the grid size in the Smagorinsky subgrid-scale model, they used a constant coefficient associated with the unresolved POD modes. By adjusting the model constants, they were able to obtain accurate results for the large-scale POD modes for 100 vortex shedding cycles.

Another approach to stabilization is to calibrate the evolution of the POD-ROM coefficients using the correct coefficients derived from the projection of the detailed simulations onto the POD modes [7, 8, 12, 43]. Using the known correct coefficients, all the ROM coefficients are adjusted using various error criteria such as least-squares minimization [7, 12, 44] or solving an optimization problem [45]. Although this approach can predict a specific DNS, it is unclear whether it will be accurate for varying flow conditions and inputs. In a related approach, Akhtar et al. [30] used a shooting method for analyzing laminar flows over a cylinder. This method adjusts the initial conditions of each cycle of to stabilize the solution. The effectiveness of this method for high Reynolds number non-periodic fluid flow still needs to be tested.

Most of the available approaches suffer from lack of generality for various flow conditions and/or lack of accuracy for the small-scale POD modes especially for long-time simulations. In other words, even with stabilization, calibration and closure, most of the available approaches are valid only for the time window of the detailed simulation from which the POD modes were extracted and/or for short term extrapolation. In addition, there are a number of parameters that need to be adjusted or optimized in the closure models for different applications.

The second major issue with current POD-ROMs is that most numerical studies have been done for low Reynolds number (Re) flows, with Re at most on the order of 100 to 1000. [6, 8, 9, 12, 30, 43, 46–49]. However, most practical turbulent flow problems are at higher Reynolds numbers. POD-ROMs may encounter issues in high Reynolds number flows [50, 51]. In particular, high Reynolds number flows involve more fluctuating energy and a wider spectrum. Therefore, there is a larger amount of energy transfer to the small-scales and a wider bandwidth of energetic POD modes. To reach the same accuracy of flow reconstruction at high Re, more POD modes are needed and truncation effects are more significant.

Most of the POD-ROMs for high Reynolds number flows have been performed using experimental databases [52–57], however there are few works in which numerical databases were used for more complicated flows. Couplet et al. [7] considered the turbulent flow past a backward-facing step at Reynolds number of 7432 based on the step height. The corresponding calibrated POD-ROM was shown to lead to reasonable results. Ulmann and Lang [13] examined the flow over a 3D cylinder at Re=3900. They used the database generated by LES and applied the subgrid-scale model of the original simulation to stabilize the corresponding POD reduced order model. Although, the lift and drag coefficients of the reduced model did not exactly represent the original LES, the energy spectrum was reproduced well. Sinha et al. [58] used an existing direct numerical simulation database of an unforced Mach 0.9 axisymmetric jet with Reynolds number of 3600 (based on the jet diameter). 30 POD modes were considered in straight Galerkin projection without any stabilization. It was shown that the large-scale evolution of the flow was well captured but not the small scales. They concluded that the POD-ROM may be adequate for the purpose of simulating the actuated flow. All in all, the natural question to ask is if a stabilization approach works well for low Reynolds number flow, how well will it work at high Reynolds number?

The main purpose of this paper is to assess the accuracy of different stabilization approaches for long term POD-ROM simulations for low and high Reynolds number flows. The test case of low Reynolds number flow at $Re = 1000$ over an airfoil is first studied. The streamline-upwind-Petrov-Galerkin (SUPG) method and the spectral vanishing viscosity (SVV) method for stabilization are used and the results are compared those of POD-ROM without stabilization (straight Galerkin). Similar comparisons are then performed for the high Reynolds number flows. This is done by analyzing 2D turbulent flow over an airfoil at a Reynolds number of 100,000 and generating POD-ROM models.

3.2 Detailed Solutions

In this section, details of the method used for simulating the unsteady, 2D, incompressible, viscous, flow around a NACA0015 airfoil are described.

3.2.1 Problem Description

The geometry of the problem, as well as, the computational mesh (which is discussed subsequently)are shown in Fig. 3.1.

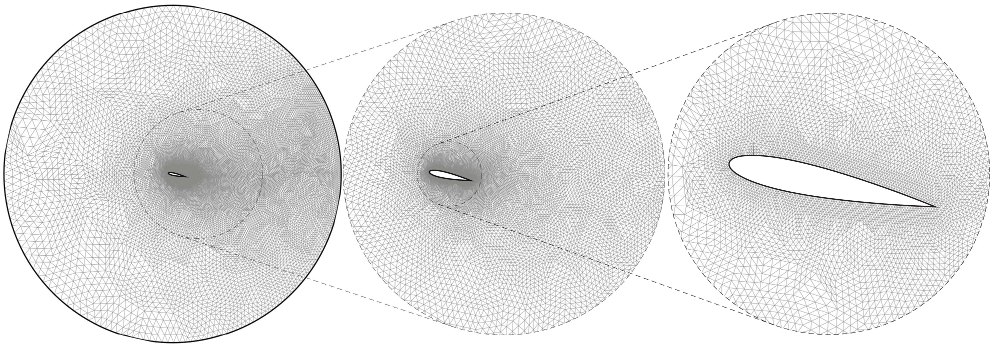

Figure 3.1: *hp*-Finite element mesh for low Reynolds case study, Re=1000 (chord length of the NACA0015 airfoil=1; Radius of domain=10.)

A circular domain, Ω, surrounds a NACA0015 airfoil which has its quarter-cord location centered at $(0, 0)$ and has an angle of attack (the angle between the chord line of the airfoil and the free stream velocity vector) of 12°. The radius of the computational domain is 10 times the chord length. The boundary of the domain, Γ, is divided into a left and a right arc. On the left side an inflow condition is enforced where the velocity is set to the free-stream velocity, u_∞. On the right side, an outflow condition is enforced where the total stress is set to zero. On the airfoil surface a no-slip boundary conditions is enforced. The problem is made non-dimensional using the chord length, the fluid density, and the free-stream velocity.

3.2.2 Governing Equations

The equations which govern the unsteady flow of an incompressible viscous fluid are the continuity and Navier-Stokes equations,

$$\frac{\partial \boldsymbol{w}}{\partial t} + \frac{\partial \mathbf{f}_x}{\partial x} + \frac{\partial \mathbf{f}_y}{\partial y} = \frac{\partial \boldsymbol{\tau}_x}{\partial x} + \frac{\partial \boldsymbol{\tau}_y}{\partial y}, \tag{3.1}$$

where $\boldsymbol{w}$ and the inviscid fluxes $\mathbf{f}_x$ and $\mathbf{f}_y$ are given by

$$\boldsymbol{w} = \begin{bmatrix} 0 \\ \rho u \\ \rho v \end{bmatrix}, \; \mathbf{f}_x = \begin{bmatrix} \rho u \\ \rho u^2 + p \\ \rho v u \end{bmatrix}, \; \mathbf{f}_y = \begin{bmatrix} \rho v \\ \rho u v \\ \rho v^2 + p \end{bmatrix}, \tag{3.2}$$

u and v are the x- and y-direction velocities, and ρ and p are the density and pressure. $\boldsymbol{\tau}_x$ and $\boldsymbol{\tau}_y$ are the viscous stresses,

$$\boldsymbol{\tau}_x = \mu \begin{bmatrix} 0 \\ 2\partial u/\partial x \\ \partial v/\partial x + \partial u/\partial y \end{bmatrix}, \; \boldsymbol{\tau}_y = \mu \begin{bmatrix} 0 \\ \partial v/\partial x + \partial u/\partial y \\ 2\partial v/\partial y \end{bmatrix}. \tag{3.3}$$

where μ is the dynamic viscosity of the fluid which is assumed to be constant. For convenience, we also introduce the total flux vectors in the x and y directions, $\mathbf{e}_x = \mathbf{f}_x - \boldsymbol{\tau}_x$ and $\mathbf{e}_y = \mathbf{f}_y - \boldsymbol{\tau}_y$.

3.2.3 Numerical Method

An *hp*-finite element method is employed for performing the numerical simulations. The streamwise-Upwind-Petrov-Galerkin (SUPG) variational approach [18] is used to discretize the governing equations on a finite element mesh consisting of triangular elements as shown in Fig. 3.1. On each element, the flow solution is represented using the high order triangular basis developed by Dubiner [59]. Spatial integration and differentiation operators for a function represented using this basis can be found in [60]. Time derivatives are approximated using a diagonally implicit Runge-Kutta (DIRK) scheme [61] that is third order accurate in time and is A-stable [62]. At each stage of the DIRK scheme the implicit problem is solved using a p-multigrid iterative algorithm. More details can be found in [63, 64]. All of the following calculations were done with fourth order polynomials which should give 5^{th} order spatial accuracy in the L_2 norm.

3.3 Proper Orthogonal Decomposition for Fluid Flow

This section provides a brief description of the POD method and how it is applied to the velocity and pressure fields. The bases for the reduced order models are derived from the detailed data using the proper orthogonal decomposition (POD). The POD was introduced by [2] as a means to extract the large-scale structures of turbulent flows. It uses data obtained from experiments or numerical simulations to generate an orthogonal set of spatial basis functions. These functions are optimal in terms of energy; the mean square inner product of a solution, $\boldsymbol{q}(\boldsymbol{x},t)$, with the function:

$$\left\langle (\boldsymbol{q}(\boldsymbol{x},t), \boldsymbol{\phi}_n(\boldsymbol{x}))^2 \right\rangle$$

is maximized under the constraint that $(\boldsymbol{\phi}_n(\boldsymbol{x}), \boldsymbol{\phi}_n(\boldsymbol{x})) = 1$, where $(\ , \ )$ is the L_2 inner product and $\langle\rangle$ indicates a time average. This maximization problem generates a sequence of orthogonal functions which herein are called POD modes,

With an adequate number of POD modes, we can approximate any solution as a linear combination of time-dependent weighting coefficients, $a_n(t)$, and the POD modes

$$\begin{aligned} \boldsymbol{q}(\boldsymbol{x},t) &= \sum_{n=1}^{M} a_n(t)\boldsymbol{\phi}_n(\boldsymbol{x}) \qquad (3.4) \\ &= \sum_{n=1}^{M} \left(\boldsymbol{q}(\boldsymbol{x},t), \boldsymbol{\phi}_n(\boldsymbol{x})\right) \boldsymbol{\phi}_n(\boldsymbol{x}), \end{aligned}$$

The derivation of the POD can be found in any of the following references [26, 30, 31, 45, 65]. In this work, the snapshot method of Sirovich [19] has been employed to derive the POD modes.

In most studies of POD-ROM for incompressible flows, the solution vector, $\boldsymbol{q}(\boldsymbol{x},t)$, consists of the velocity components only; the pressure term does not appear explicitly. There are several good reasons for this. Because the POD modes are derived from solution snapshots that are numerically divergence-free, the POD modes themselves are also divergence free. One can then show that by integrating the pressure terms in the Galerkin formulation of the Navier-Stokes equations by parts, these terms cancel out [6, 32, 34, 66, 67]. Furthermore if a zero pressure condition is applied on the outflow boundaries, no knowledge of the pressure is necessary to construct a ROM. There are disadvantages to this approach however. [23] and [12] have shown that for convectively unstable shear layers, non-zero boundary pressure terms must be considered. Furthermore, knowledge of the pressure is necessary to evaluate the forces on a structure [10]. This is particularly important for application of ROM to drag reduction.

To be able to directly incorporate the pressure into the POD formulation, following ideas from compressible flow[68], [69] let $\boldsymbol{q}(\boldsymbol{x},t) = \left(\sqrt{p(\boldsymbol{x},t)+p_0}, u(\boldsymbol{x},t), v(\boldsymbol{x},t)\right)$ where p_0 represented the atmospheric pressure. They then expanded for $p_0 \gg p$ to derive a method for obtaining the POD modes in the low Mach number limit. This method is attractive because the POD formulation then maximizes a meaningful flow quantity, the dynamic pressure, and the pressure and velocity fields are represented by a POD mode of the form $\boldsymbol{\phi} = (\Phi^p(\boldsymbol{x}), \Phi^u(\boldsymbol{x}), \Phi^v(\boldsymbol{x}))^T$. For this work, we take the simple approach of using the scaled non-dimensionalized flow variables $\boldsymbol{q}(\boldsymbol{x},t) = \left(\frac{p(\boldsymbol{x},t)}{\rho {u_\infty}^2}, \frac{u(\boldsymbol{x},t)}{u_\infty}, \frac{v(\boldsymbol{x},t)}{u_\infty}\right)$ to generate the POD modes. This is similar to the “pressure extended model” of [70]. The disadvantage of this approach compared to [69] is that the quantity maximized by the POD is dependent on the non-dimensionalization. In practice we have not found a significant difference between POD-ROMs derived using the two different approaches.

3.4 Reduced Order Modeling

The solution for $\boldsymbol{q} = [p, u, v]^T$ is sought in the space spanned by a subset of the POD modes, $\boldsymbol{\phi}$. That is the flow field for $\vec{\mathrm{q}}$ can be reconstructed as:

$$\boldsymbol{q} = \begin{bmatrix} p(\boldsymbol{x}, t) \\ u(\boldsymbol{x}, t) \\ v(\boldsymbol{x}, t) \end{bmatrix} = \sum_{n=1}^{N_r} a_n(t) \begin{bmatrix} \Phi_n^p(\boldsymbol{x}) \\ \Phi_n^u(\boldsymbol{x}) \\ \Phi_n^v(\boldsymbol{x}) \end{bmatrix} . \tag{3.5}$$

The goal of reduced order modeling is to generate a dynamical model to predict the evolution of the solution coefficients, $a_n(t)$. In the following, we compare three approaches for generating dynamical models, the Galerkin approach, the streamwise-upwind-Petrov-Galerkin (SUPG) approach and the spectral vanishing viscosity (SVV) approach. As mentioned in the introduction, previous authors have reported that it is difficult to generate accurate results for the long term simulation of fluid flow using the Galerkin approach [5, 26–28]. The goal is to determine the effectiveness of stabilized approaches at medium and high Reynolds number.

3.4.1 Galerkin ROM

The Galerkin approach to deriving a reduced order dynamical model to predict the evolution of the solution coefficients $a_n(t)$ is to use the POD modes as the test functions in the weak form of the Navier-Stokes equations

$$\int\int_{\Omega} \left[\boldsymbol{\phi}_n^T \frac{\partial \boldsymbol{w}}{\partial t} - \frac{\partial \boldsymbol{\phi}_n^T}{\partial x}\ \mathbf{e}_x - \frac{\partial \boldsymbol{\phi}_n^T}{\partial y}\ \mathbf{e}_y \right] d\Omega + \int_{\Gamma} \boldsymbol{\phi}_n^T (\ \mathbf{e}_x,\ \mathbf{e}_y) \cdot \mathbf{n}_{\Gamma} \mathrm{d}\Gamma = 0 \tag{3.6}$$

where $\vec{\mathrm{n}}_\Gamma$ is the outward normal to the domain boundary Γ. This results in a system of scalar equations for the coefficients a_n. Note that for a finite number of POD modes, N_r, this becomes a reduced order or low dimensional model. Using

N_s modes would lead to the exact value of $\vec{\mathrm{q}}$ for the time interval over which the POD modes were generated.

3.4.2 Streamwise-Upwind-Petrov-Galerkin (SUPG) ROM

The first approach to stabilize the POD based ROM is streamwise-Upwind-Petrov-Galerkin (SUPG) approach. As mentioned in section 3.2, this is also the method used to perform the detailed solutions. An advantage of the SUPG approach over other stabilized methods is that there are no adjustable parameters in SUPG. O'Donnell and Helenbrook [69] and [70] have both suggested that SUPG ideas could be used in the development of stabilization models for POD. The SUPG equations are

$$0 = \int\int_{\Omega} \left[\boldsymbol{\phi}_n^T \frac{\partial \boldsymbol{w}}{\partial t} - \frac{\partial \boldsymbol{\phi}_n^T}{\partial x}\ \mathbf{e}_x - \frac{\partial \boldsymbol{\phi}_n^T}{\partial y}\ \mathbf{e}_y \right] d\Omega + \int_{\Gamma} \boldsymbol{\phi}_n^T\,(\ \mathbf{e}_x,\ \mathbf{e}_y) \cdot \mathbf{n}_\Gamma \mathrm{d}\Gamma +$$
$$\sum_{e=1}^{N_e} \int\int_{\Omega_e} \left[\frac{\partial \boldsymbol{\phi}_n^T}{\partial x} \frac{\partial \mathbf{f}_x}{\partial(p, \rho u, \rho v)} + \frac{\partial \boldsymbol{\phi}_n^T}{\partial y} \frac{\partial \mathbf{f}_y}{\partial(p, \rho u, \rho v)} \right] \mathrm{T} \left[\frac{\partial \boldsymbol{w}}{\partial t} + \frac{\partial\ \mathbf{e}_x}{\partial x} + \frac{\partial\ \mathbf{e}_y}{\partial y} \right] d\Omega \quad \forall n \in [1, N_r] \tag{3.7}$$

where N_e is the number of elements in the mesh, Ω_e is the area of each element, and the matrix T is the SUPG stabilization matrix. The first two integrals are the standard Galerkin formulation with the first being the volumetric bi-linear functional and the second the contribution of the boundary conditions. The third integral is the SUPG stabilization, where T is given by

$$T = \frac{h_P}{\sigma} \mathrm{diag}[S, 1, 1], \tag{3.8}$$
$$h_p = h/P^2,$$
$$\sigma^2 = \max[S^2, 0.1u_\infty^2] + (h_p/\Delta t + \nu/h_p)^2,$$
$$S^2 = \max_{\Omega_e}[u^2 + v^2],$$

and h is the diameter of the inscribed circle of each triangular element, P is the polynomial degree of the element which for these calculations was always 4, Δt

is the time step of the calculations, and ν is kinematic viscosity. Note that this stabilization depends on the underlying mesh used to calculate the modes.

There are two advantages to this approach. First, the SUPG formulations allows one to use any set of modes for the velocity and the pressure; no restrictions are placed on the choice of pressure and velocity spaces. Second, the SUPG formulation is a consistent residual-based stabilization, implying that the exact solution will satisfy the weighted integral form. This can be seen by the fact that the last term in brackets in (3.7) is the governing equation, which would be zero if evaluated using the exact solution. Thus, if the reduced-order-modeling basis can accurately represent the exact solution, it will satisfy the discrete equation. This is not true of artificial viscosity approaches that add terms to the governing equation to stabilize the method.

3.4.3 Spectral Vanishing Viscosity ROM

The spectral vanishing viscosity stabilization (SVV) approach was first introduced by Tadmor [42]. The general idea is to stabilize the computation by introducing a dissipative term that is only active in the small-scale range of the spectrum. The SVV approach allows more flexibility than SUPG but contains two empirical coefficients that must be adjusted. These are an artificial viscosity magnitude and a kernel function that determines the dissipative subrange. The connection between the resolved scales and the parameters of SVV was studied by [71–73]. Here we use the standard SVV formulation [42]. The formulation is similar to the Galerkin formulation, except with a modified flux,

$$\sum_{e=1}^{N_e} \Bigg\{ \int\int_{\Omega} \left[\boldsymbol{\phi}_n^T \frac{\partial \boldsymbol{w}}{\partial t} - \frac{\partial \boldsymbol{\phi}_n^T}{\partial x} \left(\boldsymbol{e}_x - \boldsymbol{s}_{xn} \right) - \frac{\partial \boldsymbol{\phi}_n^T}{\partial y} \left(\boldsymbol{e}_y - \boldsymbol{s}_{yn} \right) \right] d\Omega + \int_{\Gamma} \boldsymbol{\phi}_n^T \left(\boldsymbol{e}_x, \boldsymbol{e}_y \right) \cdot \mathbf{n}_{\Gamma} d\Gamma \Bigg\}_{n=1,\ldots,N_r} = 0, \tag{3.9}$$

where the additional flux terms are given by $\boldsymbol{s}_{xn} = Q_n(\epsilon/\mu)\boldsymbol{\tau}_x$ and $\boldsymbol{s}_{yn} = Q_n(\epsilon/\mu)\boldsymbol{\tau}_y$, with

$$Q_n = \begin{cases} 1 & n > K \\ 0 & n < K \end{cases} \tag{3.10}$$

where ϵ is SVV viscosity amplitude which is assumed to be constant, Q is a viscosity kernel and n is the index for the reduced-order modeling basis. The basis is assumed to be organized such that larger n indicates small-scale POD modes. K is an integer cutoff above which the SVV is activated. K and ϵ must be found empirically. This makes SVV worth being studied however, is the fact that one can vary these parameters to investigate how stabilization affects the reduced order model.

Although standard SVV was developed for methods that operate with hierarchical discretization [42, 74], there is a disadvantage in combining SVV with POD-ROM in comparison with spectral methods. In the Fourier spectral method, the viscous terms act on each mode independently, but this is not true when using POD modes.

3.5 Low Reynolds Case

In this section, ROMs are tested for a 2D incompressible flow over an NACA0015 airfoil at $Re = 1000$ which corresponds to the laminar flow regime. The flow conditions are listed in table 3.1. An unstructured triangular mesh on a circular domain is used in all the detailed simulations as shown in Fig. 3.1. The mesh consists of 34032 triangles and the basis functions composed of quartic polynomials on each element. There are 41 elements are on the surface of the airfoil which for $P = 4$ gives 164 surface nodes. The time step of diagonally implicit Runge-Kutta (DIRK) scheme is $\Delta t = 0.025$. The detailed simulations were run until they reached a periodic state and then ROMs were derived from data taken from the periodic state.

Term	Condition
Airfoil	NACA0015
Reynolds number	1000
Angle of attack	12°
Time interval used to generate the modes	3
Number of snapshots	120

Table 3.1: POD-ROM characteristics

Contours of the u-velocity are shown in Fig. 3.2. For this angle of attack, the flow separates near the leading edge of the airfoil and the wake of the separated region then sheds alternating vortices of opposite vorticity. To show the periodic nature of the flow, a point probe was taken at the location $(2.09, 0.00)$. The time history of the u and v velocity at the probe location are shown in Fig. 3.3. The Strouhal number of the flow is 0.76 where the Strouhal number is defined as $c/(u_\infty T)$ where c is the chord length, u_∞ is the free-stream velocity, and T is the period of the oscillation. Fig. 3.3 shows that the flow is nearly perfectly periodic.

As discussed in section 3.3, the POD modes are evaluated using the snapshot method introduced by Sirovich [19]. The size of the eigenvalue problem for the snapshot method is equal to the number of snapshots so it is computationally advantageous to reduce the number of snapshots required to create the modes. Previous numerical studies by Noack et al. [23] showed that the first N POD modes can be computed from $2N$ snapshots. According to this work, an increase to $4N$ or more samples did not have any significant effect on the resulting models. In our previous work [75], we showed that the adequate number of snapshots depends on the time scales of the flow. To be confident about the quality of the modes, the snapshots should resolve the smallest time scale of the flow. Based on this logic, modes were constructed using 120 consecutive time steps of the detailed simulations, which corresponds to a non-dimensional time interval of 3. As shown in Fig. 3.3, This guarantees that we capture more than one whole vortex shedding period. Furthermore, if we had used every other snapshot, the time evolution in the region where the sharp drop-off in the v-velocity occurs would not be adequately resolved. The POD eigenvalue spectrums for $N_s = 120$ and $N_s = 60$ are shown in Fig. 3.4. The spectrum with $N_s = 60$ deviates from the spectrum with $N_s = 120$ at

N_r	Energy summation
5	0.9859
11	0.9981
15	0.9991
21	0.9999

Table 3.2: Normalized energy summation for low Reynolds number case

mode 18 which has an energy that is 9 orders of magnitude lower than the energy of the first mode. Therefore, 120 snapshots is a reasonable number of snapshots for generating the POD modes.

Further examining the eigenvalue spectrum shows that the first mode has a huge fraction of the energy. As shown in Fig. 3.5a and 3.5b, this mode is essentially the mean of the flow. After the first mode, the eigenvalues come in pairs of equal magnitude. This is typical of a convective problem and corresponds to POD mode pairs that are similar to sine / cosine pairs. Examples for mode 2 and mode 6 are shown in the remaining frames of Fig. 3.5. These modes capture the propagation of the vortices through the wake. Higher index modes correspond to higher wavenumber modes similar to a Fourier series.

The energetic optimality of the POD basis functions suggests that only a few POD modes could accurately describe the flow. As a reference point for understanding this, we have also plotted the curve $1/N^2$ in Fig. 3.4. This is the slowest decaying series that will converge. For this laminar case, it is clear that the POD series will rapidly converge. To measure the effectiveness of the POD modes in representing the flow, the ratio of energy captured by the reduced order model to the energy of the entire spectrum, $= \sum_{i=1}^{N} \lambda_i / \sum_{i=1}^{N_s} \lambda_i$ is usually used. In practice, the size of POD-ROM simulation, N_r, is usually determined as the smallest integer such that this ratio is greater than a certain value [6, 7, 13, 29, 31]. Table 3.2 shows the normalized energy sums when using 5, 11, 15 and 21 modes. (These are the number of modes used in the ROMs in the next section.) In agreement with the energy spectrum, the energy sum also shows that only a small number of modes should be necessary to get accurate results.

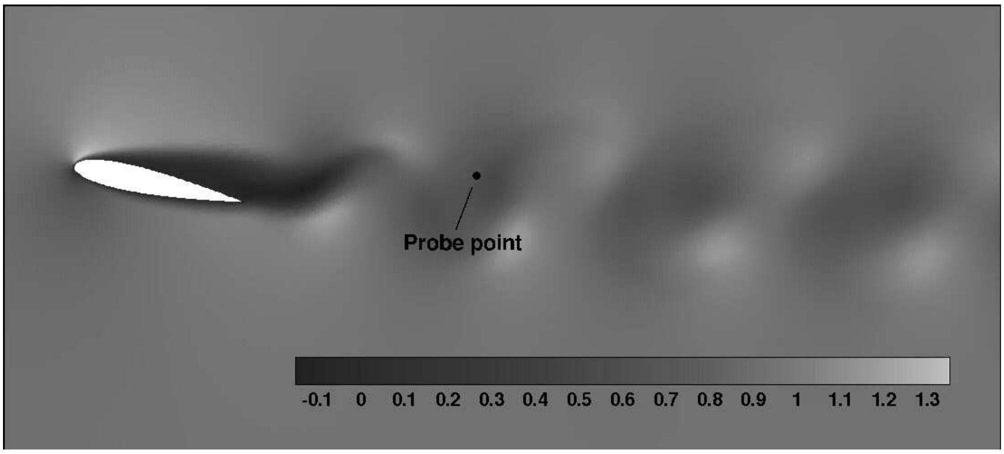

Figure 3.2: Instantaneous u-velocity contours, $Re = 1000$.

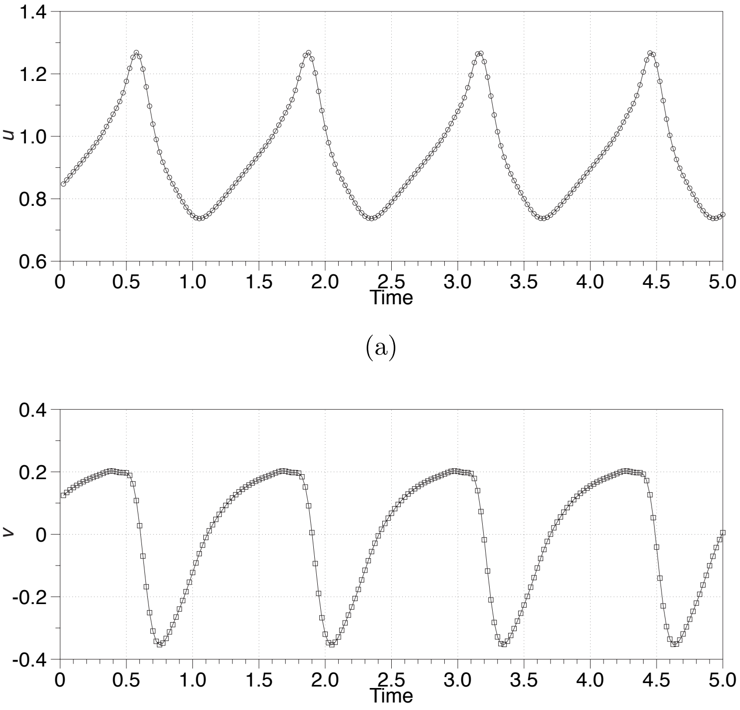

(a)

(b)

Figure 3.3: Instantaneous u and v velocity at probe location, $Re = 1000$.

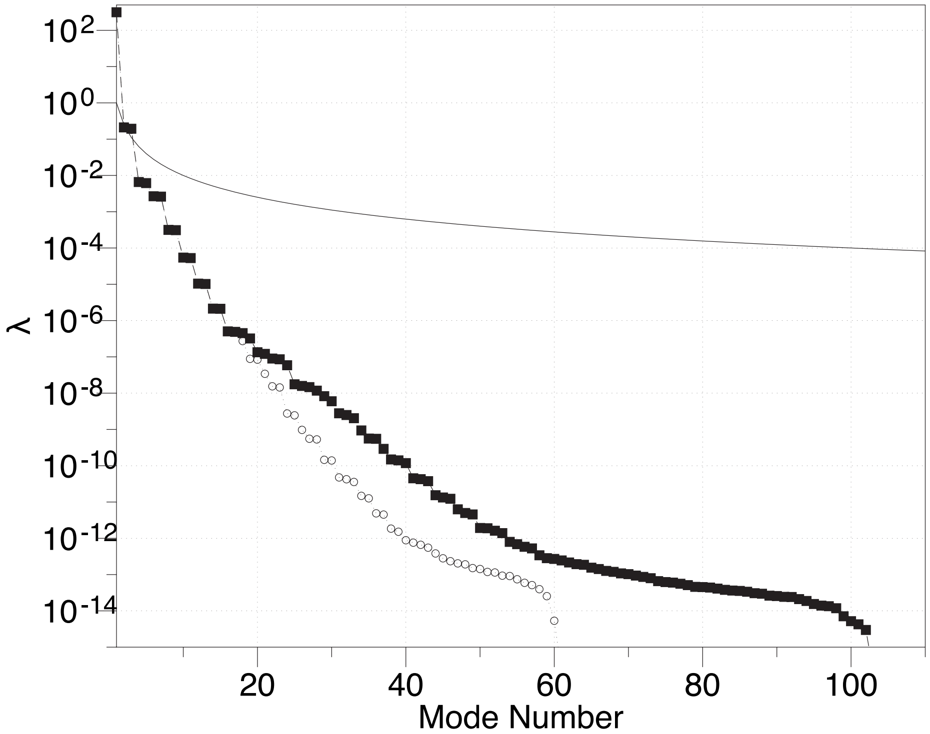

Figure 3.4: POD mode eigenvalues with $N_s = 120$ (–■–) and $N_s = 60$ (○). $1/N^2$ convergence (solid line).

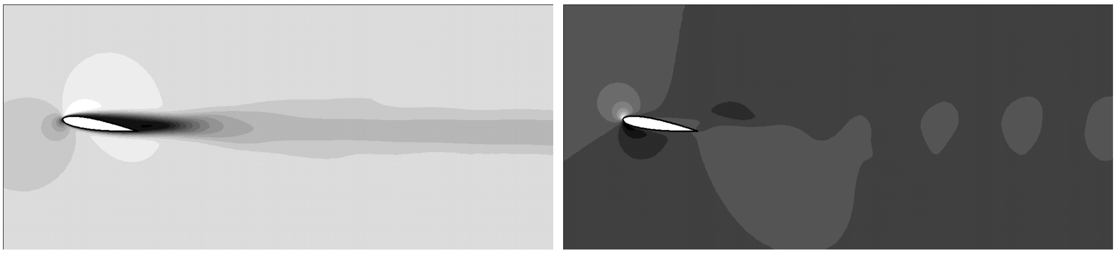

(a) Mode 1 of u velocity

(b) Mode 1 of v velocity

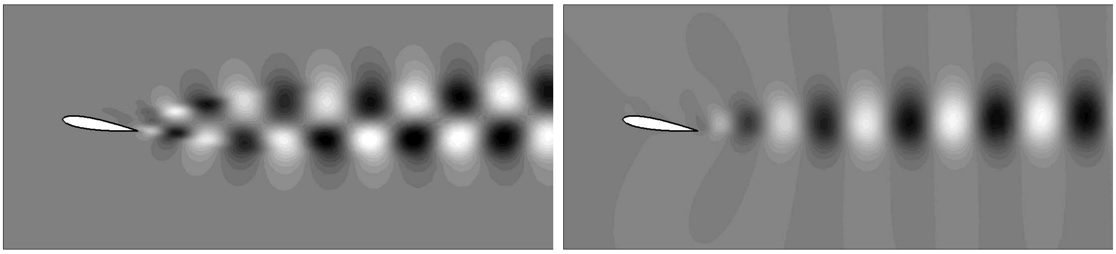

(c) Mode 2 of u velocity

(d) Mode 2 of v velocity

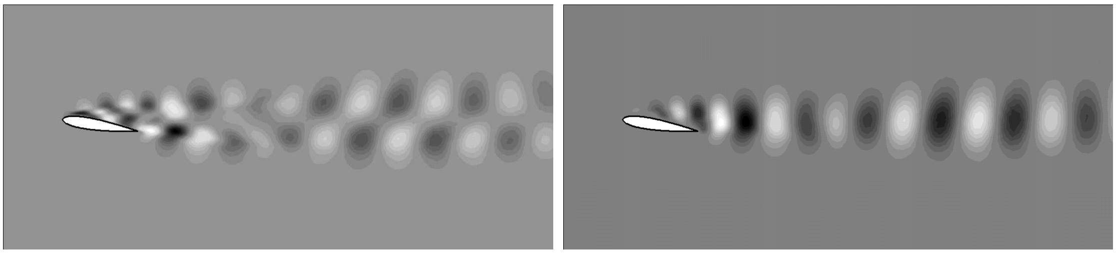

(e) Mode 6 of u velocity

(f) Mode 6 of v velocity

Figure 3.5: Representation of some POD modes. u velocity POD modes (left) and v velocity POD modes (right). Dashed lines show the negative values.

3.5.1 Results for Galerkin ROM

In this section, Galerkin POD-ROMs having $N_r = 5, 11, 15$, and 21 (the entries in table 3.2) are examined. The initial conditions for the POD-ROM i.e. $(a_1, a_2, \ldots, a_{N_r})_{t=0}$ are calculated by projecting the initial solution snapshot onto the ROM space. The POD-ROM simulation is then performed for 230 vortex shedding cycles.

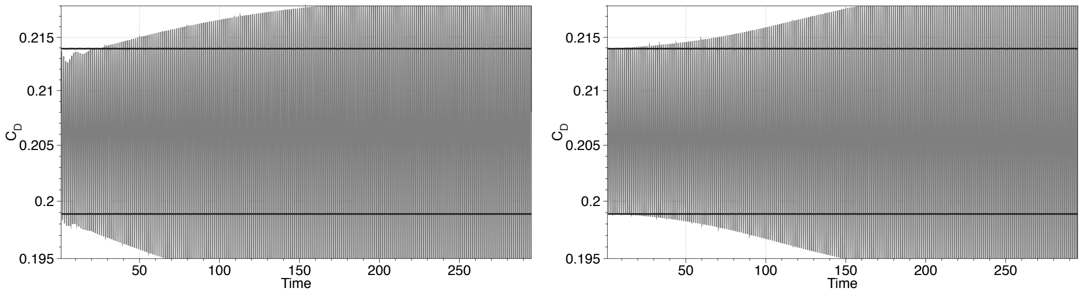

(a) $N_r = 5$, No stabilization (b) $N_r = 11$, No stabilization

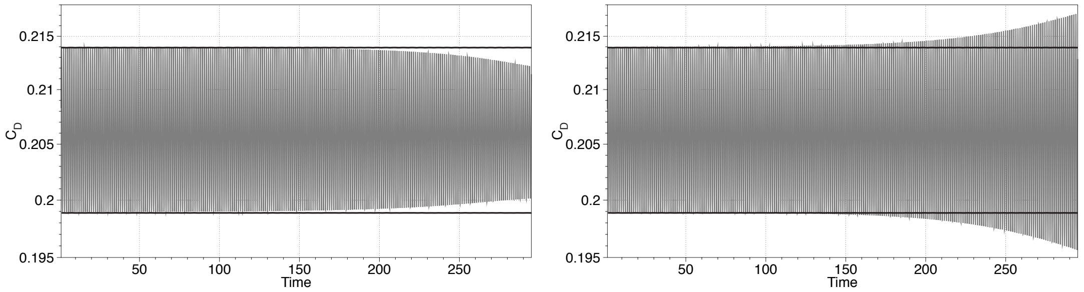

(c) $N_r = 15$, No stabilization (d) $N_r = 21$, No stabilization

Figure 3.6: Envelopes of C_D of detailed simulation (solid lines) and C_D of 4 Galerkin POD-ROM cases from table 3.2 (gray).

The evolution of the drag coefficient, C_D, for the 4 Galerkin POD-ROMs is shown in Fig. 3.6. For reference, the amplitude of the oscillations as predicted by the detailed simulation is shown as black curves on the figure. For the Galerkin POD-ROM system with 5 modes (Fig. 3.6a), the result deviates from the DNS almost immediately. With 11 modes the deviation is less rapid and becomes visually detectable after about 15 time units. For the Galerkin POD-ROM system with 15 and 21 modes (Fig. 3.6c and d) the simulation is accurate for nearly 150 time units. From this we conclude, as many previous authors have, that for any fixed amount of simulation time the Galerkin model converges as the number of modes increases, but a large number of modes are needed to accurately reproduce the periodic limit cycle. Typically many authors use the guideline that N_r should be chosen such that 99% of the energy is captured. Clearly this is insufficient to accurately reproduce the limit cycle when using a Galerkin ROM.

3.5.2 Results for SUPG ROM

To investigate the effect of stabilization, the evolution of the drag coefficients, C_D, for the 4 SUPG based POD-ROMs is shown in Fig. 3.7. The improvement with stabilization is obvious when comparing Fig. 3.6 and 3.7. Even with 5 modes, the simulation reproduces the limit cycle minimum and maximum drag within 1%. This error decreases as the number of modes increase. With 15 and 21 modes, the simulations reproduce the amplitude of the oscillations in C_D to the point that they are visually indistinguishable from the detailed simulation in the figure. This indicates that SUPG is less sensitive to truncation errors than the Galerkin model and can accurately predict the limit cycle. Ref. [43] found that, when simulating 3D fluids flows with a calibration method, the error rapidly grows outside the temporal window used to generate the POD modes. In this periodic flow, only the first two shedding cycles were used to derive the POD modes and obviously that behavior was not observed.

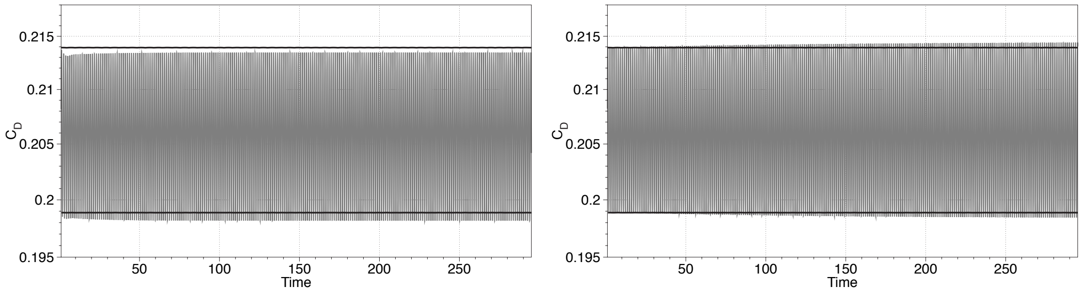

(a) $N_r = 5$, SUPG (b) $N_r = 11$, SUPG

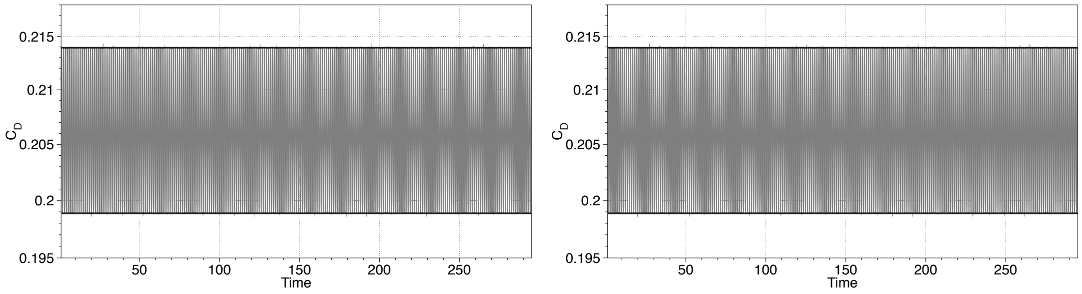

(c) $N_r = 15$, SUPG (d) $N_r = 21$, SUPG

Figure 3.7: Envelopes of C_D of detailed simulation (solid lines) and C_D of 4 SUPG based POD-ROM cases from table 3.2 (gray).

C_D is calculated from the pressure and velocity gradients adjacent to the airfoil surface and thus does not provide information about where the maximum error occurs. Contours of velocity error at the end of the 230^{th} vortex shedding period for the 21 dimensional POD-ROM is shown in Fig. 3.8. Since u_∞ is one, the absolute error is almost the same as the relative error. The figure shows that the largest errors occur in the few vortices behind the airfoil and that the maximum error is less than 2.0%.

Since we know the exact solution, a quantitative comparison of the coefficients obtained from detailed solution and coefficients obtained from POD-ROM is permitted. The time evolution of a_2, a_4, a_6, and a_8 as well as the exact values for a few vortex shedding cycles around 230^{th} shedding cycle are represented in Fig. 3.9. SUPG results for 15 and 21 modes and Galerkin results with 15 modes are shown. The values show that the amplitude of the coefficients of 15 and 21 dimensional systems are almost the same but the phase shift for the 15 modes simulation is greater. The Galerkin result has phase and amplitude error. This is true for all four coefficients shown.

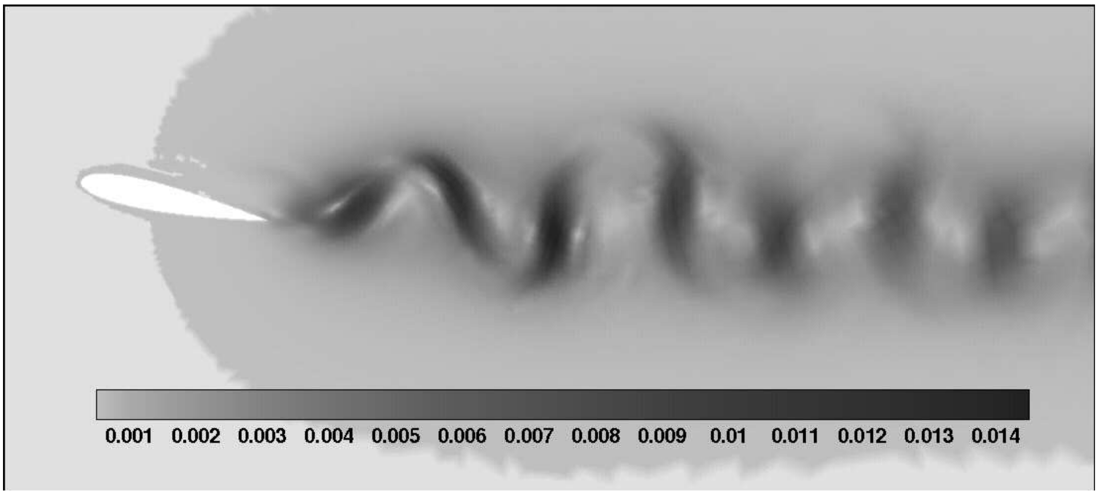

Figure 3.8: Contour of $\sqrt{(u_{Detailed} - u_{ROM})^2 + (v_{Detailed} - v_{ROM})^2}$ after 230 shedding cycles.

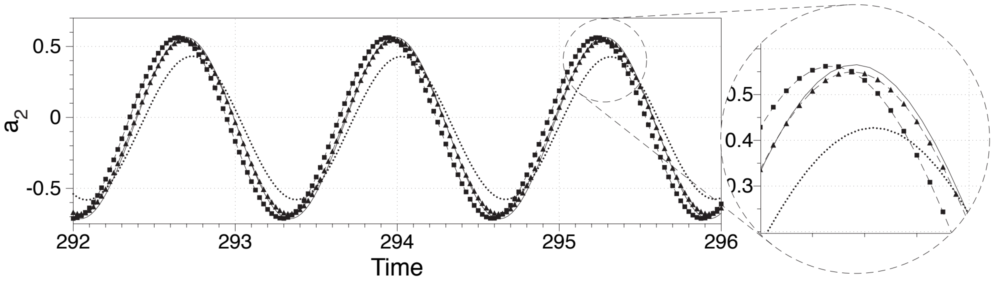

(a) POD coefficients of mode 2

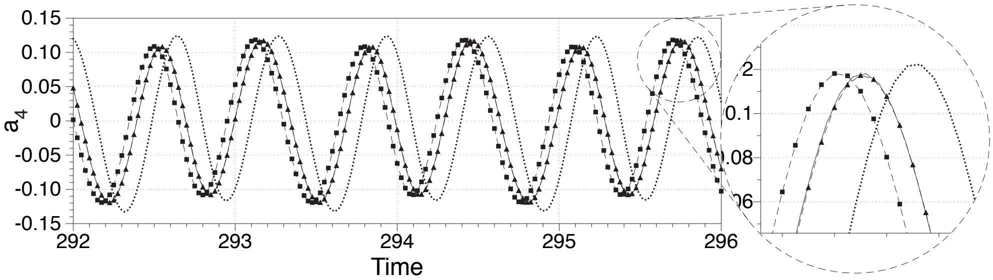

(b) POD coefficients of mode 4

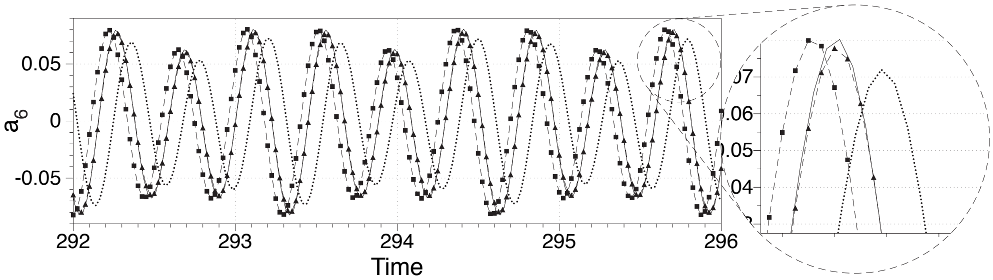

(c) POD coefficients of mode 6

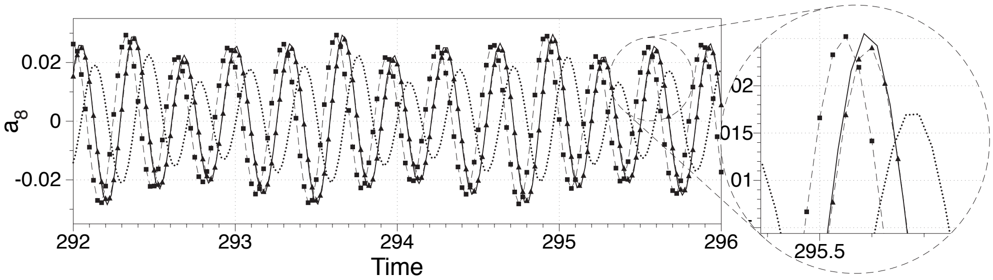

(d) POD coefficients of mode 8

Figure 3.9: Temporal evolution of the predicted POD-ROM coefficients in comparison with projected over detailed simulation. Detailed simulation(—), 15 modes simulation (–■–), 21 modes simulation (–▲–) and 15 modes simulation without stabilization (⋯).

Term	Condition	N_r	K	ϵ
Case 7	SVV	15	7	10^{-4}
Case 8	SVV	15	7	10^{-3}
Case 9	SVV	15	9	10^{-4}
Case 10	SVV	15	9	10^{-3}
Case 11	SVV	15	11	10^{-4}
Case 12	SVV	15	11	10^{-3}

Table 3.3: Brief description of the different SVV-ROMs for comparison of SUPG and SVV

3.5.3 Results for SVV ROM

For completeness, SVV and SUPG are compared by repeating the flow example already presented in the previous section using SVV stabilization. The same POD modes and the same initial conditions are used as in the SUPG and Galerkin cases. Several different SVV formulations have been used by previous authors. For example, Tadmor [42] used $\epsilon K = 0.25$, Maday et al. [76] used $K = 5\sqrt{N_r}$, and [77] used $K = 2\sqrt{N_r}$. We have tried six different formulations which are shown in table 3.3. The amplitude and cutoff number are chosen empirically. Based on [77], K would be around 7.75 which falls into the range of conditions tested.

Time histories of C_D are depicted in Fig. 3.10. The results show that with $K = 7$ (a & b) the range of modes over which artificial viscosity is applied is too wide and the amplitude of the limit cycle is too small. For larger K however, the limit cycle grows in amplitude. When studying the 1D Burgers' equation, [77] found that increasing the cut-off wavenumber, K, increases oscillation amplitudes, but that the amplitude is more sensitive to changes in ϵ. In this study, K seems to determine growth or decay, while ϵ affects the time scale of the process. For example, all of the simulations with $\epsilon = 10^{-4}$ evolve on a longer time scale than the cases with $\epsilon = 10^{-3}$. Playing with ϵ and K might lead to more accurate results, but many more numerical experiments would be required to accomplish this. Furthermore, it is not clear how robust such a model would be to changes in flow conditions. Thus, for the following high Reynolds number studies, we do not include SVV results.

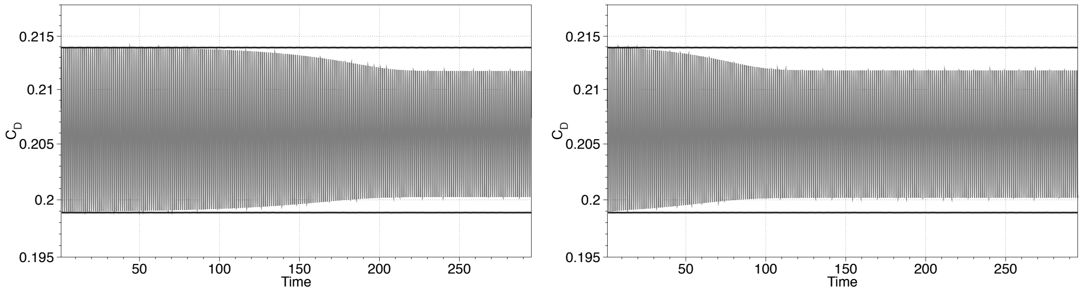

(a) $K = 7$, $\epsilon = 10^{-4}$ (b) $K = 7$, $\epsilon = 10^{-3}$

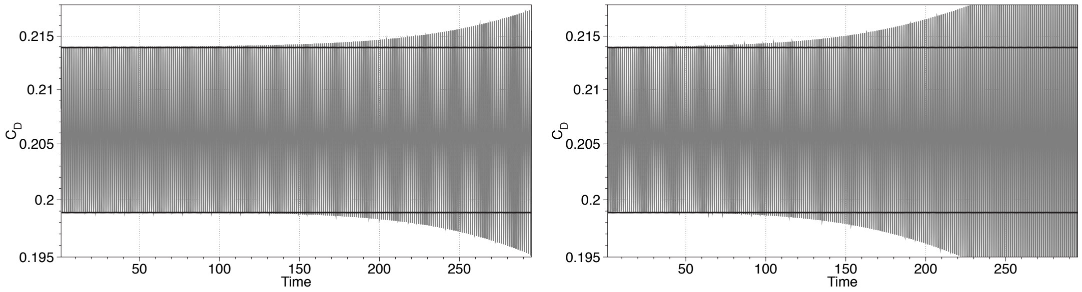

(c) $K = 9$, $\epsilon = 10^{-4}$ (d) $K = 9$, $\epsilon = 10^{-3}$

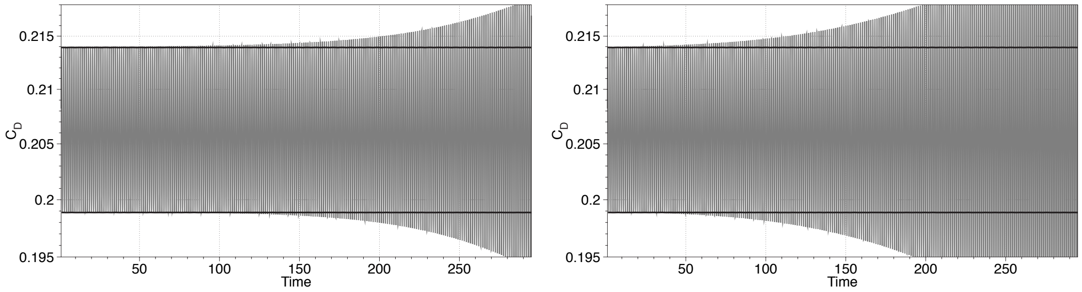

(e) $K = 11$, $\epsilon = 10^{-4}$ (f) $K = 11$, $\epsilon = 10^{-3}$

Figure 3.10: C_D of detailed simulation (gray line) and envelopes of C_D of SVV simulations for the different values of K and ϵ given in table 3.3.

3.6 High Reynolds Number Case

POD is a powerful tool for laminar flow because POD extracts the main structures of the flow based on energy content. In the laminar regime typically only a few modes are enough to describe the flow accurately. This is shown by the sharp decline of the POD eigenvalues. In turbulent flows, the energy is distributed over a wider range of scales and consequently more POD modes will be needed to

Table 3.4: POD-ROM characteristics

Term	Re	Domain radius (times the chord length)	Angle of Attack
Case study 1	$100,000$	10	15°
Case study 2	$100,000$	10	9°
Case study 3	$100,000$	5	15°

describe the flow. Furthermore, the dynamics of turbulent flows are more complex so this also will make obtaining accurate results more difficult. As mentioned in the introduction, most of the numerical investigations of POD-ROM have been done at low Reynolds numbers. In this section, we investigate the stability and dynamics of two-dimensional high Reynolds number $(100,000)$ uniform flow over a NACA0015 airfoil. Particular attention is paid to the long term behavior of the POD-ROM.

High-resolution direct numerical simulations are employed to obtain flow samples from which the POD modes are extracted. The three cases listed in table 3.4 have been studied. To resolve the turbulent flow features, the mesh was adapted using the technique given in [78]. They meshes consist of $524,702$, $474,736$ and $405,728$ triangles and are refined in the boundary layer and the separated shear layer. The adapted mesh for case study 2 is shown in Fig. 3.11. There are 4702 elements on the surface of the airfoil which for $P = 4$ gives $18,808$ surface nodes. The time step of the diagonally implicit Runge-Kutta (DIRK) scheme was $\Delta t = 1/160$. The calculations were run on 2 processors. The detailed simulations were run until they reached a quasi-periodic state (as the flow is chaotic, it is never truly periodic) and then ROMs were derived from data taken from this state.

It is worth acknowledging the fact that the simulated flow is 2D. Although the Reynolds number is high, it is not true turbulence because turbulence is always 3D. The 3D mesh size for our flow configuration would be too large for our computational facilities, and as we will show, even generating accurate models for 2D turbulence is challenging.

Fig. 3.12 shows instantaneous u and v-velocity contours from the detailed simulation of case study 1. The flow separates near the airfoil leading edge and the

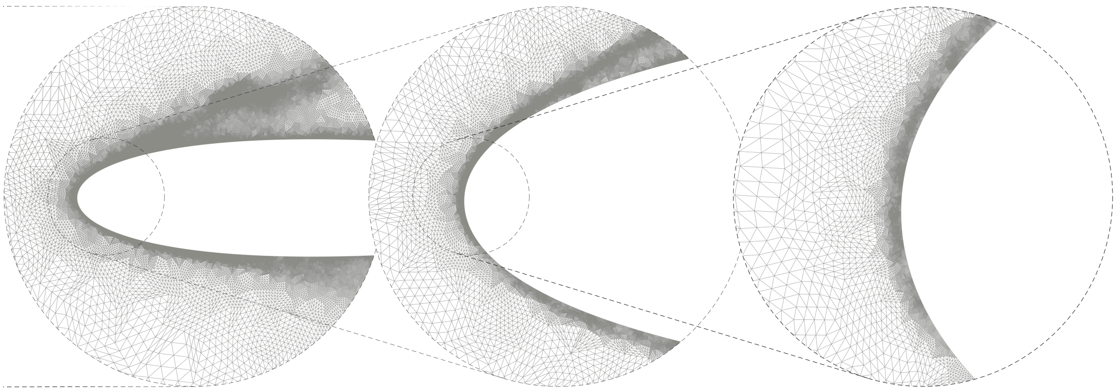

Figure 3.11: *hp*-Finite element mesh (chord length of the NACA0015 airfoil=1; Radius of domain=10.)

resulting shear layer sheds vortex pairs into the wake. These vortices interact and can merge or circulate around each other. Just after the trailing edge of the airfoil, there is another shear layer due to the velocity difference between the top and bottom of the airfoil. This shear layer tends to oscillate with a flapping motion and also generates vortices.

3.6.1 Mode generation

Two questions must be answered for a non-periodic flow. First, what time interval is necessary to achieve a converged POD decomposition? For a periodic flow, we know that one period is enough to generate converged POD modes and that those modes are able to predict the long term flow. However, for the the high Reynolds case, the time interval needed is not obvious. Second, for a fixed time interval, how many snapshots are necessary to achieve a converged POD decomposition? As mentioned previously, the number of snapshots needed for generating the POD modes depends on the time scales of the flow. For a chaotic flow however, it may not be necessary to resolve the smallest time scales because the flow is ergodic.

3.6.1.1 Effect of Time Window

To determine the answer to the first question, the POD modes are generated using every snapshot of the detailed simulations over time windows with different

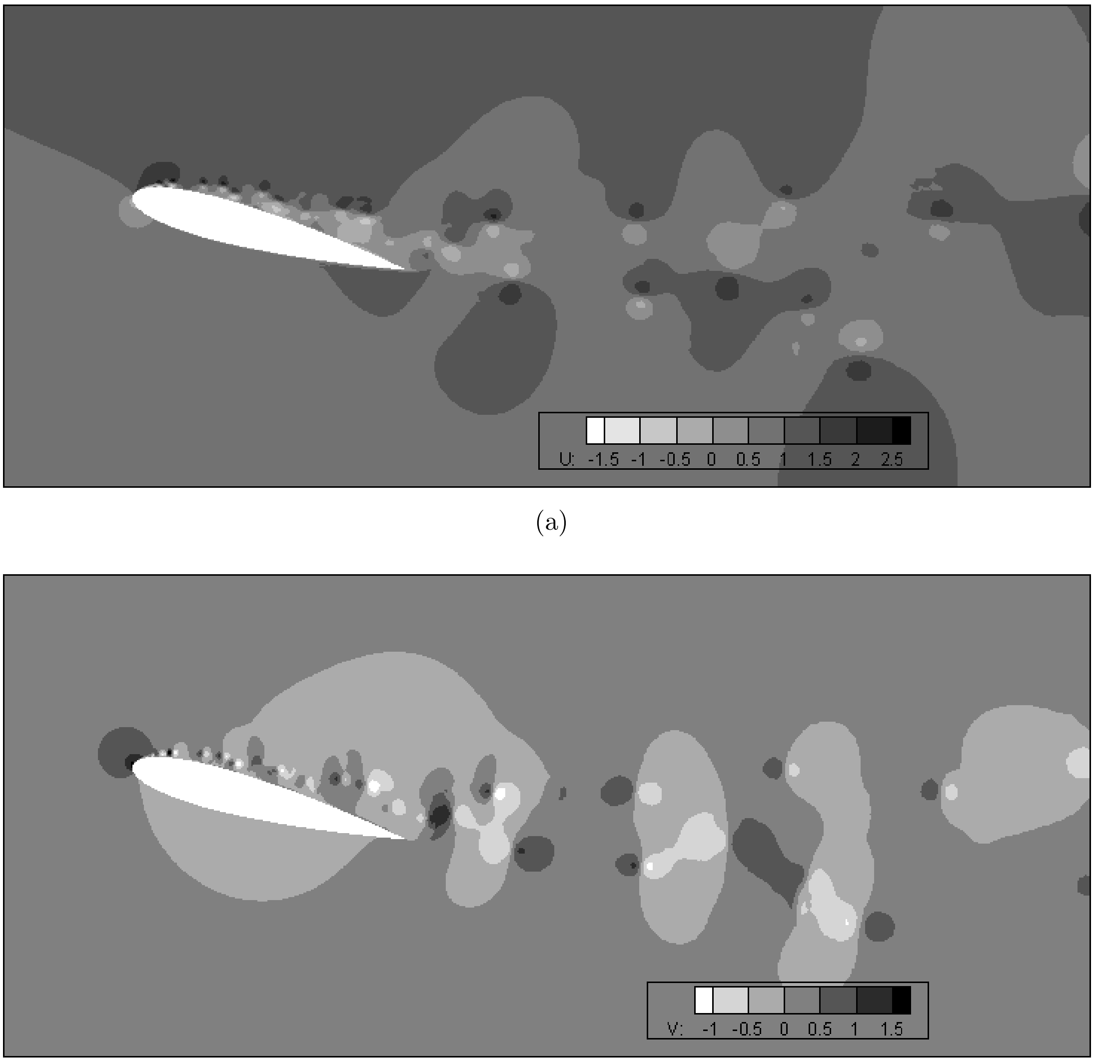

(a)

(b)

Figure 3.12: Contour of instantaneous u and v-velocity field from detailed simulation.

lengths. The length of time windows are from $T = 0.3125$ units (50 time steps) up to $T = 26.25$ units (4800 time steps) long. Fig. 3.13 shows the eigenvalue spectrum from case 1. Each curve corresponds to an eigenvalue spectrum for a different length time window. As the length of the time window increases, the rate of decay of the eigenvalue spectrum decreases. For time intervals smaller than the time required to propagate an entire domain length ($T = 10$), the eigenvalue spectrums decay more rapidly, but once this time interval is crossed, a fairly slow eigenvalue decay is established and the rate of decay decreases further as the time window increases. For a long time window, the rate of decay is barely faster than the series $1/N^2$ which is shown as the dashed black curve.

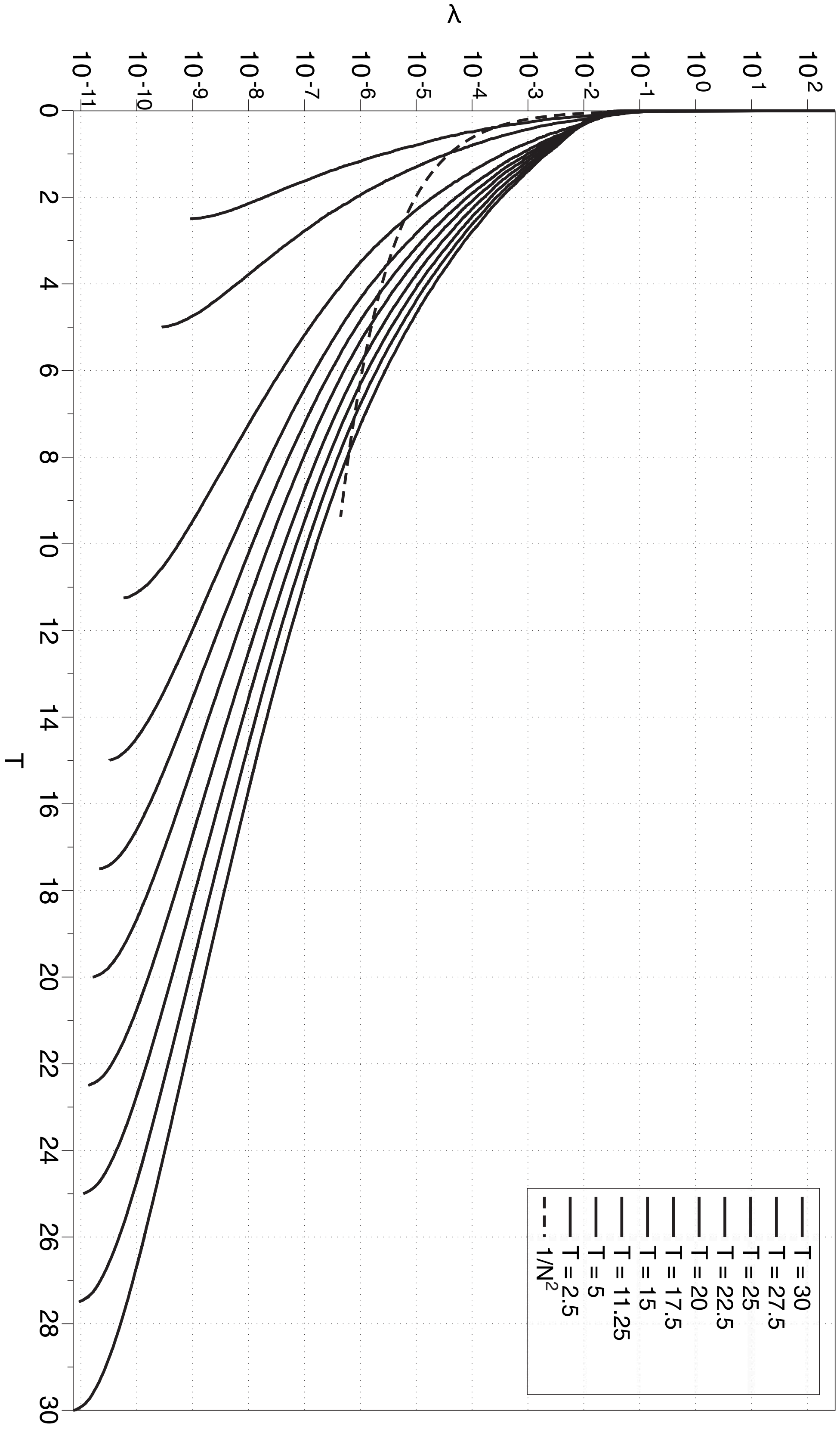

Figure 3.13: POD mode eigenvalues with different time length (number of snapshots) for case study 1.

Fig. 3.14 shows similar results for the domain size of 5. The results are shifted down slightly because the area of the domain is smaller (the eigenvalues represent the integration of energy over the domain), but the spectra show almost exactly the same trends. In this case, the time to propagate the entire domain is $T = 5$. Again when the time interval is shorter than this, there is a more rapid decay. For longer time windows, the decay is quite slow. The eigenvalues for case 2, which are not shown, show a similar behavior so it is not the flow separation that causes the slow decay. We conclude that the propagation of the vortices through the wake results in a very slow decaying spectrum. Note that the laminar case also involved vortex propagation, but here, the vortices are smaller scale, more sharply defined, intermittent, and propagate in pairs in somewhat random directions (with no periodicity).

Fig. 3.15 shows the number of POD needed to capture 90% and 99% of fluctuating energy for case study 1. This figure shows that the number of modes needed to capture 90% and 99% of fluctuating energy is basically increasing linearly with the length of the time window. Eventually, this curve should reach a plateau, but there is little evidence that this is happening, only a very slight negative concavity to the curve. Note that, although the eigenvalue spectrums shown in Figs. 3.13 and 3.14 seem to be converging as the time window is lengthened, this plot is on a logarithmic scale and the actual magnitude of the changes in the curves is remaining nearly constant. Thus, a time interval of 30 chord times is not long enough to determine an eigenvalue spectrum that is independent of the time window. This also indicates that one will likely need a large number of modes for a ROM that accurately reproduces the long term behavior of the flow (as verified below).

To understand the effect of the length of the time window on the shape of the POD modes, Fig. 3.16 shows the u and v components of the first eigenfunction for different time windows for Case 1. The first mode is basically the mean of the flow. Comparing the results of the three cases, it is clear that $T = 3.125$ is too short to achieve a converged mean. However, there are only slight differences between mode 0 calculated with a time interval of 11.25 and 30 time units.

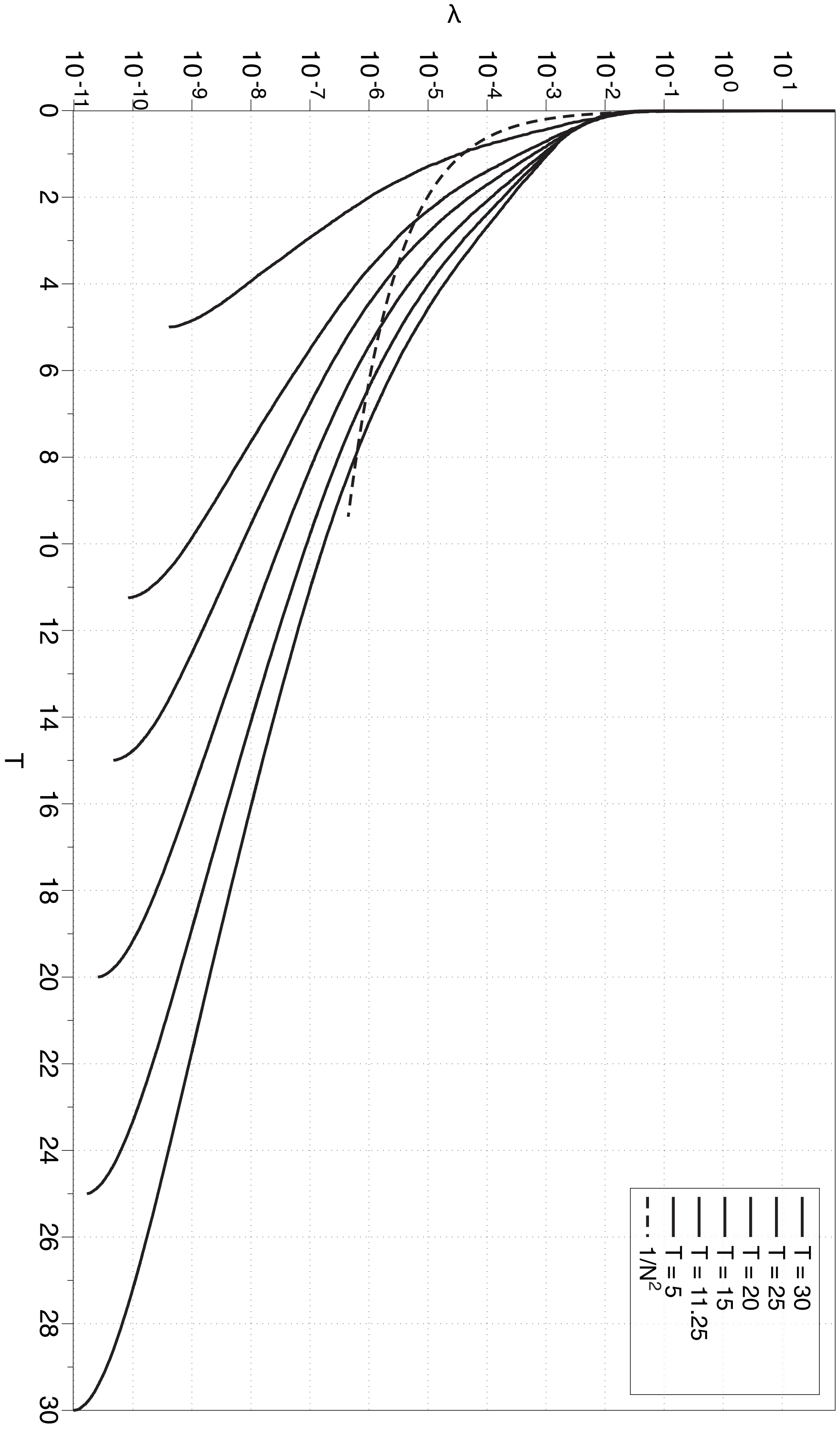

Figure 3.14: POD mode eigenvalues with different time length (number of snapshots) for case study 3.

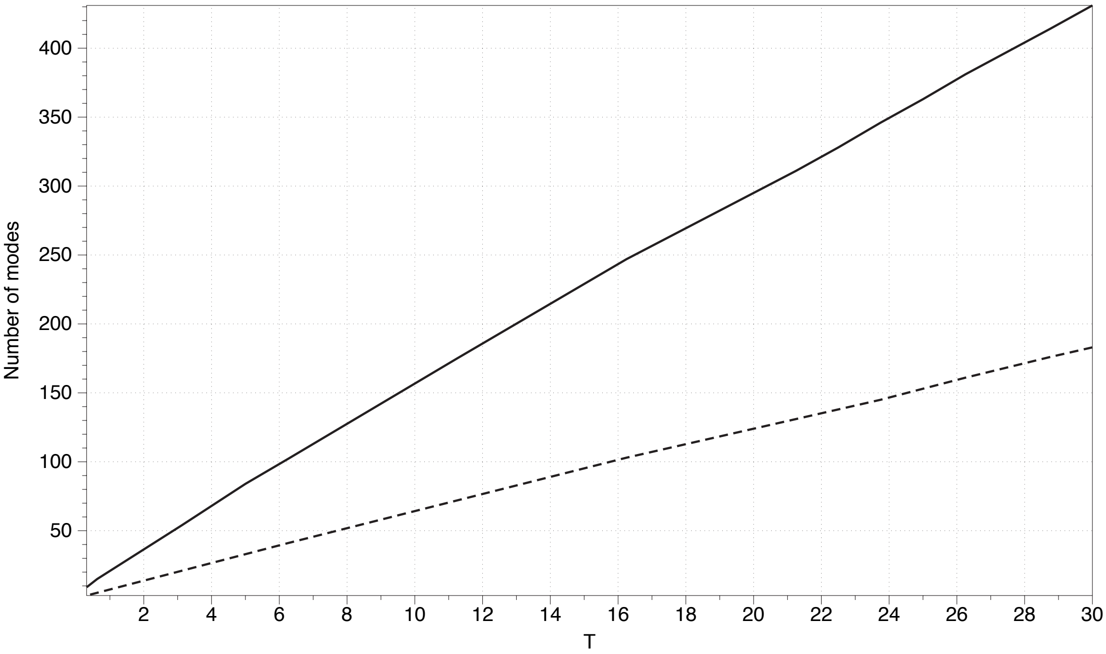

Figure 3.15: Case study 1, number of POD modes needed to capture 90% (dashed) and 99% (solid) of the energy as a function of the length of the time window T.

Fig. 3.17 shows the mode 1 results. In 1D one can show that the POD applied to any periodic propagating wave form results in Fourier modes. Here there is a similar result with the x-direction wavelength of the mode essentially equal to the chord length (more easily visible for the v-velocity component). We also see that there is greater change between the $T = 11.25$ and $T = 30$ results. For the mean mode, the L_2 norm of the difference in the velocity between $T = 11.25$ and $T = 30$ was 8×10^{-5} For the first mode, the norm of difference was 7×10^{-3}. Thus, higher modes need a longer time interval to converge.

To further confirm this, Figure 3.18 shows mode 5, which corresponds to the third fluctuating pair. In this case, the x-direction wavelength is about 1/3 the chord length. Especially in the wake for the u-velocity component there are significant changes in the mode calculated with $T = 11.25$ and $T = 30$. This is consistent with the fact that the eigenvalue spectrum has not converged. Although the low index eigenvalues seem to be converged in the eigenvalue plots, one must remember that this is a log scale so it is more difficult to see variations of the eigenvalues for the low index eigenvalues. For the fifth mode, the L_2 norm of the difference in the u or v velocity between $T = 11.25$ and $T = 30$ was 2×10^{-2}.

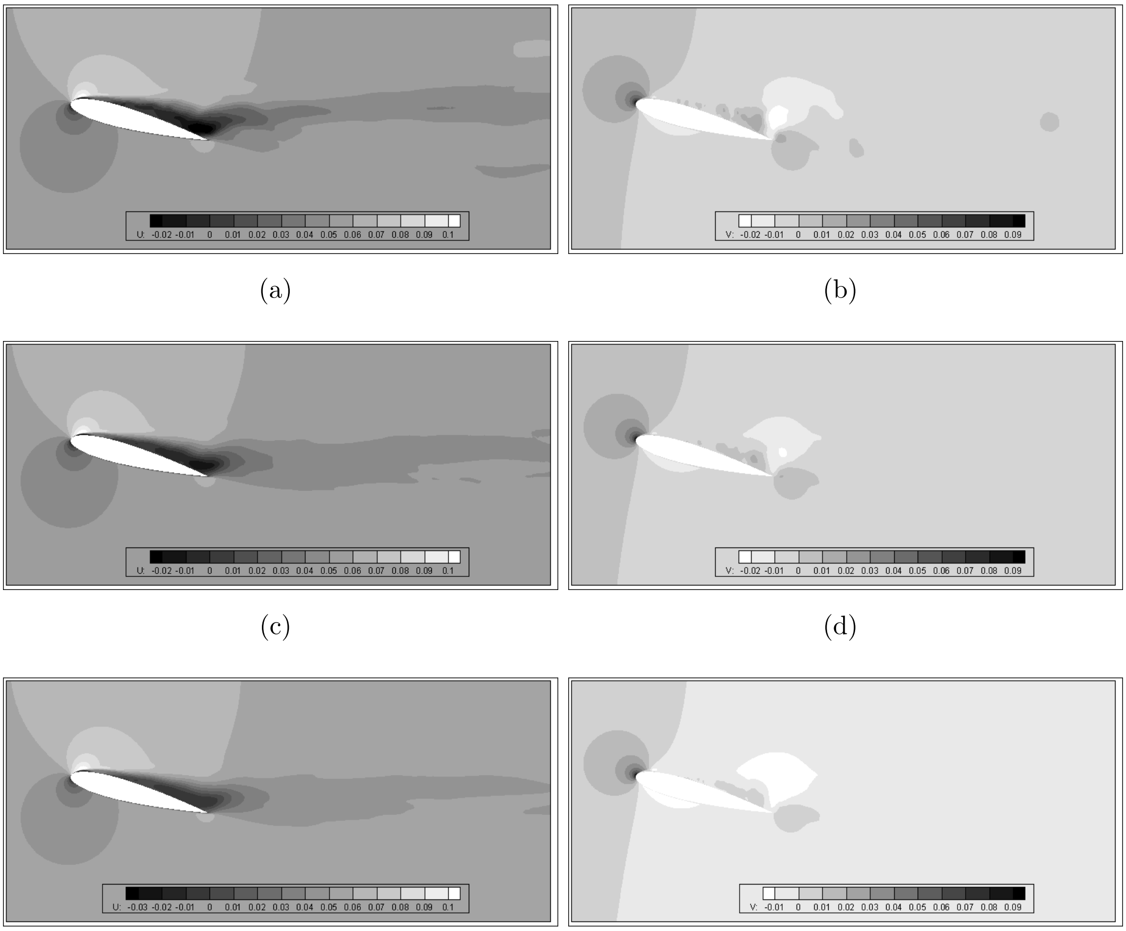

(a) (b)

(c) (d)

(e) (f)

Figure 3.16: Representation of first POD mode (mode 0) of case study 1 for different non-dimensional time windows, (a) and (b) for $T = 3.125$, (c) and (d) for $T = 11.25$, and (e) and (f) for $T = 30$. u velocity POD modes (left) and v velocity POD modes (right).

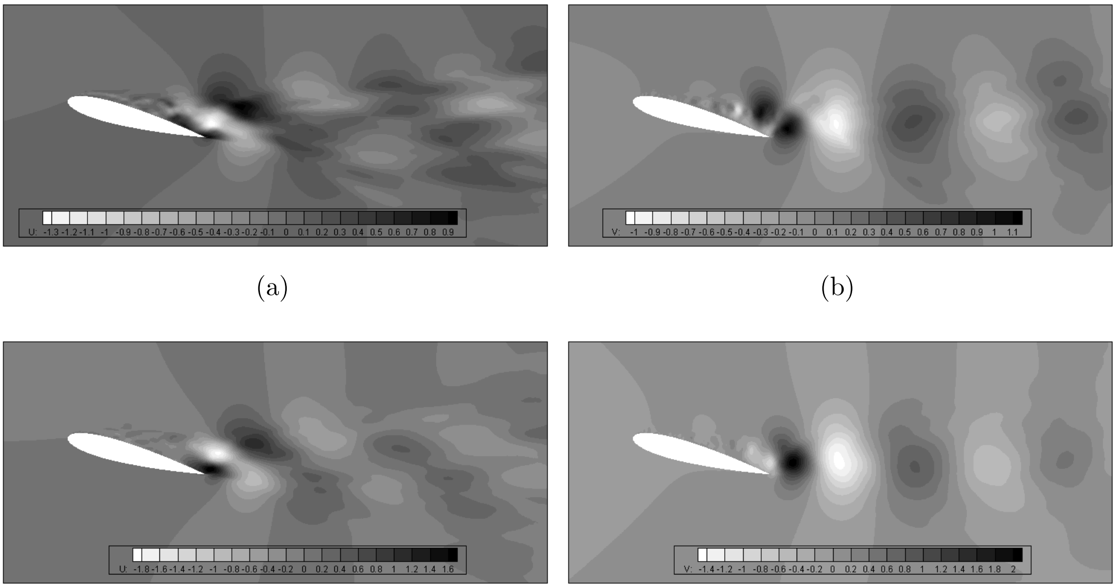

(a) (b)

(c) (d)

Figure 3.17: Representation of second POD mode (first fluctuating mode) of case study 1 for different non-dimensional time windows, (a) and (b) for $T = 11.25$, and (c) and (d) for $T = 30$. u velocity POD modes (left) and v velocity POD modes (right).

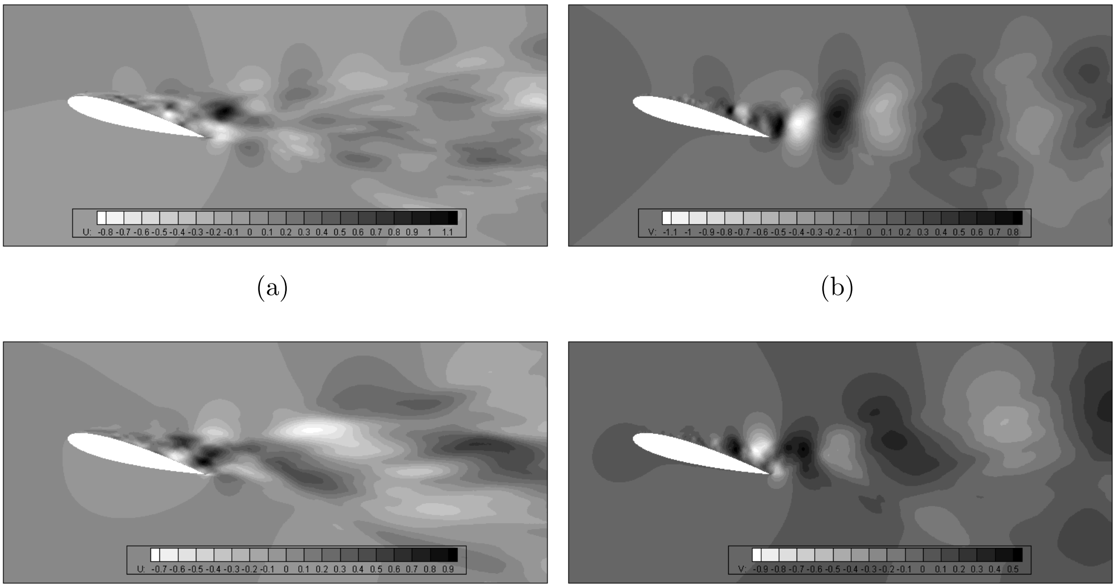

(a) (b)

(c) (d)

Figure 3.18: Representation of sixth POD mode (fifth fluctuating mode) of case study 1 for different non-dimensional time windows, (a) and (b) for $T = 11.25$, and (c) and (d) for $T = 30$. u velocity POD modes (left) and v velocity POD modes (right).

3.6.1.2 Effect of Snapshot Interval

To investigate the second question, we compare the eigenvalues for a fixed non-dimensional time period of 26.25 units, generated with different numbers of snapshots, N_s. The reason for choosing this length is that the total number of time steps in the DNS is 4200, which is divisable by 1 through 8. So, it is possible to generate the POD modes of the same time window using every snapshot, every two snapshots, every three snapshots and so on. As a reminder, for this time interval about 380 modes were needed to capture 99% of the energy as shown in Fig. 3.15.

The eigenvalues are presented in Fig. 3.19. Examining the figure, it appears that the eigenvalues well agree even with $N_s = 525$. Examining the blow-up, one can see that the spectrums created with fewer snapshots deviate from the spectrum with $N_s = 4200$ around eigenvalue 160 although this deviation is probably negligible. In general it seems that for an ergodic flow such as this, a conservative rule of thumb would be to use N_s equal to twice the number of modes needed for a 99% reconstruction. If the samples are truly statistically independent then this should generate a 99% energy reconstruction reliably. If the flow is not ergodic, then one must resolve the smallest time scales of the flow to be sure that all of the flow states get sampled.

3.6.1.3 Effect of Domain Size & Angle of Attack

To understand how domain size and angle of attack affects the eigenvalue spectrums, Table 3.5 shows the number of modes needed to capture 99% of the energy for each of the three cases simulated. In general, the trends in each of the cases is similar with a near linear growth in the number of required modes with domain size. However, the changes in relative modes for each case was not as originally expected. Case study 2, which was the attached flow, actually required the most modes to reach 99% of the energy. The wake behind the NACA 0015 at an angle of attack of 9° is composed of more but smaller vortices compared to the wake at an angle of attack 15°, (fig. 3.20) which has larger stronger structures. So, although

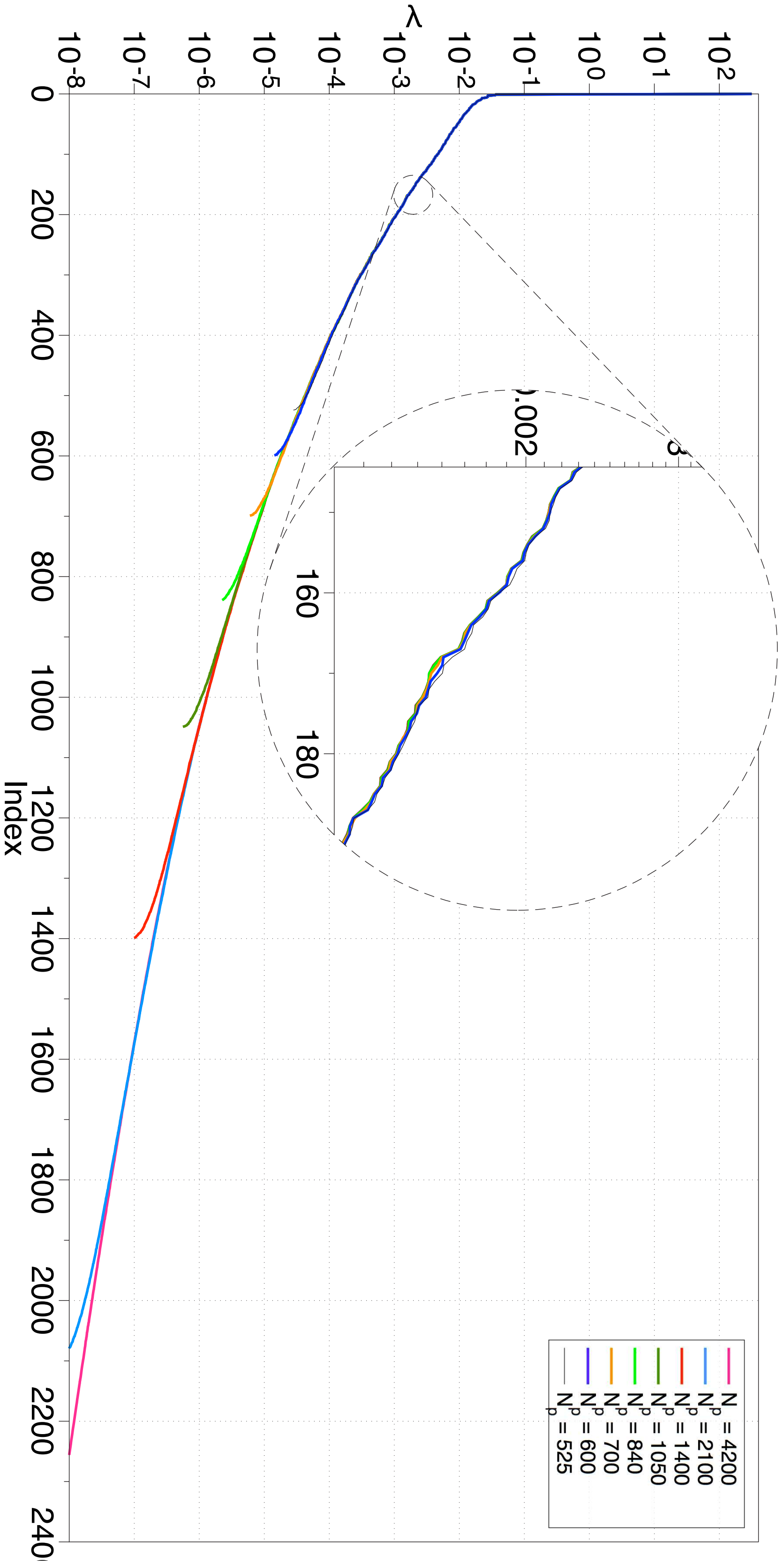

Figure 3.19: POD mode eigenvalues with different N_p for time window 26.25, case study 1.

Table 3.5: Number of fluctuating POD mode needed to capture 99% of energy

T	Time Steps	Case study 1	Case study 2	Case study 3
0.625	100	15	17	17
3.125	500	54	76	68
11.250	1800	175	248	204
20.000	3200	295	422	346
26.250	4200	381	540	435

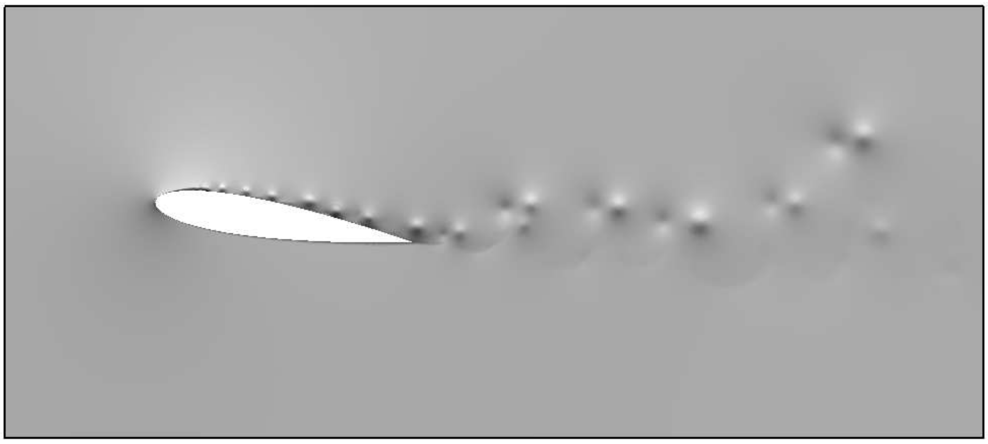

Figure 3.20: Contour of instantaneous u-velocity field from detailed simulation, angle of attck 9°.

the energy carried by each fluctuating mode of a flow at angle of attack 9° is less than for an angle of attack 15°, the energy is more evenly distributed over the modes. For the shorter domain, the number of modes increased, but this is due to the fact that the domain is smaller. The energy captured in the mean mode is less because the area is less and thus it takes more of the fluctuating modes to construct 99% of the energy. As we showed above, the modes are Fourier-like in the wake so the length of the domain does not strongly affect the number of modes needed for an accurate reconstruction.

3.6.2 ROMs

To understand how the mode generation parameters affect the resulting ROM, we test the short and long term behavior of the ROMs generated with different mode sets. For Case 1, four sets of POD modes have been generated using four time windows, those are $T=$ 0.625, 3.125, 6.25 and 11.25 (time steps = 100, 500, 1000 and 1800). For the sake of ease of explanation, we call them time window 1, 2, 3 and 4. For each time window, all of the DNS time steps were used so there is no error induced by using a smaller subset of snapshots. We also investigate how the number of modes included in the ROM affect the results and compare SUPG and Galerkin ROMs.

3.6.2.1 Effect of Time Window

Figs. 3.21 shows the time history of C_D for a ROM having 49 modes where the modes were created used the first two time windows discussed above. The top figure shows only the first 6 time units and the bottom figure shows the full 25 time units of simulation to give a sense of the long term behavior of the models. From the short term behavior, one can see that the ROMs are accurate for the time period that was used to generate the modes. The ROM generated with $T = 0.625$ follows the DNS up to this point but then deviates shortly thereafter. This is also true for the ROM created with $T = 3.125$. Because the flow is chaotic, the model will not follow the DNS for long times, but for a model to be useful the long term statistics should be correct. The plot showing 25 time units, shows that neither model reproduces the correct statistics. Both models eventually decay to a steady-state instead of continuing to fluctuate. Table 3.6 shows the mean and standard deviations of the simulations. The mean of the data is correct, mainly because the mean flow mode is correct, but the long term behavior of the fluctuations leads to essentially a zero standard deviation.

Table 3.6: Mean and standard deviation of simulation of section 3.6.2.1

Term	Mean	Standard deviation
DNS	1.036	0.28
$N_r = 49$, $T = 0.625$	1.028	0.031
$N_r = 49$, $T = 3.125$	1.026	0.066
$N_r = 49$, $T = 6.250$	0.97	0.075
$N_r = 49$, $T = 11.250$	1.109	0.076

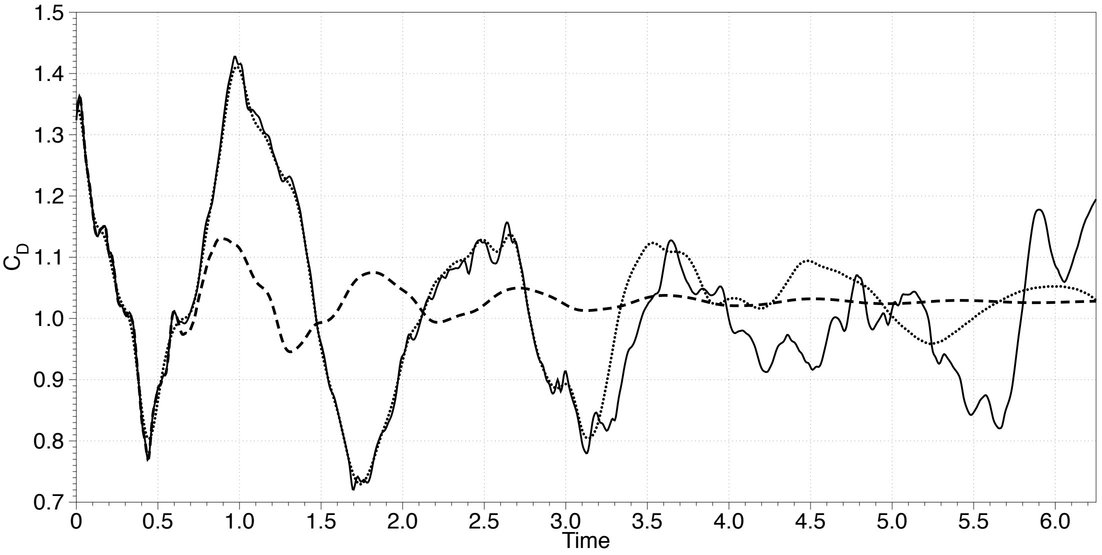

(a) Short term behavior. Length of simulation = 6.25 non-dimensional time units.

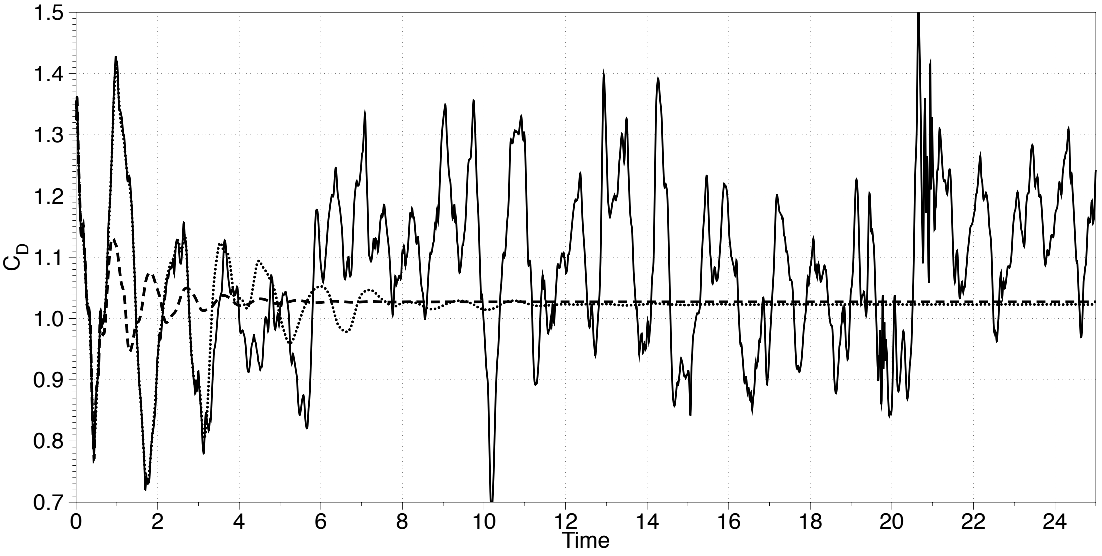

(b) Long term behavior. Length of simulation = 25.0 non-dimensional time units.

Figure 3.21: Case study 1, C_D of detailed simulation (black line), SUPG POD-ROM simulation with $N_r = 49$ for $T = 0.625$ (dashed line), and SUPG POD-ROM simulation with $N_r = 49$ for $T = 3.125$. (dotted line).

Figs. 3.22 shows the time history of C_D for a SUPG ROM with size of 49 modes where the modes were created using the time windows $T = 6.25$ and $T = 11.25$. Again, the top figure shows only the first 6 time units and the bottom figure shows the full 25 time units, long term behavior of the models. Over the short term, the SUPG ROM using the $T = 11.25$ modes did not reproduce the C_D fluctuations as well as SUPG ROM using the $T = 6.25$ modes. This is because there is an inherent tradeoff between the length of the time window used to create the modes and the number of modes needed for the ROM. For longer time windows the number of modes needed for a 99% reconstruction is greater (as shown in Fig. 3.13). These modes are more general, and thus more of them are needed for an accurate prediction. Using 49 of the modes generated with $T = 6.25$, gives a more accurate prediction over the short term. In the long term, neither of the two SUPG ROM simulation give an accurate prediction of the fluctuations. This is also confirmed by the results in Table 3.6 which gives the standard deviations. Thus longer time window modes and an increased number of modes is necessary for long term prediction.

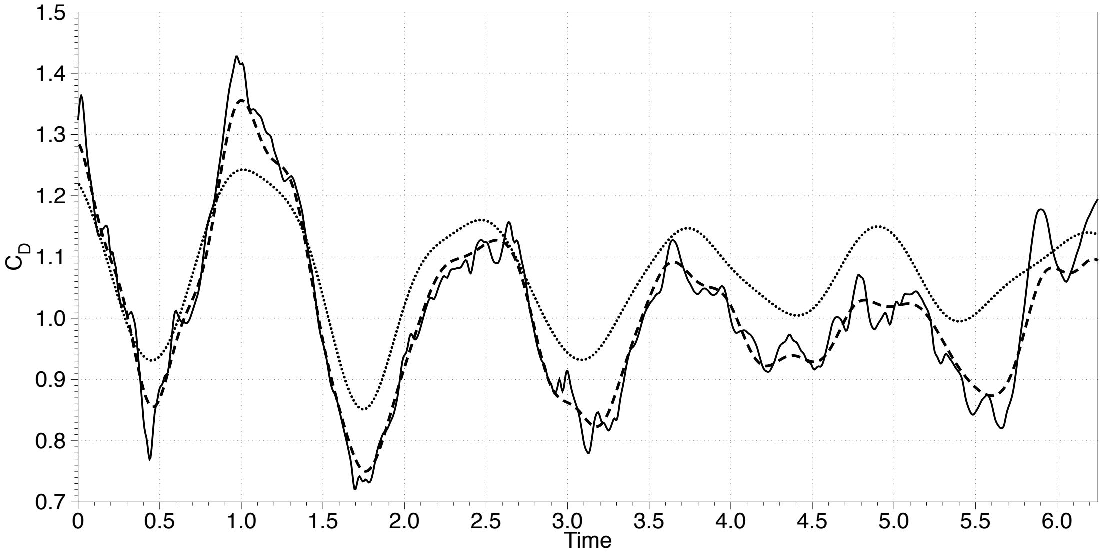

(a) Short term behavior. Length of simulation = 6.25 non-dimensional time units.

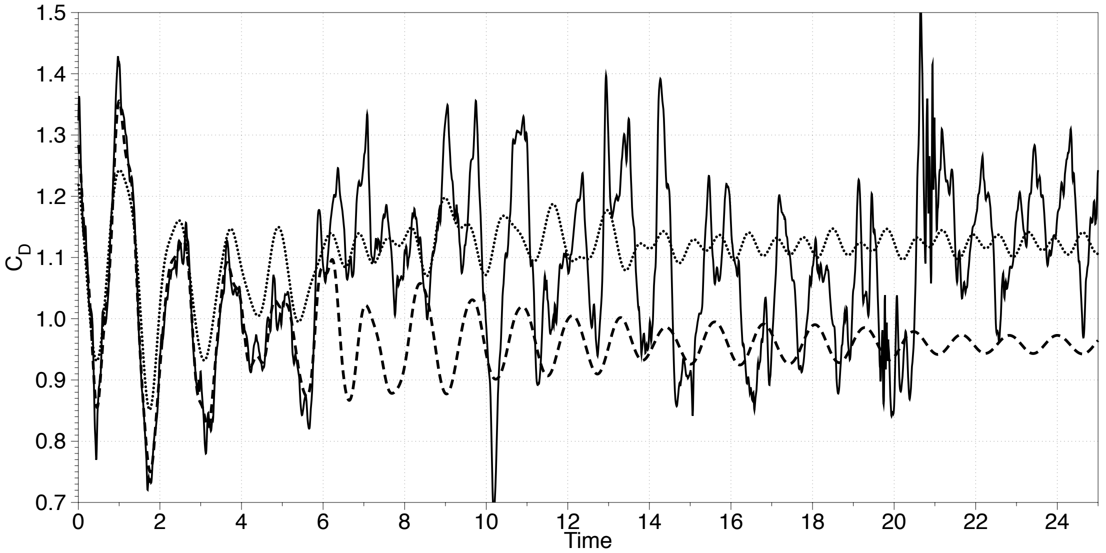

(b) Long term behavior. Length of simulation = 25.0 non-dimensional time units.

Figure 3.22: Case study 1, C_D of detailed simulation (black line), SUPG POD-ROM simulation with $N_r = 49$ for time window 3, $T = 6.25$ (dashed line), and SUPG POD-ROM simulation with $N_r = 49$ for time window 4, $T = 11.25$ (dotted line).

Fig. 3.23, shows a snapshot at $t = 6.25$ of the u-velocity of the detailed solution and the SUPG ROM solution with $N_r = 49$ using the modes created from time window 4. Not surprisingly, in the separation region above airfoil, the reduced order model has difficulty reproducing the fine detail of the small scale structures.

This is also true of the vortices in the wake. These small scale structures are apparently critical for predicting the chaotic behavior of the flow.

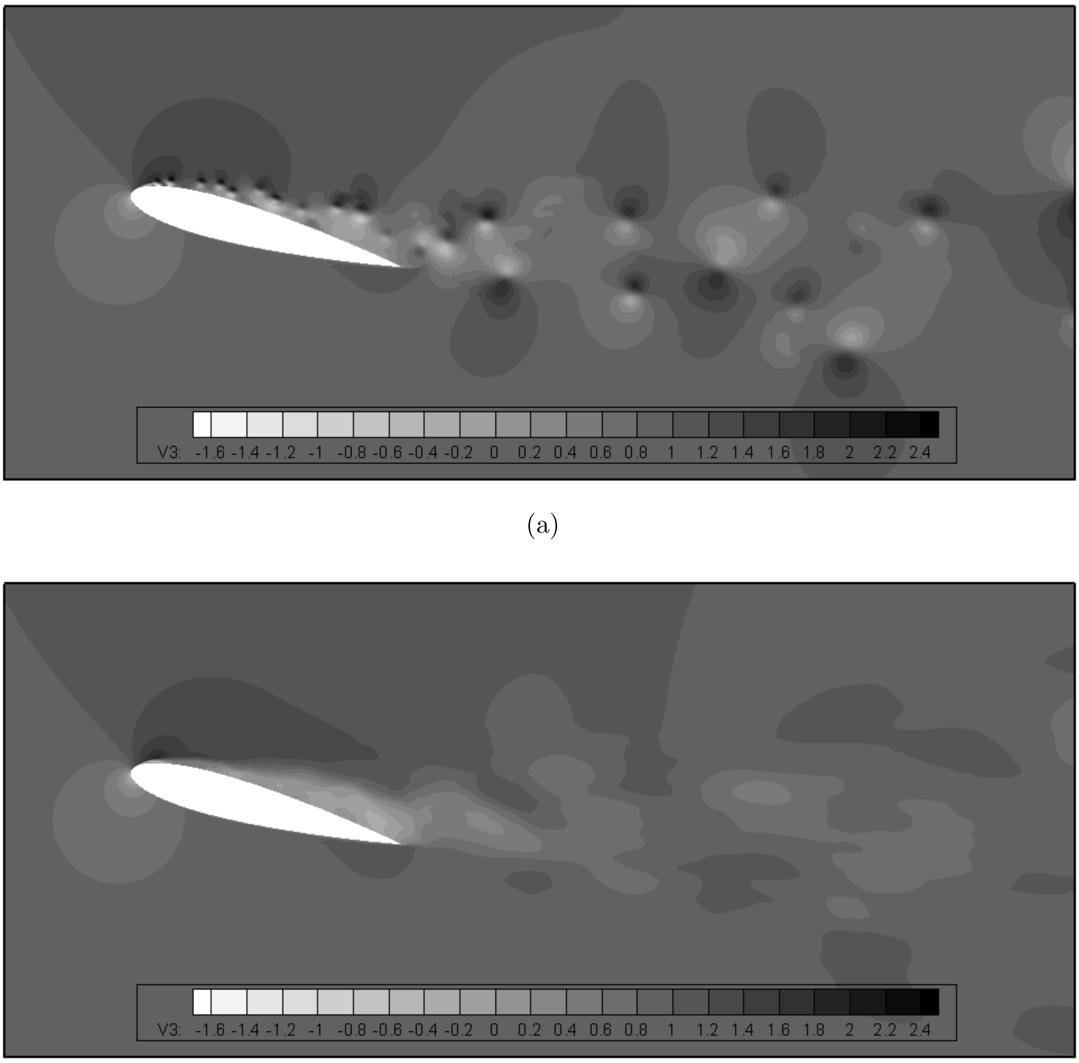

(a)

(b)

Figure 3.23: Contour of u velocity, (a) u_{Detailed} (b) u_{ROM}

3.6.2.2 Effect of Number of Modes

To investigate the effect of N_r on the model predictions, we start by examining the short term predictions. Fig. 3.24 shows the comparison of SUPG ROMs with $N_r = 49$ and $N_r = 29$ for time window 2. With 49 modes the ROM did a good job predicting the short term behavior for time window 2. This remains true even for $N_r = 29$ although some of the small scale fluctuations are missed. For this case, it requires 54 modes to reach 99% of the energy, thus this criteria actually may be over restrictive. Outside of the time window, neither model can predict the behavior and both decay as time goes to infinity. The model with $N_r = 29$ actually decays slower in the long term (not shown) which is difficult to explain.

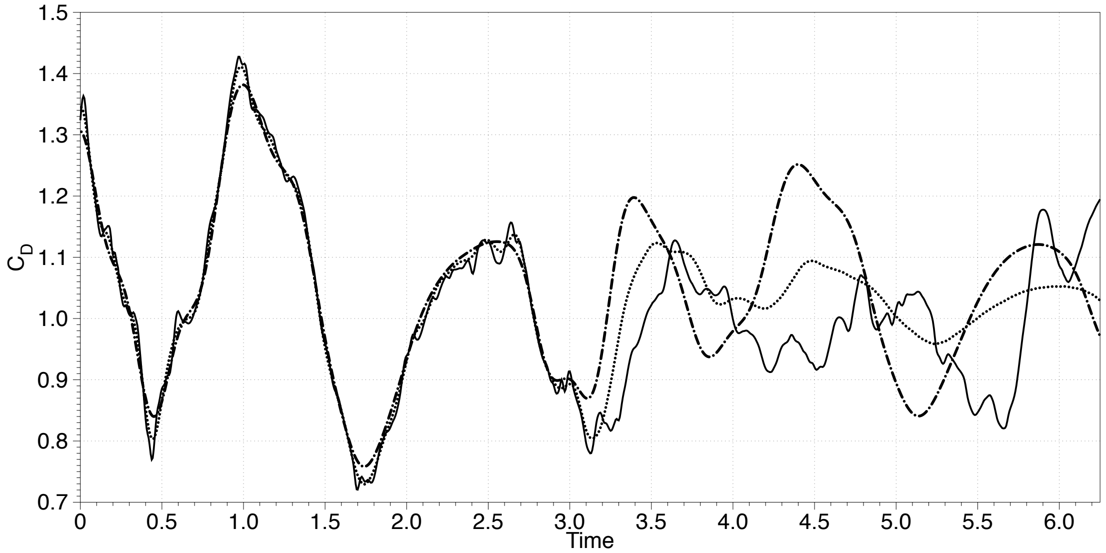

Figure 3.24: Case study 1, C_D of detailed simulation (black line) SUPG POD-ROM simulation with $N_r = 49$ (dashed line) and $N_r = 29$ (dot-dashed line) for time window 2, $T = 3.125$.

Fig. 3.25 shows the comparison of the first 6 time units with $N_r = 89$ and $N_r = 175$ for the modes created from time window 4 ($T = 11.25$). For $N_r = 49$ (Fig. 3.22), the short term prediction was not accurate. Fig. 3.25 shows that the accuracy improves with increasing N_r and that with 175 modes, many of the higher-frequency fluctuation begin to be predicted. For this case, the 99% cut-off is 175 modes so we again see that this is a reasonable value to use to estimate the necessary number of modes for an accurate model prediction. Examining the long term prediction, we again see that even with 175 modes, the long term behavior is not captured properly. In this case however, a limit cycle is predicted by models with both 89 and 175 modes however the amplitude of the fluctuations is significantly under predicted. Overall, one can say from this that the 99% cut-off is a reasonable estimate of the number of modes need for any finite window. However, as we have not been able to predict how many modes are needed to capture 99% of the energy for a infinite time window (Fig. 3.15), it is unclear how many modes would be needed to accurately predict the chaotic behavior of this flow.

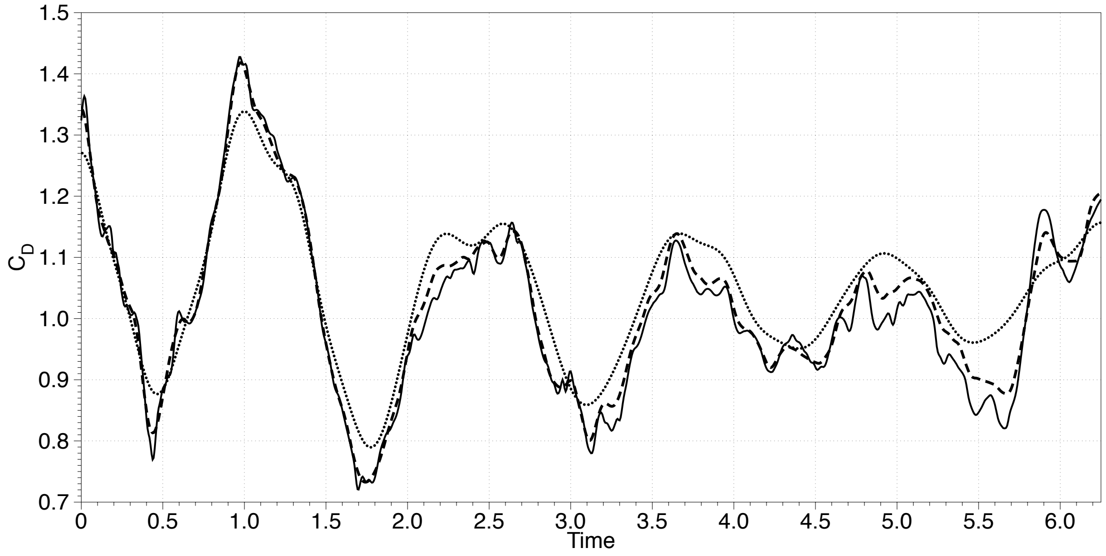

(a) Short term Length of simulation = 6.25 non-dimensional time units.

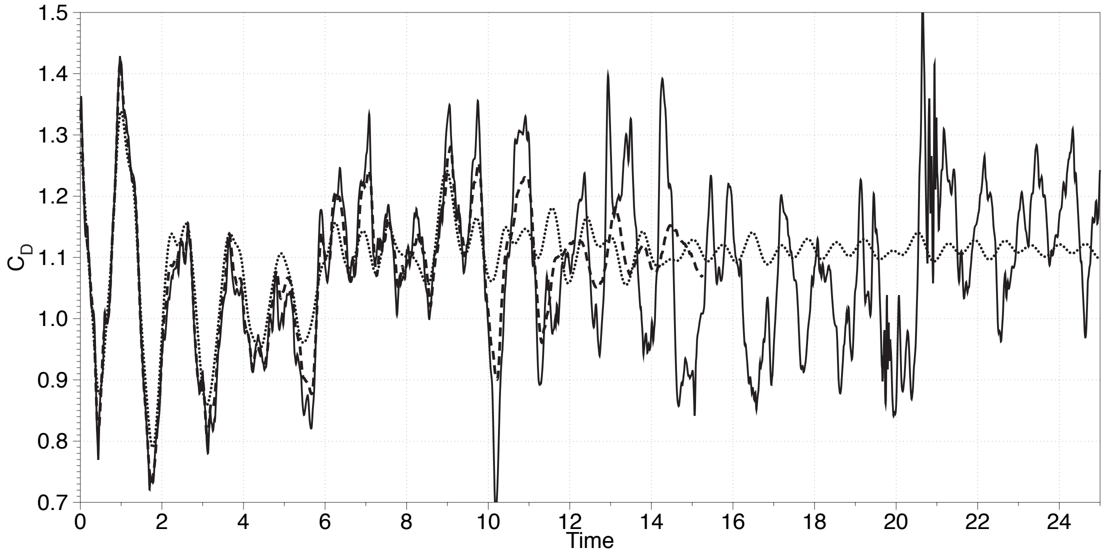

(b) Long term Length of simulation = 25.0 non-dimensional time units.

Figure 3.25: Case study 1, C_D of detailed simulation (black line) SUPG POD-ROM simulation for time windows 4 ($T = 11.25$) with $N_r = 89$ (dotted line) and $N_r = 175$ (dashed line).

3.6.2.3 Effect of Stabilization

In all of the previous results, the SUPG ROM either completely damped the fluctuations or under predicted their magnitude. This may be because of the inherent dissipation in a SUPG stabilization. To investigate this, we compare Galerkin ROM which includes no stabilization and SUPG ROM. Fig. 3.26 shows the simulation of the Case 1 with $N_r = 49$ for both the Galerkin and the SUPG ROM where the modes were made with $T = 3.125$. Again, the top figure shows only the first 6 time units and the bottom figure shows 25 time units. For the most part, both the Galerkin and SUPG ROMs predicted the results within the time window that the modes were generated from although the Galerkin ROM begins to deviate from the DNS before the end of the window (at $t \approx 2.25$). Out side the interval which was used to generate the modes, the amplitude of the fluctuations is not well-predicted by either model. The Galerkin ROM over-predicts (standard deviation = 0.80) the fluctuation amplitude while the SUPG ROM under predicts the amplitude decaying to zero. This is somewhat what one would expect as the SUPG model includes dissipation while the Galerkin model does not and is consistent with what was observed in the low Reynolds number case. The amplitude of Galerkin ROM continues to grow with time, although at a non dimensional time of 25, the simulation did not blow-up.

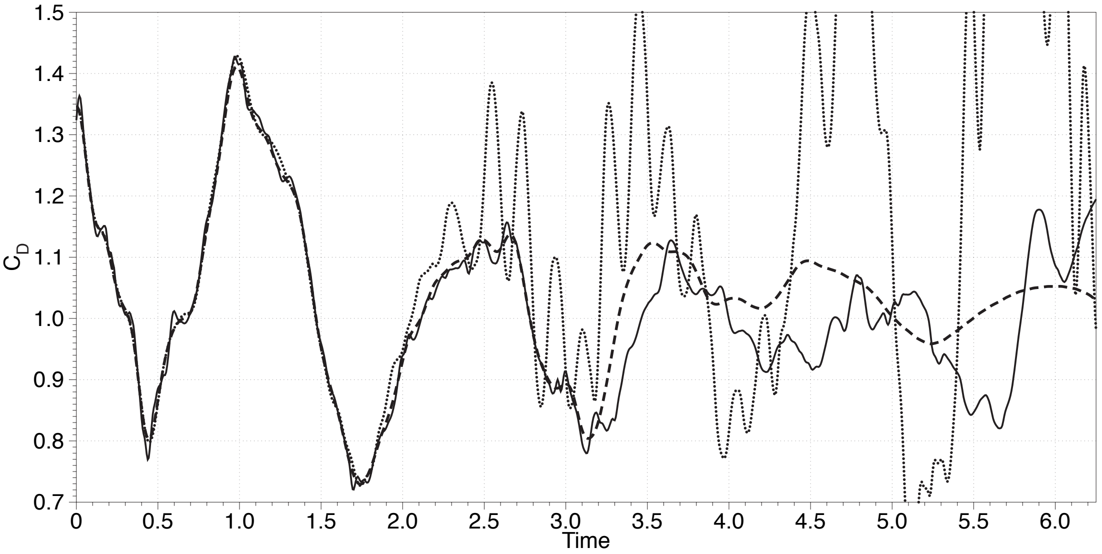

(a)

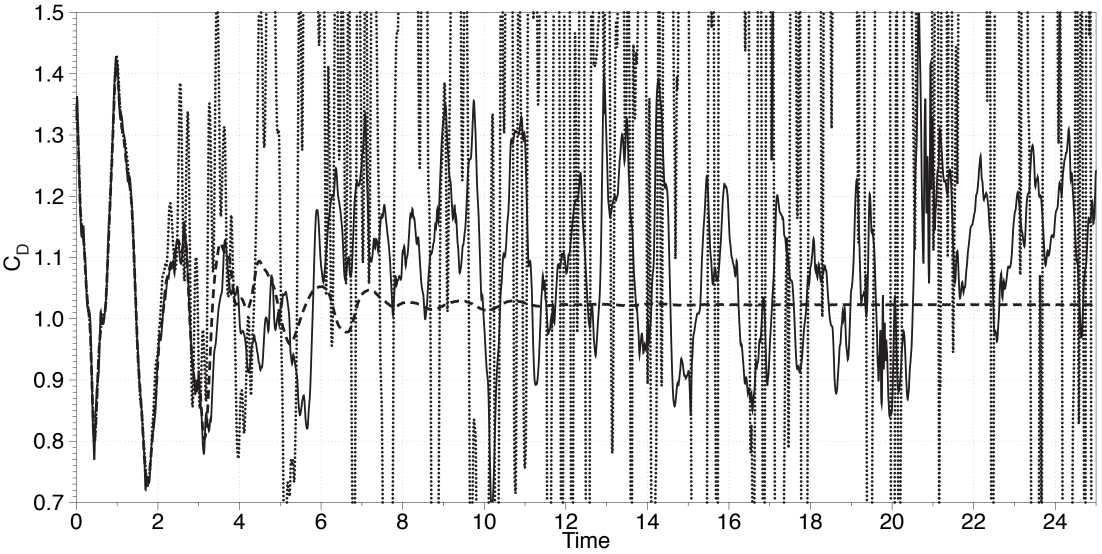

(b)

Figure 3.26: C_D of detailed simulation (black line), SUPG POD-ROM with $N_r = 49$ (dashed line) and Galerkin POD-ROM with $N_r = 49$ (dotted line) from time window 2, $T = 3.125$.

3.6.2.4 Effect of domain size

The last effect investigated is the domain size. With a smaller domain, it was originally thought that a more compact model might be developed, but this conjecture was not supported by the eigenvalue spectrums as shown in Table 3.5. To determine whether domain size affects the ROM, Figure 3.27 shows the SUPG

ROM results with $N_r = 49$ for modes created from time windows 2 and 4. The corresponding results for the larger domain size (Case 1) are shown in Fig. 3.21 and Fig. 3.22. The results obtained for the smaller domain are basically the same as for the larger domain; for the smaller time window modes ($T = 3.125$) the simulations agree well up to the end of the time window, and for the longer time window modes ($T = 11.25$) the short term behavior is not predicted well. The main difference is in the long term behavior of the ROM created using the $T = 11.25$ modes. For the shorter domain, the solution was not damped, but reached a finite amplitude limit cycle. The amplitude of this limit cycle was of the correct magnitude (standard deviation of 0.12) which was the same as the DNS. However, unlike the DNS this limit cycle was periodic and not chaotic. All in all, the size of domain does not have a significant effect on the results for short term simulation; for the same number of modes one obtains the similar accuracy over the short term even though the long term behaviors can be significantly different.

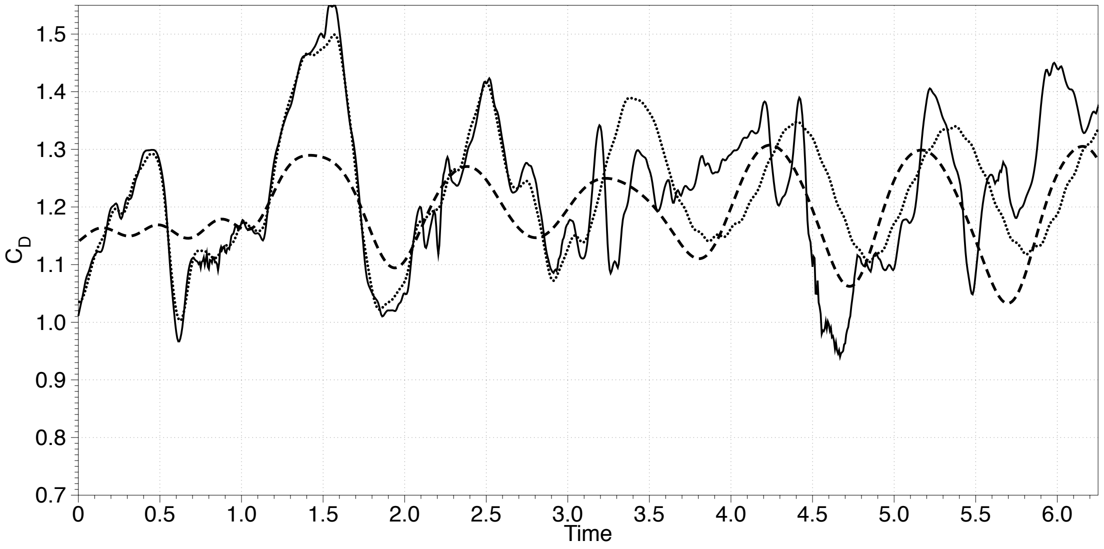

(a) case study 3

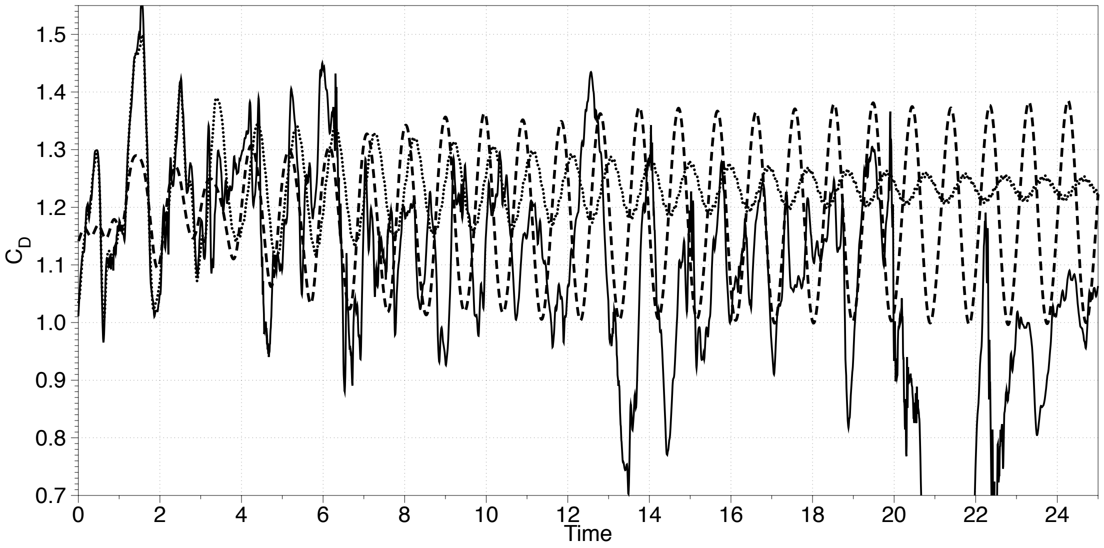

(b) case study 3, time window 2 stdev = 0.065, time window 4 stdev = 0.11

Figure 3.27: C_D of detailed simulation (black line), SUPG POD-ROM, $N_r = 49$, time window 2 (dotted line) and time window 4 (dashed line)

3.7 Conclusions

The accuracy of proper orthogonal decomposition based reduced order models was tested for flow over a NACA0015 airfoil for low and high Reynolds number flows. The main conclusions of this chapter are:

- For the low Reynolds number case ($Re = 1000$ and 12° angle of attack), the streamwise upwind Petrov-Galerkin (SUPG) stabilization and spectral vanishing viscosity (SVV) stabilization were used, and the results were compared to a Galerkin ROM. In this case, the wake flow was periodic and the eigenvalue spectrum indicated that the first 10 modes captured 99% of the flow energy. For the short term prediction (within the time span used to generate the POD modes), all models well predicted the details of the flow when 15 modes were used. However, for the long term prediction of the drag (beyond the original time span), only the SUPG model correctly predicted the limit cycle amplitude.

- The high Reynolds number case was a 2-D flow with Re= 100,000 at angle of attack of 15°. At this Reynolds number, the flow separates and sheds small scale vortices into the wake from both the separation point and from the airfoil trailing edge. The resulting turbulent flow is chaotic with a broad range of temporal and spatial scales. As a result, the energy is distributed over a much larger range of POD modes. For a window of 30 non-dimensional time units, 431 modes captured 99% of the energy. The convergence of the eigenvalue spectrum with respect to the duration of time window from which the modes were derived was investigated and it was found that the number of modes needed to capture 99% of the energy increased almost linearly with the time window. This indicates that to obtain a converged set of POD modes for high Reynolds flows a long time simulation is needed (much longer than 30 chord times).

- The modes of four different time windows with durations of 0.625, 3.125, 6.25 and 11.25 non-dimensional time were used to test the SUPG POD-ROM. It was shown that the SUPG POD ROM reproduced the large scale structures of the flow for the time period that was used to generate the modes but did not produce the correct long-term behavior; none of the models could reproduce the chaotic limit cycle of the DNS. As the length of time window from which the modes was derived was increased, the accuracy of the ROM decreased for a fixed number of modes. This is because of the fact that for a longer time window more modes were needed to capture the same percentage of energy.

- A comparison between SUPG ROM and Galerkin ROM was done. It was shown that the Galerkin ROM also can predict the fluid flow pattern within the part of time window that the modes were extracted. However, the long term simulation of Galerkin ROM showed that the drag oscillation amplitudes increased with time, while the SUPG ROM under predicted the amplitudes.
- Domain size and the angle of attack had minor effects on the derived ROM. The same basic behavior discussed above occurred at an angle of attack of 9° and for a domain sizes of 5 and 10 chord lengths.

Overall, the main conclusion is that generating a ROM for high Reynolds number flows that reproduces the correct limit cycle behavior requires much more modes than has been typically used. These results show that the number of modes required (for this 2D flow) is at the minimum hundreds. If the flow was 3D, additional Fourier-type modes would be needed in the span-wise direction. Thus, although such a model may be significantly smaller than a turbulent DNS, it will certainly not be a compact ROM in the traditional sense.

Chapter 4

Proper Orthogonal Decomposition Based Reduced Order Modeling for Transient Flow

4.1 Introduction

Despite remarkable improvement in computational resources and speed, solving the Navier-Stokes equations for complex flows in real time is still challenging. To overcome this difficulty, one approach that has attracted attention is reduced-order modeling (ROM), which uses specialized basis functions to decrease the number of degrees of freedom necessary to represent the flow. A detailed review of the different ROM techniques was reported in [1]. Among various ROM approaches, the proper orthogonal decomposition reduced order model (POD-ROM) is considered in the present study.

The POD introduces orthogonal basis functions that can optimally capture the energy of the process; they are derived by minimizing the mean-square error of the reconstruction [2]. This makes it possible to reconstruct a process by a linear combination of a limited number of modes. By projecting the governing equations onto a finite number of these POD basis functions and solving the resulting ordinary differential equations (ODEs) for the coefficients of these modes, an accurate approximation of the response of complex systems can be obtained. In fluid mechanics, POD was primarily employed to study the coherent structures of turbulent flow fields [2, 33]. Lumley [2] suggested that coherent eddies in turbulent flows may be associated with the POD modes. Later, Aubry et al. [5] studied the dynamics of coherent structures in a turbulent boundary layer using POD modes. In this approach, the POD modes form the basis used for the flow simulation instead of finite element basis functions. This was the first POD-based reduced order model (POD-ROM) of a fluid flow. This approach, which enables low-cost flow simulations for a particular problem, is of interest in a variety of applications, ranging from optimization to active flow control.

To create ROMs for flow control or ROMs that span a wide range of parameters, one often needs to either apply the POD to large data sets run at a range of conditions or combine the POD modes created from simulations at different conditions. For example, to create POD modes for a controlled flow it has been shown that one needs to generate POD modes that represent both the controlled and uncontrolled flow states [79–82].

Several authors have examined ways to combine POD modes created from individual simulations. Others have just combined all the data onto one long database and performed the POD on that. For instance, Kriegseis et al. [83] performed the POD on a combined database that included various flow conditions. Using this method, which is referred to as “Common Proper Orthogonal Decomposition”, they examined the influence of various parameters. Schmit and Glauser [84] referred to this method as “Global Proper Orthogonal Decomposition” (GPOD) and used it for various Reynolds numbers. They reported that the GPOD properly estimates the wake flow field behind a bluff body. Earlier, Taylor and Glauser [85] found that this approach requires more modes to capture a given percentage of mean-square energy compared to a database created for only a single flow condition. Siegel et al. [86] demonstrated that with GPOD method, transient data can be included to develop modes for transient as well as the pre-transient flow regime. This approach was also used by Ma and Karniadakis [32] to generate a model of 3-D flow past a cylinder. They combined data from Reynolds numbers of 185 and 182 to make a model that correctly predicted the jump in Strouhal number which occurs at a Reynolds number between 182 and 185. The model created using only one Reynolds number failed. Galletti et al. [12] also constructed a database that contained snapshots at different Reynolds numbers. They then used the POD modes of the mixed database to simulate the dynamics of a flow with Reynolds numbers that were not included in the database and found reasonable results for 30 vortex shedding cycles. More recently, Weller et al. [87] used a database including various Reynolds numbers and found that having input data at different conditions is crucial for improving the robustness of the POD-ROM system. A similar approach is Generalized POD where one performs a single simulation but varies the parameters of interest during the simulation. Bergmann et al. [31] used the Generalized POD basis by using snapshots of a range of different states (a chirp signal) in order to successfully represent a flow field which undergoes transient development.

To avoid solving a large eigenvalue problem other authors have examined alternative methods of generating modes. One approach is to add additional mode(s) to the expansion to make the new POD-ROM cover a wider range of flow dynamics. Noack et al. [88] and Siegel et al. [89] found that the error in the mean-flow is the main source of error for the case of periodic low Reynolds number flow behind a cylinder. Noack et al. [88], Gerhard et al. [90] and Siegel et al. [89] added a new "shift-mode" or "mean flow mode" to correct the mean flow. One additional mode means one more degree of freedom and one more equation to solve, but the inclusion of the shift-mode significantly improves the accuracy of the transient dynamics from one state of vortex shedding to another. The shift mode is constructed by subtracting the mean flow and the steady solution. The shift mode is orthogonalized with all other POD modes through a Gram-Schmidt procedure.

A second approach is producing POD modes for various states of the flow and then using a combination of these modes. Christensen et al. [91] created a model for predicting the Hopf bifurcation for a rotating fluid in a cylindrical vessel using POD modes from snapshots taken from several flow states with Reynolds number at both sides of the bifurcation. In this case a union of all the modes was made to generate the ROM. The modes are orthogonalized brfore being used for ROM.

Other researchers used interpolation or extrapolation of POD modes near the operating condition as the third approach. Morzynski et al. [92, 93] interpolated the POD modes to build a continuous mode interpolation procedure between two flow states by interpolation of the corresponding two-point correlation matrices. The direct interpolation of POD modes might not lead to accurate results due to the fact that the interpolation of two orthogonal sets of modes is not guaranteed to be orthogonal [94, 95]. Therefore, “subspace angle interpolation” was introduced [94, 96] to address this problem and alleviate the error for different flow conditions. But subspace angle interpolation loses its accuracy when the mode sets are not similar, in addition to being computationally inefficient [97]. Amsallem and Farhat [95] introduced a novel interpolation and obtained promising results. Hay et al. [47] tried to derive modes from the POD modes of reference states by either extrapolation of the referenced modes in the parameter space or through a first-order expansion using the mode sensitivities. The expanded approach is more accurate but computationally more expensive. In a series of studies Hay et al. [98–100] tested both methods for varying bluff body shapes and different Reynolds numbers and showed the effectiveness of the POD-ROM.

Jrgensen et al. [101] proposed the Sequential Proper Orthogonal Decomposition (SPOD) using different sets of snapshots and yet still producing orthogonal POD modes. This was carried out by projecting each set of old computed POD modes on the new set of snapshots and subtracting the projection from new set of snapshots before calculating the auto-covariance matrix of POD. While the method is reasonable accurate, the truncation of data might lead to errors. Bergmann et al. [70] used another iterative ”Krylov-like” process. A POD-ROM was built using POD modes of an alternative flow regime. Then the POD modes of the residuals are computed and orthogonalized respect to the original POD modes. The new set of POD modes including old and new modes are used for the next iteration.

The same procedure is done at each iteration. They found excellent results for the 1-D Burgers equation, but the procedure converged too slowly for the 2-D Navier-Stokes equations. Inspired by aforementioned mean flow mode or shift mode idea, Siegel et al. [102, 103] introduced the Double Proper Orthogonal Decomposition (DPOD). After computing the POD modes of each parameter state, the POD modes are stored in new sets by rank. That is, the first POD mode of each set goes to first secondary set and so on. Applying POD on the secondary sets leads to the final DPOD modes.

There have been other less frequently used approaches. For example Afanasiev and Hinze [104] use the POD-ROM iteratively for flow control. In this approach, the new set of snapshots was added to the old set at each iteration. This process is continued until the solution is converged. In another attempt [70], the hybrid method that couples the direct numerical simulations and reduced order model simulations was used. During the solution process, the DNS and POD-ROM are performed sequentially to modify the results of POD-ROM and re-actualize the database which is used to generate the modes. Camphouse et al. [73] introduced the Split method which superposes modes derived from simulations of control mechanism with no flow and simulations of the baseline flow with no control actuation. They reported good results for Burgers equation. However, superposition of modes for nonlinear equations is mathematically questionable. Behzad et al. [105] tested the Split method for 2-D Navier-Stokes equation and found considerable lack of accuracy.

None of the above approaches are optimal. In the GPOD and generalized POD cases one obtains the correct POD modes and thus can optimally represent the data, but a large eigenvalue problem must be solved. In the other cases, the eigenvalue problem that must be solved is smaller, but the modes that one obtains are suboptimal. In this work we introduce a new method that gives optimal modes but doesn't require the solution of 1 large eigenvalue problem.

To demonstrate the technique, we focus on developing POD modes for predicting the transformation of a fluid flow from one state of motion to another. 2-D viscous flow around a NACA0015 airfoil at Reynolds number of 1000 was used as the test bed. The actuation on the base flow was imposed by a fluidic jet located on 10% cord length from the leading edge of the airfoil. A case study of constant blowing/suction of fluidic jet is used to transform the flow from one state to another. The accuracy of some popular POD enrichment methods including GPOD, and DPOD are tested. These are compared to our new method called Recursive proper orthogonal decomposition (RPOD). This method not only provides a method for combining different flow states, but also allows the POD to be applied to large data sets more efficiently than a standard POD.

4.2 Detailed Solution

In this section, the simulations that will be used to investigate the various POD approaches are described. The simulations are of a two-dimensional incompressible viscous flow past a NACA0015 airfoil with vortex-shedding.

4.2.1 Problem Description

Let Ω be a two-dimensional region containing a Newtonian incompressible viscous fluid with the boundary Γ. For the simulation, a uniform inflow velocity is prescribed at the left boundary of the domain. A NACA0015 airfoil is located at the center of domain (0,0) with the angle of attack of 9°. The angle of attack is defined as the angle of the chord line of the airfoil and the velocity vector. The radius of domain Ω is 10 times the chord length. The problem is non-dimensionalized using the inlet velocity and the chord length such that when the viscosity, μ, is one, the Reynolds number is also one. Several POD-reduced order models are evaluated and tested for the airfoil in the laminar flow regime with $Re = 1000$. An unstructured triangular mesh in a circular domain is used in all calculations. Fig. 4.1 shows the mesh used for the flow simulation and for evaluation of the corresponding POD. On the right side, an outflow boundary condition is imposed

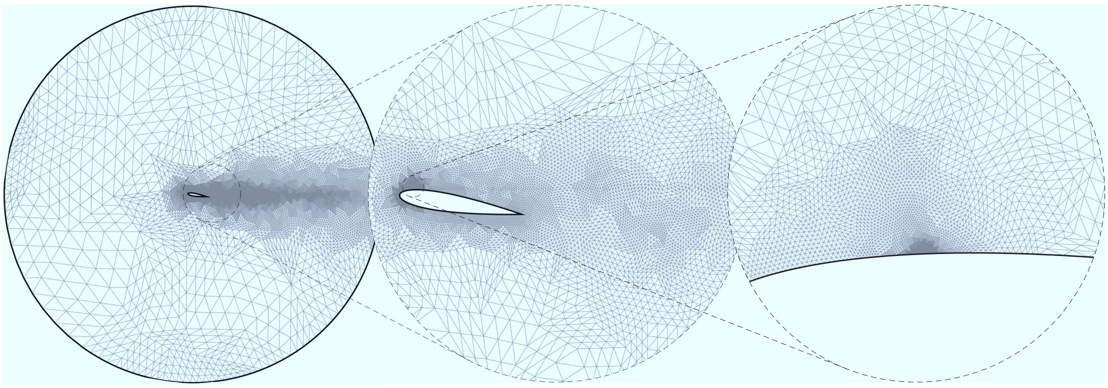

Figure 4.1: *hp*-Finite element mesh, resolved in wake region and high resolved around jet region. ($Re = 1000$, chord length of the NACA0015 airfoil=1; Radious of domain=10.)

where the total stress is set to zero. On the airfoil surface a no-slip boundary conditions is prescribed.

4.2.2 Governing Equations

The governing equations are presented in this section and the numerical procedure for the derivation of the reduced-order models are described in the next section. The equations in curvilinear coordinates are solved using a high-order numerical method. The details of the numerical scheme were described in [63, 106]. The continuity and the Navier-Stokes equations governing the unsteady flow of an incompressible viscous fluid are,

$$\frac{\partial \boldsymbol{w}}{\partial t} + \frac{\partial \mathbf{f}_x}{\partial x} + \frac{\partial \mathbf{f}_y}{\partial y} = \frac{\partial \boldsymbol{\tau}_x}{\partial x} + \frac{\partial \boldsymbol{\tau}_y}{\partial y}, \tag{4.1}$$

with the flow vector

$$\boldsymbol{w} = \begin{bmatrix} \rho \\ \rho u \\ \rho v \end{bmatrix}, \ \mathbf{f}_x = \begin{bmatrix} \rho u \\ \rho u^2 + p \\ \rho v u \end{bmatrix}, \ \mathbf{f}_y = \begin{bmatrix} \rho v \\ \rho u v \\ \rho v^2 + p \end{bmatrix}, \tag{4.2}$$

where u and v are the x- and y-direction velocities respectively and $\boldsymbol{\tau}_x$ and $\boldsymbol{\tau}_y$ are the components of the total stress tensor, given by

$$\boldsymbol{\tau}_x = \mu \begin{bmatrix} 0 \\ 2\partial u/\partial x \\ \partial v/\partial x + \partial u/\partial y \end{bmatrix}, \ \boldsymbol{\tau}_y = \mu \begin{bmatrix} 0 \\ \partial v/\partial x + \partial u/\partial y \\ 2\partial v/\partial y \end{bmatrix}. \tag{4.3}$$

where μ is the dynamic viscosity of the fluid which is assumed to be constant.

4.2.3 Numerical Method

An *hp*-finite element method is employed for performing the numerical simulations [63, 69]. A Petrov-Galerkin variational approach is used to discretize the governing equations on a finite element mesh consisting of triangular elements as shown in Fig. 4.1. On each element, the flow solution is represented using the high order triangular basis developed in [59]. Integration and differentiation operators using this basis can be found in [60]. All calculations were done with the fourth order polynomials which should give 5^{th} order spatial accuracy in the L_2 norm. Both the finite element and the POD-ROM discrete equations are derived using the streamwise-upwind-Petrov-Galerkin variational (SUPG) approach [18]. This is a consistent residual based stabilization method. That is, the test function of the integration is modified relative to the Galerkin approach, but the exact solution still satisfies the weighted integral form. The details of formulation can be found in [63, 69, 106]. The SUPG formulation is stable for convection and viscous dominated flows and also allows equal order polynomials to be used for the pressure and velocity field. A four-stage, index-2, diagonally implicit Runge-Kutta (DIRK) method [61] was used for advancing time in all the flow and POD-ROM simulations. The advantage of this method is its ability to achieve third order accuracy while maintaining A-stability.

4.2.4 Actuator Description

In this study, the flow is actuated through either constant blowing/suction (source or sink jets) or oscillating flow (synthetic jet) placed on the airfoil surface. The jet is modeled by imposing a velocity with the angle of 30° to the airfoil chord line at a location of 10% of the chord length from the leading edge on the top surface. Both a blowing/suction jet and a synthetic jet can changes the mean, the flow fluctuations [29], and the amplitude of the lift and drag forces. Ausseur and Pinier [107] suggested that placing the actuators near the leading edge increases its effect. The mesh is well resolved around the jet position. The jet can be started impulsively or gradually depending on the applications.

4.3 Reduced-Order Modeling Based on a POD Galerkin Approach

4.3.1 Proper Orthogonal Decomposition

The bases for the reduced order models are derived from the detailed data using the proper orthogonal decomposition (POD). The POD was introduced by Lumley [2] as a means to extract the large-scale structures of turbulent flows. It uses data obtained from experiments or numerical simulations to generate an orthogonal set of spatial basis functions. These functions, herein called POD modes, are optimal in terms of energy; the mean square inner product of the solution with a POD mode is maximized. With an adequate number of POD modes, we can approximate any solution as a linear combination of time-dependent weighting coefficients, $a_n(t)$, and the POD modes, $\Phi_n(x)$.

$$\begin{aligned}\boldsymbol{q}(\boldsymbol{x},t) &= \sum_n a_n(t)\boldsymbol{\phi}_n(\boldsymbol{x}) \\ &= \sum_n \left(\boldsymbol{q}(\boldsymbol{x},t),\boldsymbol{\phi}_n(\boldsymbol{x})\right)\boldsymbol{\phi}_n(\boldsymbol{x}).\end{aligned} \tag{4.4}$$

where $(\cdot,\cdot)$ is an inner product.

The POD modes are eigenfunctions of the time-averaged correlation tensor of the flow. mathematically,

$$\int_{\Omega} \boldsymbol{R}(\boldsymbol{x},\boldsymbol{x}')\boldsymbol{\phi}(\boldsymbol{x}')dx' = \int_{\Omega} \langle \boldsymbol{q}(\boldsymbol{x},t)\boldsymbol{q}^{T}(\boldsymbol{x}',t)\rangle \boldsymbol{\phi}(\boldsymbol{x}')d\boldsymbol{x}' = \lambda\boldsymbol{\phi}(\boldsymbol{x}), \tag{4.5}$$

where,

$$\boldsymbol{R}(\boldsymbol{x},\boldsymbol{x}') = \langle \boldsymbol{q}(\boldsymbol{x},t)\boldsymbol{q}^{T}(\boldsymbol{x}',t)\rangle. \tag{4.6}$$

The angled brackets indicate time-averaging and λ represent the mean kinetic energy captured by each mode or eigenfunction. The details of the POD tool can be found in [26, 30, 31, 45, 65]. The discrete form of the (4.5) is applied to the data obtained from numerical simulations. Therefore, the size of the eigenproblem is equal to the number of data points in the mesh times the number of unknowns at each data point (3 - u, v, and p), which makes it difficult to solve this problem. To remedy that, snapshot method of Sirovich [19] has been employed to derive the eigenfunction of the flow. That is an more efficient alternative method for deriving the POD modes for data which is discrete in time. The main idea of this method is to write the POD modes as a linear combination of "snapshots" of the instantaneous flow field. That is,

$$\boldsymbol{\phi}(x) = \sum_{l=1}^{N_s} \boldsymbol{q}(\boldsymbol{x},t_l)\Psi(t_l), \tag{4.7}$$

where the sum is performed over the number of snapshots, N_s. Substituting (4.7) in (4.5), the size of the snapshot method eigenproblem is N_s,

$$\left(\frac{1}{N_s}\int_{\boldsymbol{x}} \boldsymbol{q}(\boldsymbol{x},t_l)\cdot\boldsymbol{q}(\boldsymbol{x},t_k)d\boldsymbol{x}\right)\Psi = \lambda\Psi. \tag{4.8}$$

The snapshot method is computationally more efficient whenever the number of snapshots, N_s, is smaller than the number of solution unknowns.

4.3.2 Low-dimensional Model

The solution for (u, v, p) is sought in the space spanned by a subset of the POD modes, $\boldsymbol{\phi}$. That is the flow field for (u, v, p) can be reconstructed as:

$$\boldsymbol{q}(\boldsymbol{x}, t) = \begin{bmatrix} u(\boldsymbol{x}, t) \\ v(\boldsymbol{x}, t) \\ p(\boldsymbol{x}, t) \end{bmatrix} = \sum_{n=1}^{N_s} a_n(t)\boldsymbol{\phi}_n(\boldsymbol{x}) = \sum_{n=1}^{N_s} a_n(t) \begin{bmatrix} \phi_n^u(\boldsymbol{x}) \\ \phi_n^v(\boldsymbol{x}) \\ \phi_n^p(\boldsymbol{x}) \end{bmatrix}. \tag{4.9}$$

Note that the pressure and velocity modes are considered together which is known as a coupled method. For more information about velocity-pressure ROMs the reader can refer to [108]. Using the POD modes as the trial and test functions in the SUPG weighted integral equations (eq. (3.7)), a system of nonlinear scalar equations for the coefficients a_n are obtained,

$$\mathbf{r}(a_n) = 0. \tag{4.10}$$

That must be solved at each time step. For a finite number of POD modes, N_R, this becomes a reduced order or low dimensional model. The vector of reduced order flow variables would be,

$$\boldsymbol{q}_{\text{ROM}}(\boldsymbol{x}, t) = \begin{bmatrix} u_{\text{ROM}}(\boldsymbol{x}, t) \\ v_{\text{ROM}}(\boldsymbol{x}, t) \\ p_{\text{ROM}}(\boldsymbol{x}, t) \end{bmatrix} = \sum_{n=1}^{N_R} a_n(t)\boldsymbol{\phi}_n(\boldsymbol{x}) = \sum_{n=1}^{N_R} a_n(t) \begin{bmatrix} \phi_n^u(\boldsymbol{x}) \\ \phi_n^v(\boldsymbol{x}) \\ \phi_n^p(\boldsymbol{x}) \end{bmatrix}. \tag{4.11}$$

4.4 Parameter Changes in the Proper Orthogonal Decomposition

In many flow problems, the flow transitions from one mean flow state to another such as would occur when a flow control system is turned on or off or when there is a change in flow parameters such as inlet velocity or angle of attack. To have a predictive ROM, one needs POD modes that can accurately represent not only pre and post parameter change states but also the path of the flow during the parameter change. A brief review of different classes of methods that have been proposed in the literature was given in the introduction (section 4.1). Here, three of the more common methods are explained and compared: Global Proper Orthogonal Decomposition (GPOD) and Double Proper Orthogonal Decomposition (DPOD). We then introduce a novel method of building POD modes that uses a hierarchy of eigen-problems to generate modes. The new method uses the idea of applying POD several times to generate a single set of POD modes from many snapshots. It allows the POD to be applied to large data sets without requiring a equally large eigen-solution and mathematically provides the optimal modes.

4.4.1 Global Proper Orthogonal Decomposition (GPOD)

In the GPOD approach [32, 85, 109] the averaging of the correlation matrix is performed not only over time but also over data sets calculated at many different solution parameters. ROMs created from these POD modes should be able to simulate over a wide range of conditions because the correlation matrix (4.8) is enriched with enough different solutions of the system. A pictorial representation of the GPOD procedure is given in Fig. 4.2. In the figure, N_b is the number of different conditions simulated and N_s is the number of snapshots taken from each simulation. The problem with this approach is that one has a large database composed of $N_b \times N_s$ snapshots which could make the eigenvalue problem (eq. (4.8)) unmanageable.

4.4.2 Double Proper Orthogonal Decomposition (DPOD)

Siegel et al. [102, 103] introduced Double Proper Orthogonal Decomposition (DPOD) method in which the POD is applied twice to generate modes. Fig. 4.3 gives a pictorial representation. In this case, simulations are run at N_b parameter conditions and the POD is first applied to each simulation individually (an eigenvalue problem of size N_s). The POD is then applied again to each set of i^{th} POD modes

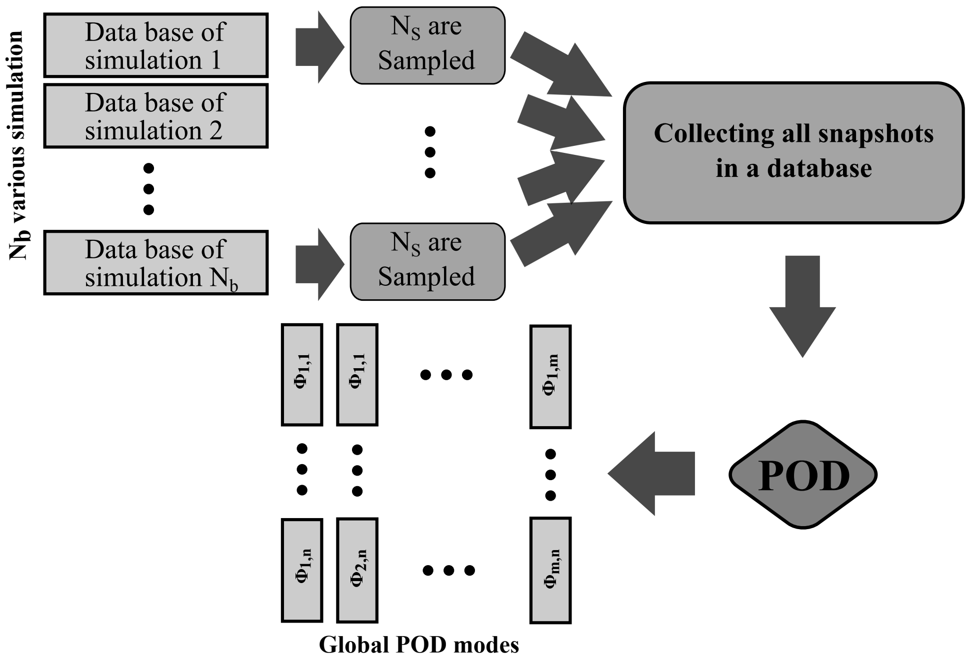

Figure 4.2: Pictorial representation of the GPOD procedure.

as shown by the dashed circle around each set of modes in the figure up for i up to some cut-off value M_1 (M_1 eigenvalue problems of size N_b). This then results in M_1 sets of POD modes for each i. One then chooses the number of modes to keep from each set, M_2. If orthogonal modes are required, then an orthogonalization procedure must be applied to the sets. The general idea is that each set will contain the primary mode (first, second, third, etc.) plus the shift modes needed for transient conditions. This method avoids having to solve one large POD problem.

In the following we implement a somewhat simpler version of DPOD where we again apply POD to each simulation and decide how many modes to keep from each simulation, M_1. Rather than applying POD individually to the N_b sets of modes we then apply POD to all the kept modes together. This results in an orthogonal set of N_b by M_1 modes. We can then select how many modes to use from this final POD for the ROM. This approach does not individually identify primary and "shift" modes, but should give similar ROM results while avoiding having to perform a Gram-Schmidt orthogonalization procedure. In the following we denote these results as MPOD for Modified DPOD. Note that this method does still reduce the size of the final eigenvalue problem to size $N_b \times M_1$ and thus

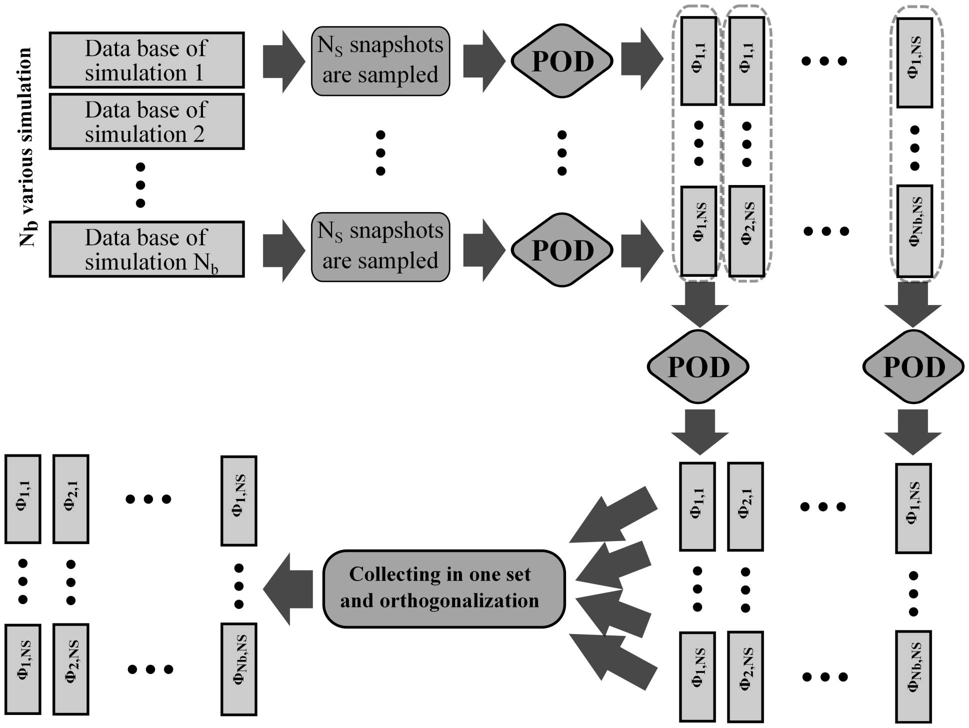

Figure 4.3: Pictorial representation of the DPOD procedure.

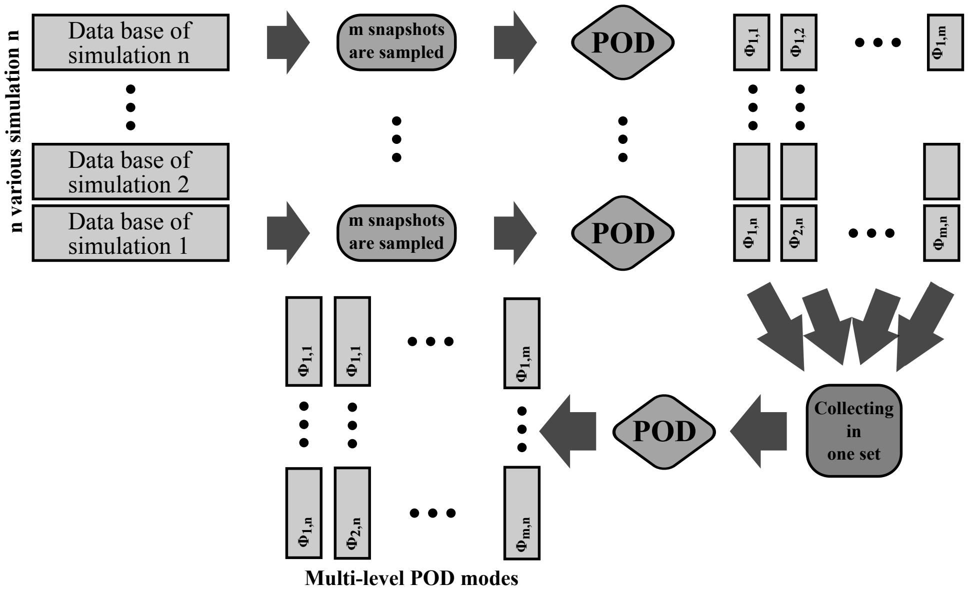

Figure 4.4: Pictorial representation of the MPOD procedure.

is more easily applied to large data sets. A pictorial representation of the MPOD procedure is given in Fig. 4.4.

4.4.3 Recursive Proper Orthogonal Decomposition (RPOD)

Although, DPOD reduces the size of the eigenvalue problems that need to be solved, there are assumptions inherent in the process that may not be correct. In the second application of the POD, it is implicitly assumed that each of the i^{th} modes from the first level POD should be weighted equally. However, the reference flows might have different eigenvalue spectrums, and one flows i^{th} mode might be much more important than another. To remedy this, we introduce the Recursive Proper Orthogonal Decomposition (RPOD). This approach weights each mode appropriately and gives *identically* the same modes as a GPOD, however it only requires eigenvalues of size N_s to be solved, not $N_s \times N_b$.

Suppose that we have N_b simulations each of which has N_s snapshots, applying the POD to each group of snapshots, N_b sets of modes will be generated. The snapshots for any simulation can then be reconstructed as

$$\boldsymbol{q}^{(i)}(\boldsymbol{x},t) = \sum_{n=1}^{N_s} a_n^{(i)}(t)\boldsymbol{\phi}_n^{(i)}(\boldsymbol{x}) \tag{4.12}$$

where the superscript (i) indicates the i^{th} simulation. Subsituting (4.12) in (4.5) gives

$$\frac{1}{\sum_{i=1}^{N_b} t_i}\int_{\boldsymbol{x}'}\left(\sum_{i=1}^{N_b}\int_0^{t_i}\left(\sum_{j=1}^{N_s} a_j^{(i)}(t)\boldsymbol{\phi}_j^{(i)}(\boldsymbol{x})\right),\left(\sum_{k=1}^{N_s} a_k^{(i)}(t)\boldsymbol{\phi}_k^{(i)}(\boldsymbol{x}')\right)\right)dt\boldsymbol{\Phi}(\boldsymbol{x}')d\boldsymbol{x}' = \Lambda\boldsymbol{\Phi}(\boldsymbol{x}) \tag{4.13}$$

t_i is the length of i^{th} simulation. Gathering terms this can be rewritten as

$$\frac{1}{\sum_{i=1}^{N_b} t_i}\int_{\boldsymbol{x}'}\left(\sum_{i=1}^{N_b}\sum_{j=1}^{N_s}\sum_{k=1}^{N_s}\left(\int_0^{t_i} a_j^{(i)}(t)a_k^{(i)}(t)dt\right)\left(\boldsymbol{\phi}_j^{(i)}(\boldsymbol{x})\boldsymbol{\phi}_k^{(i)}(\boldsymbol{x}')\right)\right)\boldsymbol{\Phi}(\boldsymbol{x}')d\boldsymbol{x}' = \Lambda\boldsymbol{\Phi}(\boldsymbol{x}). \tag{4.14}$$

One can show that the POD coefficients satisfy $\int a_j a_k = \lambda_j \delta_{j,k}$ [31] where $\delta_{j,k}$ is the Kronecker delta function. This then gives

$$\int_{\boldsymbol{x}'} \left(\sum_{i=1}^{N_b} \left(\sum_{j=1}^{N_s} \lambda_j^{(i)} \boldsymbol{\phi}_j^{(i)}(\boldsymbol{x}) \boldsymbol{\phi}_j^{(i)}(\boldsymbol{x}') \right) \right) \boldsymbol{\Phi}(\boldsymbol{x}') d\boldsymbol{x}' = \Lambda \boldsymbol{\Phi}(\boldsymbol{x}). \tag{4.15}$$

This is again an eigenvalue problem similar to eq. (4.5), except here the two-point correlation tensor is replaced by a weighted expression combining the POD modes from each of the N_b simulations. This shows that the two point correlation tensor that would be obtained from the GPOD approach (averaging over N_b simulations and N_s snapshots) is exactly the same as the two point correlation tensor that one obtains by using a weighted average over the modes from each simulation where the weights are the eigenvalues.

To take this one step further, we can apply the "snapshot" POD approach to solve the above eigenvalue problem. The main idea is to write the global POD modes as a linear combination of the POD modes from the individual simulations. That is,

$$\boldsymbol{\Phi}(\boldsymbol{x}) = \sum_{i=1}^{N_b} \sum_{j=1}^{N_s} \boldsymbol{\phi}_j^{(i)}(\boldsymbol{x}) \Psi_{ij}, \tag{4.16}$$

Substituting in (4.15),

$$\int_{\boldsymbol{x}'} \left(\sum_{i=1}^{N_b} \sum_{j=1}^{N_s} \lambda_j^{(i)} \boldsymbol{\phi}_j^{(i)}(\boldsymbol{x}) \boldsymbol{\phi}_j^{(i)}(\boldsymbol{x}') \right) \left(\sum_{k=1}^{N_b} \sum_{l=1}^{N_s} \boldsymbol{\phi}_l^{(k)}(\boldsymbol{x}') \Psi_{kl} \right) d\boldsymbol{x}' = \Lambda \sum_{i=1}^{N_b} \sum_{j=1}^{N_s} \boldsymbol{\phi}_j^{(i)}(\boldsymbol{x}) \Psi_{ij}. \tag{4.17}$$

where Λ is the eigenvalue of the global POD problem. This can be rearranged as

$$\left(\sum_{i=1}^{N_b} \sum_{j=1}^{N_s} \lambda_j^{(i)} \boldsymbol{\phi}_j^{(i)}(\boldsymbol{x}) \sum_{k=1}^{N_b} \sum_{l=1}^{N_s} \left(\int_{\boldsymbol{x}'} \boldsymbol{\phi}_j^{(i)}(\boldsymbol{x}') \boldsymbol{\phi}_l^{(k)}(\boldsymbol{x}') d\boldsymbol{x}' \Psi_{kl} \right) \right) = \Lambda \sum_{i=1}^{N_b} \sum_{j=1}^{N_s} \boldsymbol{\phi}_j^{(i)}(\boldsymbol{x}) \Psi_{ij}. \tag{4.18}$$

Bringing the right hand side over and factoring out the common factor of $\phi_j^{(i)}(x)$ gives

$$\sum_{i=1}^{N_b}\sum_{j=1}^{N_s}\boldsymbol{\phi}_j^{(i)}(\boldsymbol{x})\left(\lambda_j^i\sum_{k=1}^{N_b}\sum_{l=1}^{N_s}\left(\int_{\boldsymbol{x}'}\boldsymbol{\phi}_j^{(i)}(\boldsymbol{x}')\boldsymbol{\phi}_l^{(k)}(\boldsymbol{x}')d\boldsymbol{x}'\Psi_{kl}\right)-\Lambda\Psi_{ij}\right)=0. \quad (4.19)$$

This equation can be satisfied by solving

$$\lambda_j^i\sum_{k=1}^{N_b}\sum_{l=1}^{N_s}\left(\int_{\boldsymbol{x}'}\boldsymbol{\phi}_j^{(i)}(\boldsymbol{x}')\boldsymbol{\phi}_l^{(k)}(\boldsymbol{x}')d\boldsymbol{x}'\Psi_{kl}\right)=\Lambda\Psi_{ij}. \quad (4.20)$$

If the i, j indices are converted into a single index system, (i.e. $I = N_s(i-1)+j$) This can be written as a standard eigenvalue problem

$$DC\Psi = \Lambda\Psi, \quad (4.21)$$

in which D is the diagonal matrix of eigenvalues, $\lambda_j^{(i)}$, and C is the inner product of all the POD modes i.e.

$$C_{ij,kl} = \int_{\boldsymbol{x}'}\boldsymbol{\phi}_j^{(i)}(\boldsymbol{x}')\boldsymbol{\phi}_l^{(k)}(\boldsymbol{x}')d\boldsymbol{x}'$$

At first glance, this does not seem to be an improvement over the GPOD approach as it is still dimension $N_b \times N_s$ modes, but one does not need to keep every POD mode from the original decompositions. If one truncates the number of POD modes used from the first decomposition to M modes, then the size of the final eigenvalue problem is only $N_b \times M$. One can determine M by examining the eigenvalue spectrum of the first decompositions, thus this approach allows a systematic way to reduce the size of the eigenvalue problem needed to obtain global POD modes. It also offers a systematic way to combine the modes generated from two different POD decompositions without requiring a Gram-Schmidt orthogonalization procedure. Although, we explained a two-level RPOD, this approach could be applied in a recursive manner at each level keeping only modes with eigenvalues above a specified energy threshold.

4.5 Results

In this section, we compare the various methods by investigating a 2D flow over an airfoil NACA0015 in laminar regime (Re = 1000). The flow is actuated through constant blowing/suction (source or sink of mass) with varying values. The actuator's flow has the angle of 30° respect to the airfoil chord line at a location 10% of the chord length from the leading edge on the top surface. The angle of attack is 9°. All of the parameters are nondimensionalized respect to far-field velocity, u_∞ and chord length. The same numerical set up has been tested for detailed and POD-ROM simulation of a periodic flow in section 3.5 successfully.

For this work, only transient cases are considered; the simulations start with no actuation. After 2 periodic vortex shedding cycles, the fluidic actuator is turned on. During 5 nondimensionalized time units the power of the actuator is increased from zero to a specified value, the magnitude of constant steady blowing/suction. This change affects the coherent structures appearing in the flow. It causes the periodic state of flow to shift from one amplitude to another one. Suction decreases the drag force and increases the lift force. Blowing on the fluidic actuator has the opposite effect. Each detailed simulation includes 1100 snapshots from the initial periodic state to the final periodic state. Six different amplitudes ($-1.5u_\infty$, $-u_\infty$, $-u_\infty/2$, $u_\infty/2$, u_∞, and $1.5u_\infty$) are imposed on the actuator. Therefore, the whole database includes 6600 snapshots (6×1100). This is not unreasonably large, but as we showed in the previous chapter if the flow was turbulent a much larger database would be needed. This simple problem is sufficient to demonstrate the advantages of the our new technique.

4.5.1 RPOD Versus GPOD

If the POD is applied on all the snapshots in the database, the ROM using the resultant modes provides an accurate representation of the flow but the eigenproblem is large. Here we demonstrate that the RPOD can provide comparable results while reducing the size of the eigenvalue problem that one must solve.

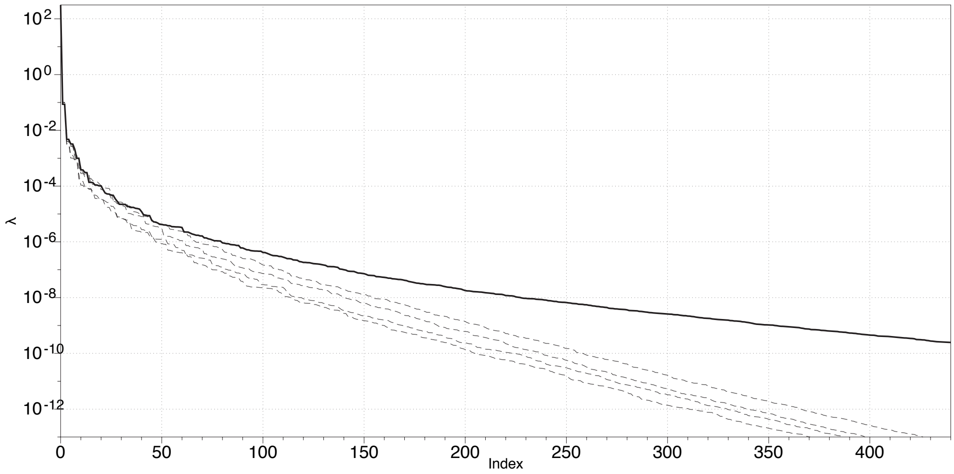

Figure 4.5: Eigenvalues of POD using all snapshots (solid line), eigenvalues of four detailed simulations (dashed line).

To study RPOD, first we look at the eigenvalues. Four detailed simulations with actuation magnitudes of $-u_\infty$, $-1/2u_\infty$, $1/2u_\infty$, and u_∞ are performed. So the whole data base is composed of $4 \times 1100 = 4400$ snapshots. In applying the POD to each simulation individually, four eigenvalue spectra are produced. Fig. 4.5 shows the eigenvalues of each detailed simulation and the POD of all the snapshots together (GPOD). One can see that there is information in each simulation that is not contained in the other simulations because the GPOD spectrum converges slower than each simulation individually.

In the second step of RPOD, we weight each of the modes as discussed in section 4.4.3 and perform an additional POD. Depending on the number of modes kept from the first POD, this should reproduce the GPOD spectrum. Fig. 4.6 shows the GPOD spectrum versus RPOD spectra created with different mode truncations $M = 50, 75, 100$, and 110. As the cut-off mode number is increased, the spectrum converges toward POD of all snapshots. The deviation between the full spectrum and the RPOD spectrums can be predicted by examining the cut-off energy of the initial POD. For example, for a cut-off of $M = 50$, the cut-off energy of the individual N_b spectra are at about $\lambda = 10^{-6}$. This the level at which the final RPOD spectrum deviates from the GPOD spectrum. This also holds fairly well for the other cut-off levels so if one knows what tolerance one requires in reproducing the GPOD results, it is straightforward to decide how many modes

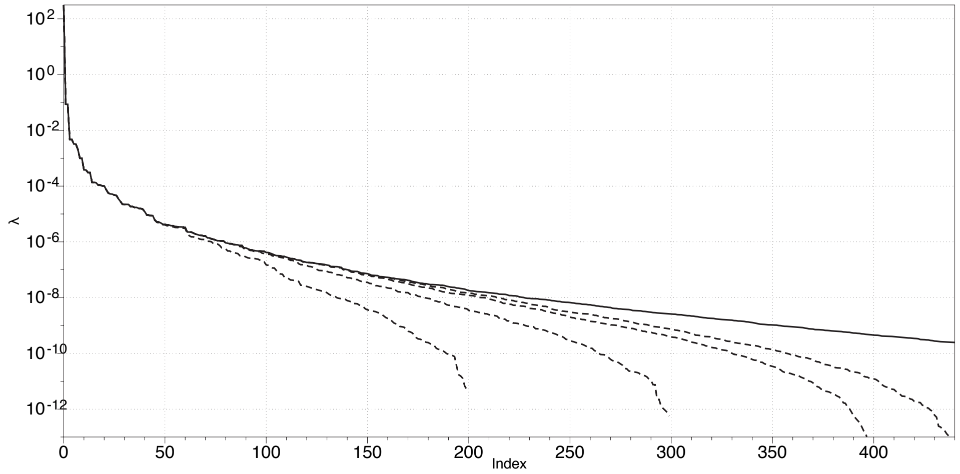

Figure 4.6: Eigenvalues of POD using all snapshots (solid line), eigenvalues of RPODs with cut-off $M = 50$, 75, 100, and 110 (dashed line).

to keep from the first level of the RPOD. Also note that for $M = 110$, the size of the final eigenvalue problem for the RPOD is a factor of 10 smaller than the full eigenvalue of problem.

An alternative method that is often used to reduce the size of the eigenvalue problem for GPOD is to use a reduced set of snapshots. Fig. 4.7 shows a comparison of the eigenvalues of the full GPOD to GPODs performed using a reduced number of snapshots, $N_s = 55$ and 110. This is also compared to RPOD with $M = 55$ and 110. One can see that for this particular case, simply reducing the number of snapshots still reproduces the eigenvalue spectrum reasonably well, but the RPOD does a better job for the same size of the final eigenvalue problem. Furthermore, the RPOD is a more controlled approach in that one can use the initial POD decomposition to determine how many modes are necessary for the second POD decomposition whereas one must arbitrarily choose a reduced snapshot size with no a-priori insight on what amount of reduction is acceptable.

In order to investigate the ROM from RPOD and GPOD, two different cases are considered:

- Case RPOD: POD is applied on 550 snapshots of detailed simulations of six actuation amplitudes, $-1.5u_\infty$, $-u_\infty$, $-u_\infty/2$, $u_\infty/2$, u_∞, and $1.5u_\infty$. So six eigenproblems with dimension 500 are solved and 6×550 POD modes are

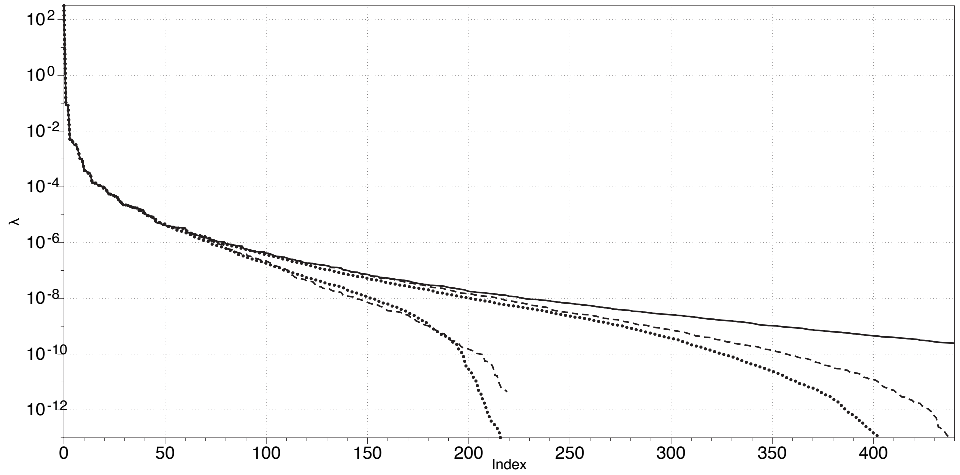

Figure 4.7: Eigenvalues of POD using all snapshots (solid line), eigenvalues of GPOD using $N_s = 220$ and 440 (dotted line) and, RPOD using cut-off number of $N_{cut-off} = 55$ and 110 (dashed line).

derived. 200 energetic POD modes are sampled from each set of modes for the second level of RPOD approach. It would lead to an eigenproblem with size 1200. Note that to do the RPOD, we need 200 eigenvalues of primary POD level.

- Case GPOD: 400 snapshots, uniformly distributed over each of 6 detailed simulation with actuation magnitude of $-1.5u_\infty$, $-u_\infty$, $-1/2u_\infty$, $1/2u_\infty$, u_∞, and $1.5u_\infty$ are sampled to construct temporal tensor (4.8). The dimension of the eigenproblem becomes $6 \times 400 = 2400$.

19 modes of the final RPOD modes are used to perform the POD-ROMs. Results, showed in Fig. 4.8, are close to the detailed simulation. In fact, the results of ROMs using GPOD and RPOD are on each other. It shows that GPOD could be powerful if enough snapshots are sampled. Also, it shows that weighting process is crucial in a muti-level POD to achieve right set of POD modes. RPOD can perform as accurate as GPOD while it needs to solve smaller size of eigenproblems. This capability of RPOD becomes more important when the method is supposed to be used for non-periodic flows. Note that the first level of eigenproblems can be solve parallelly. It means that instead of solving a giant eigenproblem once, it solve some smaller eigenproblems, most of them can be solved at the same time. So, RPOD make it possible that through manageable sizes of eigenproblems, optimal

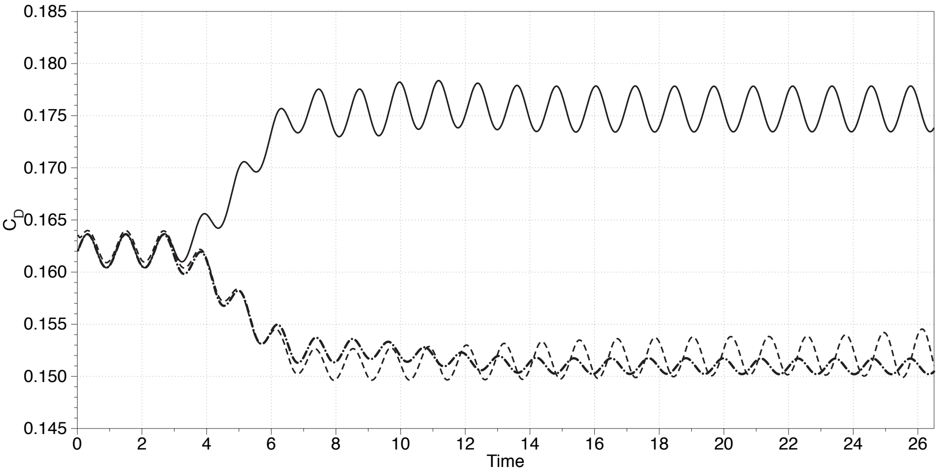

Figure 4.8: Comparison of the drag coefficient, detailed simulation with A=u_∞ (solid lines), POD-ROM using GPOD modes with A=$-u_\infty$ (dashed lines), and POD-ROM using RPOD modes with A=$-u_\infty$ (dotted lines).

energy is streamed toward the final set of modes. Therefore, more initial detailed simulations and samples of each simulation are taken into account by the final POD modes.

4.5.2 MPOD

In section 4.4.2, we introduced MPOD through which one can generate the POD modes for each simulation individually and then truncate the POD modes of each set and construct a second level set of POD modes. POD modes of the second set produces a cascade of information from initial simulations POD modes to the final set of POD modes, although, the size of matrices are manageable and the final modes are orthogonal. In section 4.4.3 we introduced RPOD as the right way multi-level POD process. To show the importance of weigthing the POD modes at the second level POD, we present the results of ROM using MPOD modes.

For the sake of right comparison between RPOD and MPOD, we use the same snapshots which were used in section 4.5.1. 550 snapshots of each six detailed simulation are sampled and POD is applied to derive 550 POD modes. So, six sets of modes are available, each includes 550 POD modes. The secondary POD applied on 200 low frequency primary POD modes to derive the final POD modes.

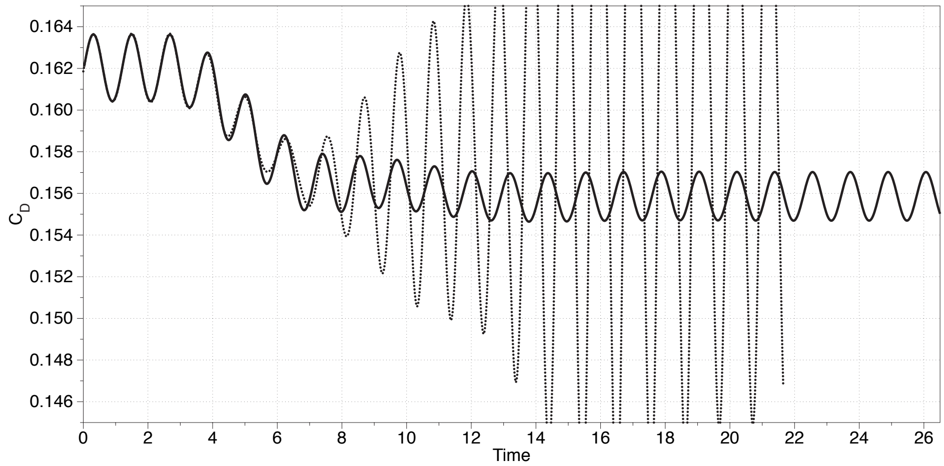

Figure 4.9: Comparison of the drag coefficient, detailed simulation with A=u_∞ (solid lines), detailed simulation with A=$-1/2u_\infty$ (dash-dotted lines), POD-ROM using MPOD basis with A=$-1/2u_\infty$ (dotted lines), POD-ROM using MPOD basis with A=u_∞ (dashed lines).

Therefore, the dimension of the secondary eigenproblem would be 1200, (6×200). 19 of the final modes are used to repeat the POD-ROMs. Fig. 4.9 shows the results of MPOD for the same case of above. Poor results have been met. The reason is various levels of energy corresponding to various flow simulations. Suppose that two flow with totally different level of energy are used as the input of MPOD. The second eigenproblem treats all the input POD modes the same, no matter that each POD mode represents a special amount of energy. Due to the same reason, eigenvalues spectrum of different cases are unique respect to that process.

4.6 Conclusion

The first goal of this section is a review on the methods which were developed to conquer the difficulties that the POD faces to represent the transient state of a fluid flow. The main issue in developing dynamically accurate low-dimensional models lies in obtaining a mode set that spans the entire parameter range of interest. The methods cathegorized to two main approches, enrichment of the flow and adding more modes to reduced order model. We focused on the enrichment of the modes and a novel method, called recursive proper orthogonal decomposition (RPOD) is introduced to solve the computational cost of the previous methods. Also, two well-known methods, Generalized POD basis and Global POD modes, were tested to show the advantage of the new method.

The so called methods were tested for a 2-D fluid flow over an airfoil at $Re = 1000$. The flow was acctuated with a fluidic jet located on the airfoil. It derives the fluid flow from a periodic state to a secondary periodic state with different amplitude and frequence. The magnitude of constant blowing/suction of the fluidic jet could be different and through that a variaty of fluid flow states were generate. The snapshots of the simulations was used as the data base.

We conclude that the Generalized POD basis needs a long comprehensive refrensed solution of Navier-Stokes to be able to produce appropriate POD modes. On the other hand GPOD can produce informative modes. But the data base should be large enough. GPOD is generally would be a more powerful method than the Generalized POd basis. But in order to derive informative modes, both methods suffer from solving giant eigenproblem. To solve that problem, we introduced a new method called recursive proper orthogonal decomposition (RPOD). The accuracy of the new method is as good as GPOD while it deals with smaller eigen problems. The idea is breaking the full POD applied on the data base to some smaller eigenproblems. The resulting POD modes are weigthed and employed as the inlet of a secondary eigenproblem. Through this idea, it is possible to decreas the computational time of solving an eigenproblem and keep the accuracy of the modes. Mathematically RPOD generates the optimal cascade of information from initial snapshots to final POD modes. Also the method that we propose appears to be a viable approach for clusters where most of the needed eigenproblems could be solved at the same time.

Chapter 5

Summary, Conclusions, and Recommendations for Future Work

In this chapter, concluding remarks and recommendations for future work are presented. The research performed here is motivated by the need for real time active control of fluid flow, and in particular, separation control of airflow over an airfoil at high angle of attack. It is possible to reduce the computational cost of fluid flow simulation if the flow velocity field can be expressed in term of some intelligent modes that characterizes the flow. These modes are typically evaluated from detailed simulations. This approach has the advantage that accounting for the energetic scales of the flow, so that the dominant features of the flow can be represented by a small number of modes. For example, for flow control applications, there is a need for rapid computation of the variation of the flow to external actuation. In this case, rapid availability of computational results is of essence as long as the majority of the energy of the flow is accounted for. Among the methods to decompose the fluid flow, the proper orthogonal decomposition (POD) that has attracted considerable attention, is used in the present study. That is a number of energetic modes is used to build a reduced order model for predicting the main feature of the flow. Other important aspect of this dissertation includes assessment of numerical errors of derivation of POD modes, building reduced order modeling for simple 1-D Burgers equation and 2-D flow over a NACA 0015 at low and high Reynolds number. One innovative aspect of the present thesis is the development of a new method by modifying the POD modes for accurate prediction of the flows under transient states.

5.0.1 Conclusion

5.0.1.1 Proper orthogonal decomposition based reduced order modeling for burger equation

Two important aspects of proper-orthogonal-decomposition-based reduced order modeling (POD-ROM) of the Burgers equation were examined. The first is the sensitivity of the eigenvalue spectrum and the POD modes to round-off errors and errors caused by using a reduced number of snapshots in building the POD. For both the direct and the snapshot method of solving the POD problem, solutions obtained using LAPACK's DGEEV were compared to a new method that we called the "deflation" method. The deflation method always gave positive eigenvalues where as LAPACK often gives spurious negative eigenvalues. However, the direct method using DGEEV was the only method that gave POD modes that are orthogonal to machine precision. For the snapshot method without deflation the orthogonality of the modes was poor for any mode beyond the point where the eigenvalues approach machine precision. The orthogonality of the snapshot method improved using the deflation method but not to machine precision. For the snapshot method, the number of snapshots required to obtain an accurate eigenvalue spectrum was determined by the smallest time scale of the phenomenon. After resolving this time scale, the errors in the eigenvalues and modes drop rapidly then converge with second-order accuracy. Second aspect which was studied is the effects of mode quality, ROM stabilization, and ROM dimension were investigated for low- and high-Reynolds number simulations of the Burgers equation. The ROM error was assessed using two errors, the error of projection of the problem onto the POD modes (the out-plane error) and the error of the ROM in the space spanned by POD modes (the in-plane error). The numerical results showed not only is the in-plane error bounded by the out-plane error (in agreement with theory) but it actually converges faster than the out-of-plane error. The total error was only weakly affected by the quality and orthogonality of the POD modes. Stabilization of the ROM had a positive effect at high-Re, but when the underlying grid used to derive the ROM is well-resolved, stabilization was not necessary.

5.0.1.2 On the robust proper orthogonal decomposition based reduced order modeling

This section investigated the accuracy of reduced order models (ROMs) for low and high Reynolds number flows. The benchmark configuration for low Reynolds case study was a 2D incompressible flow over a NACA0015 at an angle of attack of 12° at Re = 1000 such that separation occurred. The wake behind the airfoil is periodic at this Reynolds. The benchmark for high Reynolds case study was Re = 100,000 at angle of attack 15° where the flow became chaotic. For each flow, proper orthogonal decomposition (POD) modes were generated that included a pressure component to allow the easy calculation of drag forces from the model. For the low Reynolds number case, Galerkin, Streamwise-Upwind-Petrov-Galerkin (SUPG), and spectral vanishing viscosity (SVV) approaches were used for creating the POD-ROM. For short term prediction in the low Reynolds case, all models were in good agreement with the detailed simulation. However, the SUPG model was the only model that provided accurate long-term predictions. For the high Reynolds number case, the convergence rate of eigenvalues respect to the length of the time window which was used to generate the modes was very slow. For ROM, the Galerkin and SUPG approaches were compared. It was shown that both methods do provide good agreement with detailed simulation in the time window over which the POD modes are extracted. For long term simulation, neither SUPG ROM nor Galerkin ROM provided accurate results. The SUPG ROM decays to semi-periodic state where if the dimension of the ROM is increased, the amplitude of semi-periodic state is lower. The Galerking ROM method showed over prediction with error more than 100%. It was concluded that a wide time window of snapshots is needed to generate POD modes that can accurately predict turbulent flows. Also, the size of the POD ROM should be high for chaotic flows, because the energy distributed over a wide range of the modes. This result is in contradiction with the goal of reduced order modeling, that is using a few number of modes to have an accurate simulation of the flow.

5.0.1.3 Proper orthogonal decomposition based reduced order modeling for transient fluid flows

To have a set of POD modes which are capable to predict the flow over a transition of states, some methods have been recommended. The wildly used method is enrichment of the modes in terms of information to adjust their capability for prediction of a transient. In section 4, a review on the methods which were developed to conquer the difficulties that the POD faces to represent the transient state of a fluid flow, was done. The benchmark was a 2-D fluid flow over an airfoil at $Re = 1000$. The flow was actuated with a fluidic jet located on the airfoil. It drives the fluid flow from a periodic state to a secondary periodic state with different amplitude and frequency. Two well-known methods, Generalized POD basis and Global POD modes, were tested. We concluded that GPOD is more powerful than generalized POD basis. Hence, both methods need the solution of a huge eigenvalue problem. So, a novel method, called Recursive proper orthogonal decomposition (RPOD) was introduced to reduce the computational cost of the previous methods, while providing the accuracy of the GPOD. The idea is breaking the full POD applied on the data base to some smaller eigenproblems. The resulting POD modes are weighted and employed as the inlet of a secondary eigenproblem. Mathematically RPOD generates the optimal cascade of information from initial snapshots to final POD modes.

5.0.2 Recommendations for future work

The subject, covered in this these has a lot of potential in many engineering applications. The following recommendations for future study are made:

1. Additional investigation on the high Reynolds ROM is needed. The presented results showed that for high Reynolds flows the ROM requires very large number of modes to lead to accurate simulation. It also needs a very long duration detailed simulation for generating the modes POD modes. To overcome the computational cost of evaluating POD modes from a very long and highly resolved simulation, recursive proper orthogonal decomposition (RPOD), introduced in chapter 4, could be employed. Then, a large size ROM using those modes could be developed and tested. It is important to verify the application of POD-ROM for real time control application.

2. The presented study showed that for high Reynolds flows, a large number of modes should be employed for accurate description of the flow. To generate a low order model with small number of models, a closure model is necessary. On the other hand, it was shown that the dimension of ROM has a significant effect on results. Therefore, the closure model should take into account the effect of mode frequencies at high Reynolds POD ROMs. The idea of SUPG could be used where the time scale involved in SUPG should be modified by the effect of frequency of each mode. The eigenvalues correspond to each mode could be the key to develop and adjust the closure model.

3. Full state feedback control law could be developed to suppress vortex shedding behind the airfoil. Real dynamical systems require sensors and estimators for feedback control. In this work, the coefficients of each mode of the flow as the weight of main structures is the tool to decide about the feedback control. It means that instead of reading pressure at a specific point and use that as the input of feedback control, one can just use the coefficients of the energetic POD modes within a ROM. Also, thanks to the decomposition, it

is possible to just control a few energetic POD mode for control instead of dealing with the whole fluid structures.

Bibliography

[1] A.C. Antoulas. *Approximation of large-scale dynamical systems*, volume 6. Society for Industrial Mathematics, 2005.

[2] JL Lumley. The structure of inhomogeneous turbulent flows. *Atmospheric turbulence and radio wave propagation*, pages 166–178, 1967.

[3] K. Karhunen. *Zur spektraltheorie stochastischer prozesse.* Suomalainen tiedeakatemia, 1946.

[4] M. Loeve. Probability theory, 3rd éd, 1963.

[5] Nadine Aubry, Philip Holmes, John L. Lumley, and Emily Stone. The dynamics of coherent structures in the wall region of a turbulent boundary layer. *Journal of Fluid Mechanics*, 192:115–173, 1988. doi: 10.1017/S0022112088001818.

[6] S. Sirisup and GE Karniadakis. A spectral viscosity method for correcting the long-term behavior of pod models. *Journal of Computational Physics*, 194(1):92–116, 2004.

[7] M. Couplet, C. Basdevant, and P. Sagaut. Calibrated reduced-order pod-galerkin system for fluid flow modelling. *Journal of Computational Physics*, 207(1):192–220, 2005.

[8] L. Cordier, B.A. El Majd, and J. Favier. Calibration of pod reduced-order models using tikhonov regularization. *International Journal for Numerical Methods in Fluids*, 63(2):269–296, 2010.

[9] M. Bergmann, C.H. Bruneau, and A. Iollo. Improvement of reduced order modeling based on proper orthogonal decomposition. 2008.

[10] Z. Wang, I. Akhtar, J. Borggaard, and T. Iliescu. Two-level discretizations of nonlinear closure models for proper orthogonal decomposition. *Journal of Computational Physics*, 230(1):126 – 146, 2011. ISSN 0021-9991. doi: DOI:10.1016/j.jcp.2010.09.015.

[11] B. Podvin. On the adequacy of the ten-dimensional model for the wall layer. *Physics of fluids*, 13:210, 2001.

[12] B. Galletti, C.H. Bruneau, L. Zannetti, and A. Iollo. Low-order modelling of laminar flow regimes past a confined square cylinder. *Journal of Fluid Mechanics*, 503(-1):161–170, 2004.

[13] S. Ullmann and J. Lang. A pod-galerkin reduced model with updated coefficients for smagorinsky les. 2010.

[14] K. Kunisch and S. Volkwein. Galerkin proper orthogonal decomposition methods for parabolic problems. *Numerische Mathematik*, 90(1):117–148, 2001.

[15] J. Borggaard, T. Iliescu, and Z. Wang. Artificial viscosity proper orthogonal decomposition. *Mathematical and Computer Modelling*, 53(1-2):269–279, 2011.

[16] Z. Luo, Y. Zhou, and X. Yang. A reduced finite element formulation based on proper orthogonal decomposition for burgers equation. *Applied numerical mathematics*, 59(8):1933–1946, 2009.

[17] N.C. Nguyen, G. Rozza, and A.T. Patera. Reduced basis approximation and a posteriori error estimation for the time-dependent viscous burgers equation. *Calcolo*, 46(3):157–185, 2009.

[18] T.J.R. Hughes and M. Mallet. A new finite element formulation for computational fluid dynamics: Iii. the generalized streamline operator for multidimensional advective-diffusive systems* 1. *Computer Methods in Applied Mechanics and Engineering*, 58(3):305–328, 1986.

[19] L. Sirovich. Turbulence and the dynamics of coherent structures, i-coherent structures, ii-symmetries and transformations. *Quarterly of Applied Mathematics*, 45:561–571, 1987.

[20] E. Anderson, Z. Bai, and C. Bischof. *LAPACK Users' guide*, volume 9. Society for Industrial Mathematics, 1999.

[21] B.N. Parlett. *The symmetric eigenvalue problem*, volume 20. Society for Industrial Mathematics, 1998.

[22] M. Rathinam and L.R. Petzold. A new look at proper orthogonal decomposition. *SIAM Journal on Numerical Analysis*, 41(5):1893–1925, 2003.

[23] B.R. Noack, P. Papas, and P.A. Monkewitz. The need for a pressure-term representation in empirical galerkin models of incompressible shear flows. *Journal of Fluid Mechanics*, 523(1):339–365, 2005.

[24] G.H. Golub and C.F. Van Loan. Matrix computations. 1996. *Johns Hopkins University, Press, Baltimore, MD, USA*, 1996.

[25] A. Barbagallo, D. Sipp, and P.J. Schmid. Closed-loop control of an open cavity flow using reduced-order models. *Journal of Fluid Mechanics*, 641 (-1):1–50, 2009.

[26] W. Cazemier, R. W. C. P. Verstappen, and A. E. P. Veldman. Proper orthogonal decomposition and low-dimensional models for driven cavity flows. *Physics of Fluids*, 10(7):1685–1699, 1998. doi: 10.1063/1.869686.

[27] D. Rempfer. Investigations of boundary layer transition via galerkin projections on empirical eigenfunctions. *Physics of Fluids*, 8(1):175–188, 1996. doi: 10.1063/1.868825.

[28] Dietmar Rempfer and Hermann F. Fasel. Evolution of three-dimensional coherent structures in a flat-plate boundary layer. *Journal of Fluid Mechanics*, 260:351–375, 1994. URL `http://dx.doi.org/10.1017/S0022112094003551`.

[29] I. Akhtar, A.H. Nayfeh, et al. Model based control of laminar wake using fluidic actuation. *Journal of Computational and Nonlinear Dynamics*, 5: 041015, 2010.

[30] I. Akhtar, A.H. Nayfeh, and C.J. Ribbens. On the stability and extension of reduced-order galerkin models in incompressible flows. *Theoretical and Computational Fluid Dynamics*, 23(3):213–237, 2009.

[31] M. Bergmann, L. Cordier, and J.P. Brancher. Optimal rotary control of the cylinder wake using proper orthogonal decomposition reduced-order model. *Physics of Fluids*, 17:097101, 2005.

[32] X. Ma and G.E. Karniadakis. A low-dimensional model for simulating three-dimensional cylinder flow. *Journal of Fluid Mechanics*, 458(-1):181–190, 2002.

[33] L. Sirovich and JD Rodriguez. Coherent structures and chaos: a model problem. *Physics Letters A*, 120(5):211–214, 1987.

[34] M. Rajaee, S.K.F. Karlsson, and L. Sirovich. Low-dimensional description of free-shear-flow coherent structures and their dynamical behaviour. *Journal of Fluid Mechanics*, 258:1–1, 1994.

[35] R.E.A. Arndt, DF Long, and MN Glauser. The proper orthogonal decomposition of pressure fluctuations surrounding a turbulent jet. *Journal of Fluid Mechanics*, 340(1):1–33, 1997.

[36] B. Podvin and J. Lumley. A low-dimensional approach for the minimal flow unit. *Journal of Fluid Mechanics*, 362(1):121–155, 1998.

[37] L. Ukeiley, L. Cordier, R. Manceau, J. Delville, M. Glauser, and JP Bonnet. Examination of large-scale structures in a turbulent plane mixing layer. part

2. dynamical systems model. *Journal of Fluid Mechanics*, 441(1):67–108, 2001.

[38] D. Ahlman, F. Söderlund, J. Jackson, A. Kurdila, and W. Shyy. Proper orthogonal decomposition for time-dependent lid-driven cavity flows. *Numerical Heat Transfer: Part B: Fundamentals*, 42(4):285–306, 2002.

[39] E. Caraballo, J. Little, M. Debiasi, and M. Samimy. Development and implementation of an experimental-based reduced-order model for feedback control of subsonic cavity flows. *Journal of fluids engineering*, 129(7):813–824, 2007.

[40] J.P. Chollet and M. Lesieur. Parameterization of small scales of three-dimensional isotropic turbulence utilizing spectral closures. *Journal of Atmospheric Sciences*, 38:2747–2757, 1981.

[41] Olivier Mtais and Marcel Lesieur. Spectral large-eddy simulation of isotropic and stably stratified turbulence. *Journal of Fluid Mechanics*, 239:157–194, 1992. doi: 10.1017/S0022112092004361.

[42] E. Tadmor. Convergence of spectral methods for nonlinear conservation laws. *SIAM Journal on Numerical Analysis*, 26(1):30–44, 1989.

[43] M. Buffoni, S. Camarri, A. Iollo, and M. V. Salvetti. Low-dimensional modelling of a confined three-dimensional wake flow. *Journal of Fluid Mechanics*, 569:141–150, 2006. doi: 10.1017/S0022112006002989.

[44] L. Perret, E. Collin, J. Delville, et al. Polynomial identification of pod based low-order dynamical system. *Journal of Turbulence*, 7(17):1–15, 2006.

[45] B. Galletti, A. Bottaro, C.H. Bruneau, and A. Iollo. Accurate model reduction of transient and forced wakes. *European Journal of Mechanics-B/Fluids*, 26(3):354–366, 2007.

[46] E. Lombardi, M. Bergmann, S. Camarri, A. Iollo, et al. Low-order models: optimal sampling and linearized control strategies. 2009.

[47] A. Hay, J.T. Borggaard, and D. Pelletier. Local improvements to reduced-order models using sensitivity analysis of the proper orthogonal decomposition. *Journal of Fluid Mechanics*, 629(1):41–72, 2009.

[48] Sunil Ahuja and Clarence W Rowley. Feedback control of unstable steady states of flow past a flat plate using reduced-order estimators. *Journal of Fluid Mechanics*, 645:447–478, 2010.

[49] Zhanhua Ma, Sunil Ahuja, and Clarence W Rowley. Reduced-order models for control of fluids using the eigensystem realization algorithm. *Theoretical and Computational Fluid Dynamics*, 25(1-4):233–247, 2011.

[50] J. Kim and T.R. Bewley. A linear systems approach to flow control. *Annu. Rev. Fluid Mech.*, 39:383–417, 2007.

[51] J. Seidel, C. Fagley, and T. McLaughlin. Structure identification in turbulent flows for feedback flow control. *Physica Scripta*, 2010(T142):014008, 2010.

[52] CE Tinney, MN Glauser, and LS Ukeiley. Low-dimensional characteristics of a transonic jet. part 1. proper orthogonal decomposition. *Journal of Fluid Mechanics*, 612:107–141, 2008.

[53] CE Tinney, LS Ukeiley, and MN Glauser. Low-dimensional characteristics of a transonic jet. part 2. estimate and far-field prediction. *Journal of Fluid Mechanics*, 615:53–92, 2008.

[54] WL Siauw, J-P Bonnet, J Tensi, L Cordier, BR Noack, and L Cattafesta. Transient dynamics of the flow around a naca 0015 airfoil using fluidic vortex generators. *International Journal of Heat and Fluid Flow*, 31(3):450–459, 2010.

[55] M Samimy, M Debiasi, E Caraballo, A Serrani, X Yuan, J Little, and JH Myatt. Feedback control of subsonic cavity flows using reduced-order models. *Journal of Fluid Mechanics*, 579:315–346, 2007.

[56] RD Wallace, PR Shea, MN Glauser, V. Thirunakkarasu, and HA Carlson. Simulation-guided, model-based feedback flow control for a pitching turret. *AIAA Journal*, 50(8):1685–1696, 2012.

[57] M. Arienti and M.C. Soteriou. Time-resolved proper orthogonal decomposition of liquid jet dynamics. *Physics of Fluids*, 21:112104, 2009.

[58] A. Sinha, A. Serrani, and M. Samimy. Initial development of reduced-order models for feedback control of axisymmetric jets. *International Journal of Flow Control*, 2(1):39–60, 2010.

[59] M. Dubiner. Spectral methods on triangles and other domains. *J. Sci. Comput.*, 6(4):345–390, 1991.

[60] S. J. Sherwin and G. E. Karniadakis. A triangular spectral element method: Applications to the incompressible Navier-Stokes equations. *Comp. Meth. App. Mech. Eng.*, 123:189–229, 1995.

[61] R. Williams, K. Burrage, I. Cameron, and M. Kerr. A four-stage index 2 diagonally implicit runge-kutta method. *Applied numerical mathematics*, 40 (3):415–432, 2002.

[62] C Gear. Simultaneous numerical solution of differential-algebraic equations. *Circuit Theory, IEEE Transactions on*, 18(1):89–95, 1971.

[63] BT Helenbrook. A two-fluid spectral-element method. *Computer methods in applied mechanics and engineering*, 191(3-5):273–294, 2001.

[64] Brian T Helenbrook and Timothy J Baker. An adaptive spectral element method for two-fluid flows. In *ASME 2002 Joint US-European Fluids Engineering Division Conference*, pages 439–446. American Society of Mechanical Engineers, 2002.

[65] M. Couplet, P. Sagaut, and C. Basdevant. Intermodal energy transfers in a proper orthogonal decomposition galerkin representation of a turbulent separated flow. *Journal of Fluid Mechanics*, 491(-1):275–284, 2003.

[66] S.N. Singh, J.H. Myatt, G.A. Addington, S. Banda, and J.K. Hall. Optimal feedback control of vortex shedding using proper orthogonal decomposition models. *Journal of fluids engineering*, 123:612, 2001.

[67] O.K. Rediniotis, J. Ko, and A.J. Kurdila. Reduced order nonlinear navier-stokes models for synthetic jets. *Journal of fluids engineering*, 124(2):433–443, 2002.

[68] C. W. Rowley, T. Colonius, and R. M. Murray. Model reduction for compressible flows using POD and Galerkin projection. *Physica D*, 189(1-2): 115–129, February 2004.

[69] BJ O'Donnell and BT Helenbrook. Proper orthogonal decomposition and incompressible flow: An application to particle modeling. *Computers & fluids*, 36(7):1174–1186, 2007.

[70] M. Bergmann, C.H. Bruneau, and A. Iollo. Enablers for robust pod models. *Journal of Computational Physics*, 228(2):516–538, 2009.

[71] R. Pasquetti. Spectral vanishing viscosity method for les: sensitivity to the svv control parameters. *Journal of Turbulence*, (6), 2005.

[72] R. Pasquetti. Spectral vanishing viscosity method for high-order les: Computation of the dissipation rates. In *ECCOMAS CFD 2006 Congress, Egmond aan Zee, Holland*, pages 5–8, 2006.

[73] RC Camphouse, JH Myatt, RF Schmit, MN Glauser, JM Ausseur, MY Andino, and RD Wallace. A snapshot decomposition method for reduced order modeling and boundary feedback control. In *38 th AIAA Fluid Dynamics Conference and Exhibit, 39 th AIAA Plasmadynamics and Lasers Conference, 40 th AIAA Thermophysics Conference, 5 th AIAA Theoretical Fluid Mechanics Conference, 4 th AIAA Flow Control Conference, and the 26 th AIAA Aerodynamic Measurement Technology and Ground Testing Conference.* American Institute of Aeronautics and Astronautics, 1801 Alexander Bell Drive, Suite 500, Reston, VA, 20191-4344, USA,, 2008.

[74] A. Gelb and E. Tadmor. Enhanced spectral viscosity approximations for conservation laws. *Applied Numerical Mathematics*, 33(1):3–22, 2000.

[75] Fariduddin Behzad, Brian T Helenbrook, and Goodarz Ahmadi. On the sensitivity and accuracy of proper-orthogonal-decomposition-based reduced order models for burgers equation. *Computers and Fluids*, 2014.

[76] Y. Maday, S.M. Ould Kaber, and E. Tadmor. Legendre pseudospectral viscosity method for nonlinear conservation laws. *SIAM Journal on Numerical Analysis*, 30(2):321–342, 1993.

[77] GS Karamanos and G.E. Karniadakis. A spectral vanishing viscosity method for large-eddy simulations. *Journal of Computational Physics*, 163(1):22–50, 2000.

[78] B.T. Helenbrook. Mesh deformation using the biharmonic operator. *International journal for numerical methods in engineering*, 56(7):1007–1021, 2003.

[79] WR Graham, J. Peraire, and KY Tang. Optimal control of vortex shedding using low-order models. part iimodel-based control. *International journal for numerical methods in engineering*, 44:945–972, 1999.

[80] WR Graham, J. Peraire, and KY Tang. Optimal control of vortex shedding using low-order models. part iimodel-based control. *International journal for numerical methods in engineering*, 44(7):973–990, 1999.

[81] G. Berkooz, P. Holmes, and J.L. Lumley. The proper orthogonal decomposition in the analysis of turbulent flows. *Annual review of fluid mechanics*, 25(1):539–575, 1993.

[82] A.E. Deane and C. Mavriplis. Low-dimensional description of the dynamics in separated flow past thick airfoils. *AIAA journal*, 32(6):1222–1227, 1994.

[83] J. Kriegseis, T. Dehler, M. Gnirß, and C. Tropea. Common-base proper orthogonal decomposition as a means of quantitative data comparison. *Measurement Science and Technology*, 21:085403, 2010.

[84] R. Schmit and M. Glauser. Improvements in low dimensional tools for flow-structure interaction problems: using global pod. 1, 2003.

[85] JA Taylor and MN Glauser. Towards practical flow sensing and control via pod and lse based low-dimensional tools. *Journal of fluids engineering*, 126: 337, 2004.

[86] S.G. Siegel, K. Cohen, J. Seidel, and T. McLaughlin. Short time proper orthogonal decomposition for state estimation of transient flow fields. In *43 rd AIAA Aerospace Sciences Meeting and Exhibit*, page 2005, 2005.

[87] J. Weller, E. Lombardi, M. Bergmann, and A. Iollo. Numerical methods for low-order modeling of fluid flows based on pod. *International Journal for Numerical Methods in Fluids*, 63(2):249–268, 2010. ISSN 1097-0363. doi: 10.1002/fld.2025.

[88] B.R. Noack, K. Afanasiev, M. Morzynski, G. Tadmor, and F. Thiele. A hierarchy of low-dimensional models for the transient and post-transient cylinder wake. *Journal of Fluid Mechanics*, 497(-1):335–363, 2003.

[89] S. Siegel, K. Cohen, and T. McLaughlin. Feedback control of a circular cylinder wake in experiment and simulation. *AIAA paper*, 3569, 2003.

[90] J. Gerhard, M. Pastoor, R. King, B.R. Noack, A. Dillmann, M. Morzynski, and G. Tadmor. Model-based control of vortex shedding using low-dimensional galerkin models. *AIAA paper*, 4262:2003, 2003.

[91] EA Christensen, JN Sørensen, M. Brøns, and PL Christiansen. Low-dimensional representations of early transition in rotating fluid flow. *Theoretical and Computational Fluid Dynamics*, 5(6):259–267, 1993.

[92] M. Morzynski, W. Stankiewicz, B.R. Noack, F. Thiele, R. King, and G. Tadmor. Generalized mean-field model for flow control using a continuous mode interpolation. In *Proceedings of the Third AIAA Flow Control Conference*, 2006.

[93] M. Morzynski, W. Stankiewicz, B. Noack, R. King, F. Thiele, and G. Tadmor. Continuous mode interpolation for control-oriented models of fluid flow. *Active Flow Control*, pages 260–278, 2007.

[94] T. Lieu and M. Lesoinne. Parameter adaptation of reduced order models for three-dimensional flutter analysis. In *42 nd AIAA Aerospace Sciences Meeting and Exhibit*, 2004.

[95] D. Amsallem and C. Farhat. Interpolation method for adapting reduced-order models and application to aeroelasticity. *AIAA Journal-American Institute of Aeronautics and Astronautics*, 46(7):1803–1813, 2008.

[96] T. Lieu, C. Farhat, and M. Lesoinne. Reduced-order fluid/structure modeling of a complete aircraft configuration. *Computer methods in applied mechanics and engineering*, 195(41):5730–5742, 2006.

[97] T. Lieu and C. Farhat. Adaptation of aeroelastic reduced-order models and application to an f-16 configuration. *AIAA journal*, 45(6):1244–1257, 2007.

[98] A. Hay, J. Borggaard, I. Akhtar, and D. Pelletier. Reduced-order models for parameter dependent geometries based on shape sensitivity analysis. *Journal of Computational Physics*, 229(4):1327–1352, 2010.

[99] I. Akhtar, J. Borggaard, A. Hay, et al. Shape sensitivity analysis in flow models using a finite-difference approach. *Mathematical Problems in Engineering*, 2010:1–22, 2010.

[100] A. Hay, I. Akhtar, and J.T. Borggaard. On the use of sensitivity analysis in model reduction to predict flows for varying inflow conditions. *International Journal for Numerical Methods in Fluids*, 68(1):122–134, 2012.

[101] B.H. Jørgensen, J.N. Sørensen, and M. Brøns. Low-dimensional modeling of a driven cavity flow with two free parameters. *Theoretical and computational fluid dynamics*, 16(4):299–317, 2003.

[102] S. Siegel, K. Cohen, J. Seidel, and T. McLaughlin. State estimation of transient flow fields using double proper orthogonal decomposition (dpod). *Active Flow Control*, pages 105–118, 2007.

[103] S.G. Siegel, J.U.R. Seidel, C. Fagley, DM Luchtenburg, K. Cohen, T. Mclaughlin, et al. Low-dimensional modelling of a transient cylinder wake using double proper orthogonal decomposition. *Journal of Fluid Mechanics*, 610:1–42, 2008.

[104] K. Afanasiev and M. Hinze. Adaptive control of a wake flow using proper orthogonal decomposition1. In *Shape optimization and optimal design: proceedings of the IFIP conference*, page 317. CRC, 2001.

[105] Fariduddin Behzad, Brian T. Helenbrook, and Goodarz Ahmadi. On reduced order modeling of transient flow using the preserving orthogonal decomposition. 2012.

[106] Michael J. Brazell and Brian T. Helenbrook. p=2 continuous finite elements on tetrahedra with local mass matrix inversion. *Computer Methods in Applied Mechanics and Engineering*, 213-216(0):289 – 298, 2012. ISSN 0045-7825.

[107] J.M. Ausseur and J.T. Pinier. Towards closed-loop feedback control of the flow over naca-4412 airfoil. In *43 rd AIAA Aerospace Sciences Meeting and Exhibit*, page 2005, 2005.

[108] Alfonso Caiazzo, Traian Iliescu, Volker John, and Swetlana Schyschlowa. A numerical investigation of velocity–pressure reduced order models for incompressible flows. *Journal of Computational Physics*, 259:598–616, 2014.

[109] M. Bergmann and L. Cordier. Optimal control of the cylinder wake in the laminar regime by trust-region methods and pod reduced-order models. *Journal of Computational Physics*, 227(16):7813–7840, 2008.